

# Search For the Rare Decay $K_L \rightarrow \pi^0 \pi^0 \gamma$

David Edward Smith  
Pasadena, MD

B.S., University of Oklahoma, 2001

A Thesis presented to the Graduate Faculty of the University of  
Virginia in Candidacy for the Degree of Doctor of Philosophy

Department of Physics

University of Virginia  
August, 2006

---

---

---

---

# Abstract

This thesis describes a search for the rare decay  $K_L \rightarrow \pi^0 \pi^0 \gamma$  using data from the KTeV experiment, using the topology  $K_L \rightarrow \pi^0 \pi_D^0 \gamma$  (where  $\pi_D^0 \rightarrow \gamma e^+ e^-$ ). Due to Bose statistics and the real nature of the photon, the  $K_L \rightarrow \pi^0 \pi^0 \gamma$  decay can proceed at lowest order only by the CP conserving direct emission of an E2 photon. The decay vanishes to  $O(p^4)$  in chiral perturbation theory and is a probe of the theory to the sixth order. The primary background to this decay consists of  $K_L \rightarrow \pi^0 \pi^0 \pi_D^0$  events with one lost photon.

The upper limit for the decay  $K_L \rightarrow \pi^0 \pi^0 \gamma$  presented in this thesis is  $2.32 \times 10^{-7}$  at the 90% confidence level. This upper limit was derived from both 1997 and 1999 data, using a blind analysis. The upper limit was derived from a Feldman-Cousins method, based on a weighted total of 0.53 data events in the signal region with an expected  $K_L \rightarrow \pi^0 \pi^0 \pi_D^0$  background of  $0.37 \pm 0.28$  events. The previous upper limit for this decay was  $5.6 \times 10^{-6}$  at the 90% confidence level.

## Acknowledgments

This work would not have been possible without the help of many different people. First and foremost, I would like to thank my advisor Brad Cox for his continual guidance in both my analysis and the writing of this thesis. Invaluable assistance was also provided by Michael Arenton and particularly Sasha Ledovskoy, who "got me on my feet" with the analysis and provided help throughout the project.

I would also like to thank my fellow students, Sasha Golossanov, John Shields, Michael Ronquest, David Williams and David Phillips for their assistance and friendship, and the other members of the KTeV collaboration for their insights and suggestions. Finally, I could not have done this without the love and support of my friends and family, particularly my mother, JoAnne.

David Smith

Charlottesville, Virginia

July 6, 2006



# Contents

<b>1</b>	<b>Introduction</b>	<b>1</b>
1.1	Introduction . . . . .	1
1.2	The $K_L$ System and CP Violation . . . . .	2
1.2.1	Symmetries: C, P and CP . . . . .	2
1.2.2	The $K^0 \bar{K}^0$ System . . . . .	2
1.3	The Decay $K_L \rightarrow \pi^0 \pi^0 \gamma$ . . . . .	4
1.3.1	Introduction to the Decay . . . . .	4
1.3.2	Matrix Element and Decay Rate . . . . .	6
1.3.3	The Decay $K_L \rightarrow \pi^0 \pi_D^0 \gamma$ as a Probe of Chiral Perturbation Theory . . . . .	6
1.3.4	Previous Searches for the Decay . . . . .	7
<b>2</b>	<b>The KTeV detector</b>	<b>9</b>
2.1	Introduction to KTeV . . . . .	9
2.2	Beam Production . . . . .	10
2.3	Sweepers, Absorbers and Collimators . . . . .	13
2.4	The Beam . . . . .	15

2.5	Vacuum Window and Ring Counters . . . . .	15
2.6	Charged Particle Spectrometer . . . . .	16
2.6.1	Drift Chambers . . . . .	16
2.6.2	The Magnet . . . . .	18
2.6.3	Momentum Resolution . . . . .	18
2.7	The Cesium Iodide Calorimeter . . . . .	19
2.7.1	Crystal Readout . . . . .	20
2.7.2	Calibration . . . . .	21
2.7.3	Energy and Position Resolution . . . . .	21
2.8	Other Parts of the Detector . . . . .	23
2.8.1	The VV' Trigger Hodoscope . . . . .	23
2.8.2	Transition Radiation Detectors . . . . .	23
2.8.3	The Hadron Anti . . . . .	23
2.8.4	Beam Dump and Muon Detector . . . . .	24
2.8.5	Other Vetoes . . . . .	24
<b>3</b>	<b>Trigger and Event Selection</b>	<b>26</b>
3.1	Level 1 . . . . .	26
3.1.1	DC-OR signals . . . . .	27
3.1.2	The 2E-NCLUS Trigger . . . . .	28
3.2	Level 2 . . . . .	28
3.2.1	Hardware Cluster Counter . . . . .	29
3.2.2	DC Hit Counters . . . . .	31
3.2.3	2E-NCLUS trigger: Level 2 . . . . .	31

3.3	Event Readout . . . . .	32
3.4	Level 3 . . . . .	32
3.5	2E-NCLUS Crunch . . . . .	33
<b>4</b>	<b>Event Reconstruction</b>	<b>34</b>
4.1	Tracking . . . . .	34
4.1.1	Hit Pairs and SODs . . . . .	35
4.1.2	y-track Finding . . . . .	37
4.1.3	x-track Finding . . . . .	38
4.2	Clustering . . . . .	38
4.2.1	Hardware Clustering . . . . .	38
4.2.2	Software Clustering . . . . .	39
4.2.3	Cluster Positioning . . . . .	39
4.2.4	Clustering Corrections . . . . .	39
4.3	Vertexing . . . . .	41
<b>5</b>	<b>KTeV Monte Carlo</b>	<b>44</b>
5.1	Simulation of Kaon Production . . . . .	44
5.2	Simulation of $K_L$ Decay . . . . .	46
5.2.1	$K_L \rightarrow \pi^0 \pi^0 \gamma$ Generation . . . . .	47
5.2.2	$K_L \rightarrow \pi^0 \pi^0 \pi^0$ Generation . . . . .	47
5.2.3	$\pi^0 \rightarrow e^+ e^- \gamma$ Dalitz Decay . . . . .	47
5.3	Particle Tracing . . . . .	48
5.4	Particle Interactions . . . . .	48

5.4.1	Photon Conversion . . . . .	48
5.4.2	Multiple Scattering . . . . .	49
5.4.3	Bremsstrahlung . . . . .	50
5.5	Detector Simulation . . . . .	50
5.5.1	Photon Vetoes and VV' counter . . . . .	50
5.5.2	Charged Particle Spectrometer Simulation . .	51
5.5.3	TRDs . . . . .	52
5.5.4	Calorimeter Simulation . . . . .	53
5.6	Accidental Overlays . . . . .	54
5.7	Trigger Simulation . . . . .	55
5.8	Monte Carlo Samples . . . . .	55
5.8.1	2E-NCLUS Trigger and Crunch . . . . .	55
<b>6</b>	<b>The Combined Vertexing Routine</b>	<b>57</b>
6.1	Track Component of Combined Vertex . . . . .	58
6.2	$\gamma\gamma$ Component of Combined Vertex . . . . .	60
6.3	$ee\gamma$ Component of Combined Vertex . . . . .	60
6.4	Accuracy of the Combined Vertex . . . . .	62
<b>7</b>	<b>The Normalization Mode Analysis</b>	<b>63</b>
7.1	Definition of the Normalization Mode . . . . .	63
7.2	Normalization Mode Selection Cuts . . . . .	64
7.2.1	Missing Photon Position Cut . . . . .	64
7.2.2	Gamma-Gamma Mass Cut . . . . .	64



7.2.3	Beamhole Photon Energy Cut . . . . .	64
7.2.4	PP0KINE Cut . . . . .	65
7.2.5	Vertex $\chi^2$ Cut . . . . .	65
7.2.6	Vertex Z-position Cut . . . . .	66
7.2.7	$m_{ee\gamma}$ Cut . . . . .	66
7.2.8	$m_{\gamma\gamma}$ Cut . . . . .	66
7.2.9	Vertex x- and y- position cut . . . . .	66
7.2.10	Fusion $\chi^2$ Cut . . . . .	67
7.2.11	Next-best Vertex $\chi^2$ Cut . . . . .	67
7.2.12	$\gamma\gamma$ Mispairing Cut . . . . .	68
7.2.13	Overlapping Clusters Cut . . . . .	68
7.3	$K_L$ Flux Calculation . . . . .	69
7.4	The Final Normalization Sample . . . . .	69
<b>8</b>	<b>The Signal Mode Analysis</b>	<b>87</b>
8.1	Defining the Signal Region . . . . .	87
8.2	Blind Analysis Method . . . . .	88
8.3	Justification of $K_L \rightarrow \pi^0 \pi^0 \pi_D^0$ As Primary Background	89
8.4	The Analysis Cuts . . . . .	89
8.4.1	Vertex $\chi^2$ . . . . .	89
8.4.2	Vertex Z-Position . . . . .	90
8.4.3	$m_{ee\gamma}$ . . . . .	90
8.4.4	$m_{\gamma\gamma}$ . . . . .	90
8.4.5	Vertex X- and Y- Position . . . . .	91

8.4.6	Fusion $\chi^2$ . . . . .	91
8.4.7	PP0KINE Cut . . . . .	92
8.4.8	$m_{\pi\pi}$ Cut . . . . .	92
8.4.9	$\pi^0 - \gamma$ Angle Cut . . . . .	93
8.4.10	Overlapping Clusters Cut . . . . .	93
8.4.11	Next-best Vertex $\chi^2$ Cut . . . . .	94
8.4.12	$\gamma\gamma$ Mispairing Cut . . . . .	94
8.4.13	Summary of Cuts . . . . .	94
8.5	Opening the Signal Regions . . . . .	94
<b>9</b>	<b>Systematic Errors</b>	<b>122</b>
9.1	The Single Event Sensitivity . . . . .	122
9.2	Calculating the Combined SES . . . . .	123
9.3	Systematic Error on the SES . . . . .	124
9.3.1	Statistical Error on the Acceptances . . . . .	125
9.3.2	Total Error on the SES . . . . .	125
9.4	Error on the Expected Background . . . . .	125
<b>10</b>	<b>Final Result and Conclusion</b>	<b>128</b>
10.1	The Basic Method . . . . .	128
10.2	Incorporating Errors . . . . .	129
10.3	Weighting Events . . . . .	130
10.4	The Upper Limit . . . . .	131
10.5	Conclusion . . . . .	134

# List of Figures

1.1	One of several diagrams contributing to oscillations between $K^0$ and $\bar{K}^0$ . . . . .	3
1.2	The Feynman diagram for the decay $K_L \rightarrow \pi^0 \pi^0 \gamma$ . .	5
2.1	The KTeV detector for 799 running (3-D view). . . .	11
2.2	The KTeV detector for 799 running (plan view). . . .	12
2.3	Y-view of beamline elements in the NM2 enclosure. .	13
2.4	The field and sense wire arrangement within a drift chamber. . . . .	18
2.5	The size and structure of the CsI calorimeter. . . . .	20
2.6	Energy/momentum distribution for electrons from $K_{e3}$ decays. . . . .	22
2.7	Calorimeter energy resolution as a function of track momentum, for electrons. . . . .	22
2.8	Structure of the VV' trigger hodoscope. . . . .	24
3.1	Possible HCC bit patterns and corresponding weights for a 2 by 2 group of calorimeter blocks. . . . .	30

4.1	The arrival times of signals in DC1 during run 8397. . . . .	36
4.2	Categories of SODs from a charged track. . . . .	36
4.3	SOD distribution from a sample of $K_L \rightarrow \pi^0 \pi_D^0$ events. . . . .	37
4.4	Mean E/p vs. p of calibration $K_{e3}$ electrons in small blocks, after all clustering corrections after the lin- earity fudge. . . . .	41
4.5	A completely reconstructed event displayed using the KDISP program. . . . .	43
6.1	Z resolution in meters of the combined (solid line) vs. charged (dotted line) vertex routines. . . . .	61
7.1	Reconstructed x-position of the T3MISP photon at the CsI face for 1997 and 1999 running. . . . .	71
7.2	Reconstructed y-position of the T3MISP photon at the CsI face for 1997 and 1999 running. . . . .	72
7.3	Combined mass of the T3MISP photon and the direct emission photon for 1997 and 1999 running. . . . .	73
7.4	Reconstructed energy of the T3MISP (beamhole) pho- ton for 1997 and 1999 running. . . . .	74
7.5	Normalization mode PP0KINE for 1997 and 1999 running. . . . .	75
7.6	Normalization mode combined vertex $\chi^2$ for 1997 and 1999 running. . . . .	76

7.7	Normalization mode vertex z-position for 1997 and 1999 running. . . . .	77
7.8	Normalization mode $m_{ee\gamma}$ for 1997 and 1999 running.	78
7.9	Normalization mode $m_{\gamma\gamma}$ for 1997 and 1999 running.	79
7.10	Normalization mode vertex x-projection at the CsI face for 1997 and 1999 running. . . . .	80
7.11	Normalization mode vertex y-projection at the CsI face for 1997 and 1999 running. . . . .	81
7.12	Normalization mode fusion $\chi^2$ for 1997 and 1999 running. . . . .	82
7.13	Difference between the next best and best vertex $\chi^2$ for the normalization mode for 1997 and 1999 running.	83
7.14	Minimum mass of any $\gamma\gamma$ pair other than the correct one for the normalization mode, for 1997 and 1999 running. . . . .	84
7.15	Overlapping cluster $\chi^2$ for the normalization mode for 1997 and 1999 running. . . . .	85
7.16	Combined mass of the T3MISP photon and the direct emission photon for 1997 and 1999 running, on a logarithmic scale. . . . .	86
8.1	$m_{ee\gamma\gamma\gamma}$ (in $GeV/c^2$ ) vs $p_t^2$ (in $(GeV/c)^2$ ) for $K_L \rightarrow \pi^0\pi_D^0\gamma$ MC events after the bad run/spill cut. The signal box is marked. . . . .	97

8.2	$m_{ee\gamma\gamma\gamma}$ (top, in $GeV/c^2$ ) and $p_t^2$ (bottom, in $(GeV/c)^2$ ) distributions for 1999 signal mode events past the crunch, used as an input in determining the 1999 signal region. . . . .	98
8.3	Logarithm of $P(m_{ee\gamma\gamma\gamma}, p_t^2)$ for 1999 $K_L \rightarrow \pi^0\pi_D^0\gamma$ MC events (red) and $K_L \rightarrow \pi^0\pi^0\pi_D^0$ MC events (dots) after the bad run/spill cut. Events with a value greater than -6.6 are considered to be in the signal region. . .	99
8.4	$m_{ee\gamma\gamma\gamma}$ (in $GeV/c^2$ ) vs. $p_t^2$ (in $(GeV/c)^2$ ) for 1999 $K_L \rightarrow \pi^0\pi_D^0\gamma$ MC events after the bad run/spill cut. The signal region is marked. . . . .	100
8.5	Total mass $m_{ee\gamma\gamma\gamma}$ for events outside the signal region after all cuts. . . . .	101
8.6	$p_t^2$ for events outside the signal region after all cuts. .	102
8.7	Vertex $\chi^2$ for events outside the signal region after all cuts. . . . .	103
8.8	Vertex z-position for events outside the signal region after all cuts. . . . .	104
8.9	Vertex $\chi^2$ for events inside the signal region before the cut, for signal and background MC. . . . .	105
8.10	Vertex z-position for events inside the signal region before the cut, for signal and background MC. . . .	106

8.11	$m_{ee\gamma}$ for events inside the signal region before the cut, for signal and background MC. . . . .	107
8.12	$m_{\gamma\gamma}$ for events inside the signal region before the cut, for signal and background MC. . . . .	108
8.13	Vertex x-projection at the calorimeter face for events inside the signal region before the cut, for signal and background MC. . . . .	109
8.14	Vertex y-projection at the calorimeter face for events inside the signal region before the cut, for signal and background MC. . . . .	110
8.15	Fusion $\chi^2$ for events inside the signal region before the cut, for signal and background MC. . . . .	111
8.16	PP0KINE for events inside the signal region before the cut, for signal and background MC. . . . .	112
8.17	$m_{\pi\pi}$ for events inside the signal region before the cut, for signal and background MC. . . . .	113
8.18	Cosine of the angle between a randomly chosen $\pi^0$ and the direct emission photon, in the $2\pi$ rest frame for events inside the signal region before the cut, for signal and background MC. . . . .	114
8.19	Overlapping cluster $\chi^2$ for events inside the signal region before the cut, for signal and background MC. . . . .	115

8.20	Next best minus best vertex $\chi^2$ for events inside the signal region before the cut, for signal and background MC. . . . .	116
8.21	Best $\pi^0$ mass given by two random unpaired photons for events inside the signal region before the cut, for signal and background MC. . . . .	117
8.22	$m_{ee\gamma\gamma\gamma\gamma}$ in $GeV/c^2$ vs $p_t^2$ in $(GeV/c)^2$ for 1997 $K_L \rightarrow \pi^0\pi^0\pi_D^0$ MC after all cuts. The signal box is marked. . . . .	118
8.23	$m_{ee\gamma\gamma\gamma\gamma}$ in $GeV/c^2$ vs $p_t^2$ in $(GeV/c)^2$ for 1997 data after all cuts. The signal box is marked. . . . .	119
8.24	$m_{ee\gamma\gamma\gamma\gamma}$ in $GeV/c^2$ vs $p_t^2$ in $(GeV/c)^2$ for 1999 $K_L \rightarrow \pi^0\pi^0\pi_D^0$ MC after all cuts. The signal box is marked. . . . .	120
8.25	$m_{ee\gamma\gamma\gamma\gamma}$ in $GeV/c^2$ vs $p_t^2$ in $(GeV/c)^2$ for 1999 data after all cuts. The signal box is marked. . . . .	121
10.1	$m_{ee\gamma\gamma\gamma\gamma}$ (left) and $p_t^2$ (right) for 1999 MC events in the signal region after all cuts. . . . .	132
10.2	Confidence belt plot for the combined analysis. . . . .	133



# List of Tables

2.1	Relative populations of particle species surviving in the E799 beam. . . . .	15
5.1	Radiation lengths of elements of the charged particle spectrometer. . . . .	52
7.1	Number of events past each normalization mode cut, for data and $K_L \rightarrow \pi^0 \pi^0 \pi_D^0$ MC, for 1997. . . . .	70
7.2	Number of events past each normalization mode cut, for data and $K_L \rightarrow \pi^0 \pi^0 \pi_D^0$ MC, for 1999. . . . .	70
8.1	Total acceptance (in percent) of each analysis cut for 1997 signal and background Monte Carlo in the signal box, after the crunch and bad run/spill cuts . . . . .	95
8.2	Total acceptance (in percent) of each analysis cut for 1999 signal and background Monte Carlo in the signal region, after the crunch and bad run/spill cuts. . . . .	95

9.1	Systematic errors due to cuts done only on the normalization mode. . . . .	127
9.2	Effect of various backgrounds on the normalization mode, after all normalization mode cuts. . . . .	127

# Chapter 1

## Introduction

### 1.1 Introduction

This thesis describes a search for the rare particle decay  $K_L \rightarrow \pi^0 \pi_D^0 \gamma$  using data taken from the 1997 and 1999 runs of the KTeV experiment at the Fermi National Accelerator Laboratory. In searching for the decay, one photon from one pion was required to decay via a virtual gamma ( $\gamma^* \rightarrow e^+ e^-$ ) to satisfy the KTeV two charged-particle trigger. This decay (with a final state of 4 photons and two electrons) is difficult to detect because of the background, which is overwhelmingly due to  $K_L \rightarrow \pi^0 \pi^0 \pi_D^0$  events where one of the photons is missed. The essential method of this analysis is to design a series of cuts to select the  $K_L \rightarrow \pi^0 \pi_D^0 \gamma$  events while eliminating  $K_L \rightarrow \pi^0 \pi^0 \pi_D^0$  background events.

This chapter describes the physics of the neutral kaon system and of the decay  $K_L \rightarrow \pi^0 \pi_D^0 \gamma$ , as well as describing previous searches for the decay. The following chapters discuss the KTeV experiment

in detail and the methods used in this analysis.

## 1.2 The $K_L$ System and CP Violation

### 1.2.1 Symmetries: C, P and CP

It is an important fact of nature that physical interactions obey certain symmetries. Two important symmetries in particle physics involve the operators C (charge conjugation) and P (parity). The operator C acting on a particle state changes it to its anti-particle state, leaving spins and momenta unchanged. The operator P reverses the signs of all spatial dimensions; under P a particle state has its momentum reversed but retains the same spin and internal quantum numbers.

Until the 1950s it was assumed that all physical processes were symmetric under the action of the operators C and P. To the current level of experimental accuracy the strong and electromagnetic interactions are CP invariant, but the weak interaction maximally violates both C and P (as noted by Lee and Yang in 1956)<sup>1</sup>. However, even after the discovery of C and P non-invariance in the weak interactions, the combined operation CP was thought to be a good symmetry. That changed in 1964 when Cronin and Fitch discovered CP violation in neutral kaon decays<sup>2</sup>.

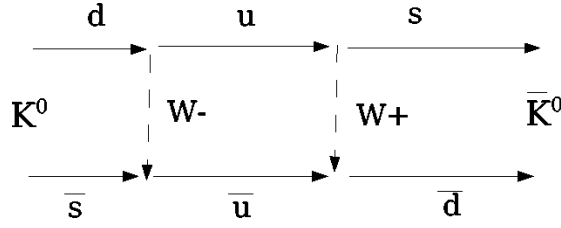


Figure 1.1: One of several diagrams contributing to oscillations between  $K^0$  and  $\bar{K}^0$ .

### 1.2.2 The $K^0$ $\bar{K}^0$ System

When neutral kaons are produced by strong interactions, they occur in one of two flavor eigenstates—the  $d\bar{s}$  eigenstate,  $K^0$ , and the  $s\bar{d}$  eigenstate,  $\bar{K}^0$ . However, since the weak interaction does not conserve flavor, the two eigenstates can change into each other by means of a second-order ( $\Delta S = 2$ ) weak process, as shown in figure 1.1.

Neutral kaons decay by the weak interaction, which does not conserve flavor. However, it does almost conserve CP. The  $K^0$  and  $\bar{K}^0$  states are eigenstates of P (with eigenvalue +1) but transform into each other under C, so that

$$\begin{aligned} \text{CP } |K^0\rangle &= |\bar{K}^0\rangle \\ \text{CP } |\bar{K}^0\rangle &= |K^0\rangle \end{aligned}$$

It is possible to construct eigenstates of CP,  $K_1$  (CP = 1) and  $K_2$  (CP = -1), using linear combinations of flavor eigenstates:<sup>3</sup>

$$\begin{aligned}
|K_1\rangle &= \frac{1}{\sqrt{2}}(|K^0\rangle + |\bar{K}^0\rangle) \\
|K_2\rangle &= \frac{1}{\sqrt{2}}(|K^0\rangle - |\bar{K}^0\rangle)
\end{aligned}$$

The near-preservation of CP by the weak interaction means that these states have very different lifetimes. If CP were exactly conserved, a  $|K_1\rangle$  could not decay into three pions ( a CP = -1 state), while a  $|K_2\rangle$  could not decay into two pions (a CP = 1 state). This means that, because the  $3\pi$  state is preferred for  $|K_2\rangle$ , the possible phase space for its decay is much smaller than that for  $|K_1\rangle$ , and so it should have a much longer lifetime. In experiments, such a lifetime difference was observed. The neutral kaon system was determined to consist of a long-lived state,  $K_L$ , with  $\tau_L = 5.17 \times 10^{-8}$  seconds, and a short lived state,  $K_S$ , with lifetime  $\tau_S = 8.93 \times 10^{-11}$  seconds <sup>4</sup>. The  $K_L$  and  $K_S$  particles are eigenstates of the weak interaction, and would correspond exactly to  $K_1$  and  $K_2$  if CP were conserved. The observation of  $K_L \rightarrow 2\pi^0$  decay by Cronin and Fitch proved that CP was violated in the weak interaction; the amount of violation is small (approximately on the level of  $2 \times 10^{-3}$ )<sup>5</sup>. It was therefore postulated that the weak decay eigenstates are admixtures of the CP eigenstates, characterized by a small complex parameter  $\epsilon$ :

$$|K_L\rangle = \frac{1}{1 + |\epsilon|^2}(|K_2\rangle + \epsilon |K_1\rangle)$$

$$|K_S\rangle = \frac{1}{1 + |\epsilon|^2}(|K_1\rangle + \epsilon |K_2\rangle)$$

This admixture of states is the mechanism behind indirect CP violation. The KTeV experiment has also found evidence<sup>6</sup> for a smaller amount of direct CP violation via the weak interaction in the kaon system. Direct CP violation consists of a state of definite CP decaying to one of opposite CP, e.g.  $K_2 \rightarrow 2\pi$ . In indirect CP violation, the definite CP state  $K_2$  would instead convert into the kaon state of opposite CP,  $K_1$ , before decaying; this is possible due to the fact that the weak decay eigenstates are not identical to the eigenstates of CP.

### 1.3 The Decay $K_L \rightarrow \pi^0 \pi^0 \gamma$

#### 1.3.1 Introduction to the Decay

The decay  $K_L \rightarrow \pi^0 \pi^0 \gamma$  cannot occur unless the pion pair has at least two units of relative angular momentum.<sup>7</sup> To understand this, note that the kaon has spin and total angular momentum 0 while the photon has spin 1. This means that the overall angular momentum conservation for the system (given a pion pair of angular momentum  $L^{\pi\pi}$  and a photon of angular momentum  $L^\gamma$ ) requires:

$$|0, 0\rangle \rightarrow |L^{\pi\pi}, L_z^{\pi\pi}\rangle |L^\gamma, L_z^\gamma\rangle$$

Where  $L_z^\gamma = -L_z^{\pi\pi}$ , is non-zero and so  $|L^{\pi\pi}| \geq 1$ . However, if  $L^{\pi\pi} = 1$ , the matrix element would be antisymmetric under interchange

of the two pions, Therefore this matrix element is forbidden by Bose statistics, and so the pion pair must have  $L \geq 2$ , and the photon must be at least E2 or M@.

The net effect of this requirement is to suppress the branching ratio of this decay compared to the kinematically similar decay  $K_L \rightarrow \pi^+\pi^-\gamma$ . By direct comparison of the matrix elements for  $K_L \rightarrow \pi^0\pi^0\gamma$  and  $K_L \rightarrow \pi^+\pi^-\gamma$  Sehgal<sup>8</sup> was able to estimate the total branching ratio of the decay  $K_L \rightarrow \pi^0\pi^0\gamma$  to be

$$BR(K_L \rightarrow \pi^0\pi^0\gamma) = 1 \times 10^{-8}$$

compared to  $2.9 \times 10^{-5}$  for  $K_L \rightarrow \pi^+\pi^-\gamma$ .

The lowest possible electric multipole in the perturbation expansion of this decay, given the orbital angular momentum of the pion pair, is the CP-conserving electric quadrupole term E2. Because of the rarity of the decay and the small value of the CP violation parameter  $\epsilon$ , the CP-violating M2 amplitude is ignored in this analysis. Also, because the directly emitted photon is real, there is no charge radius term in this decay—the J=0 transition from  $K_L$  to  $K_S$  cannot occur with emission of a real (J=1) photon. Therefore, this decay is treated as pure E2.



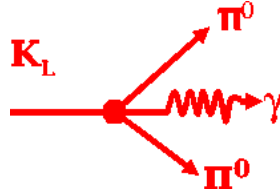


Figure 1.2: The Feynman diagram for the decay  $K_L \rightarrow \pi^0 \pi^0 \gamma$

### 1.3.2 Matrix Element and Decay Rate

The Feynman diagram for this decay is seen in figure 1.2. Heiliger and Sehgal determined the matrix element of  $K_L \rightarrow \pi^0 \pi^0 \gamma$  to be<sup>9</sup>

$$A(K_L \rightarrow \pi^0(p_1)\pi^0(p_2)\gamma(k)) = \frac{g_{E2}}{M_K^4} \frac{(p_1 - p_2) \cdot k}{\Lambda^2} (\epsilon \cdot p_1 k \cdot p_2 - \epsilon \cdot p_2 k \cdot p_1)$$

for the first order E2 transition, where  $p_1, p_2$  and  $k$  are the four-momenta of the indicated particles, and  $\epsilon$  is the photon polarization four-vector. (This matrix element is symmetric in the interchange of the two pions, as noted above.)

After squaring this matrix element and summing over photon polarizations, the differential decay rate for  $K_L \rightarrow \pi^0 \pi^0 \gamma$  was calculated to be (in the center of mass system of the  $K_L$ ):

$$\frac{d^2\Omega}{dE_\gamma d\beta} = \frac{g_{E2}^2 E_\gamma^4 |\vec{p}_1|^2 \sin(\beta^3)}{32\pi^3 \Lambda^4 M_K^7 E_1 E_2} ((E_1 - E_2) - (|\vec{p}_1| \cos(\beta) - |\vec{p}_2| \cos(\theta)))$$

where  $E_1$  and  $E_2$  are the energy of the two pions,  $\beta$  is the angle between the photon and one pion (the one with energy  $E_1$  and three-momentum  $\vec{p}_1$ ) and  $\theta$  is the angle between the photon and the other

pion. All quantities are in the kaon center of mass system.

### 1.3.3 The Decay $K_L \rightarrow \pi^0 \pi_D^0 \gamma$ as a Probe of Chiral Perturbation Theory

Chiral Perturbation Theory is an approximation used in the study of quantum chromodynamics, which treats long-distance interactions that are not calculable in closed form. The theory is based on the fact that if quarks were massless, the QCD Lagrangian would have chiral symmetry, i.e. the helicity of a quark would be conserved. Members of the pseudoscalar meson octet—kaons, pions and eta particles—would then be massless Goldstone bosons arising from the spontaneous breaking of the chiral symmetry by the QCD vacuum. The actual masses of these particles can be taken into account by explicitly breaking the chiral symmetry and putting the light quark masses ( $m_u$ ,  $m_d$  and  $m_s$ ) back into the Lagrangian. Since the pseudoscalar mesons interact weakly at low energy (below about 300 MeV), we can treat the breaking of the chiral symmetry as a perturbation of the chirally symmetric Lagrangian.<sup>10</sup> In chiral perturbation theory, the Lagrangian is expanded in terms of the quark masses and the interaction momentum; only even powers of the momentum occur in the expansion. The theory has been well tested to the fourth order ( $O(p^4)$ ), and has accurately predicted several neutral kaon parameters (such as the branching ratio of the decay  $K_S \rightarrow \gamma\gamma$ )<sup>11</sup>. The decay  $K_L \rightarrow \pi^0 \pi_D^0 \gamma$  is of interest to theo-

rists because it is forbidden in the second and fourth orders of chiral perturbation theory, making it a probe of the theory at the sixth order( $\mathcal{O}(p^6)$ )<sup>12</sup>.

#### 1.3.4 Previous Searches for the Decay

The upper limit on  $K_L \rightarrow \pi^0\pi^0\gamma$  was previously established by the NA31 experiment to be  $5 \times 10^{-6}$ .<sup>13</sup> (Unlike the present analysis, the NA31 search was for a final state with five photons; i.e. a state with no Dalitz pairs.).The KTeV experiment has produced an upper limit on  $K_L \rightarrow \pi^0\pi^0\gamma$  through a study of  $K_L \rightarrow \pi^0\pi^0e^+e^-$ . This study, done by Valeri Jejer using KTeV 1997 data, found<sup>14</sup>

$$BR(K_L \rightarrow \pi^0\pi^0e^+e^-) < 5.4 \times 10^{-9}$$

which implies (dividing by the Dalitz decay factor of 0.012)

$$BR(K_L \rightarrow \pi^0\pi^0\gamma) < 4.5 \times 10^{-7}$$

Jejer's result for  $K_L \rightarrow \pi^0\pi^0\gamma$  differs from the current result for several reasons. He used only the 1997 data set, while the current analysis uses both 1997 and 1999 data. The set of cuts that he used to distinguish signal from background was also different, since final-state particles must be paired differently in the reconstructions of  $K_L \rightarrow \pi^0\pi^0e^+e^-$  and  $K_L \rightarrow \pi^0\pi^0\gamma$ . In addition, the  $K_L \rightarrow \pi^0\pi^0e^+e^-$  mode proceeds via a charge radius process which

does not occur in  $K_L \rightarrow \pi^0 \pi^0 \gamma$ ; this is not taken into account in the above estimation of the  $K_L \rightarrow \pi^0 \pi^0 \gamma$  branching ratio.

## Chapter 2

# The KTeV detector

### 2.1 Introduction to KTeV

KTeV (short for "Kaons at the Tevatron") was a fixed-target experiment that ran in 1997 and 1999 at Fermi National Accelerator Laboratory. It was actually comprised of two separate experiments: E799 studied rare kaon and hyperon decays, while E832 was designed to measure the direct CP-violating parameter  $\text{Re}(\epsilon'/\epsilon)$ . This analysis is based on data collected from the E799 part of the experiment.

The primary difference between the two experiments was the use of an active regenerator to provide parallel  $K_S$  and  $K_L$  beams in E832. For E799 the regenerator was removed from the beam, providing two parallel  $K_L$  beams. In addition, a set of transition radiation detectors (TRDs) was added to the detector in 799 running to improve discrimination between electrons and charged pions. The experimental setup for E799 running is shown in 3-D in figure 2.1

and in cross-section in figure 2.2.

The actual operation of the E799 experiment took place over three distinct periods. The 'winter run', from January to March 1997; the 'summer run', from July to September 1997, and the '1999 run' from September 1999 to January 2000. The summer and winter runs are usually combined and called the '1997' run. This analysis uses data from the 1997 and 1999 runs of the E799 experiment.

## 2.2 Beam Production

The KTeV detector was located along the NM (neutrino-muon) fixed target beamline at the Fermilab Tevatron. The Tevatron accelerated protons to an energy of 800 GeV/c and extracted them to the NM beamline. The time required for the acceleration was 40 seconds; this is referred to as the off-spill period. The accelerated protons were continuously delivered to the beamline in the subsequent 'on-spill' period. The on-spill period lasted approximately 20 seconds in the 1997 run; it was doubled to approximately 40 seconds for 1999 to allow for more protons per spill.

In addition to the simple spill structure, the proton beam had a micro-structure. Protons were delivered in 1-2 ns pulses, spaced by 18.8 ns. Each micro-structure period was known as an RF (radio frequency) bucket. This bucket structure was caused by the use of RF accelerating cavities to accelerate the beam before injection. A

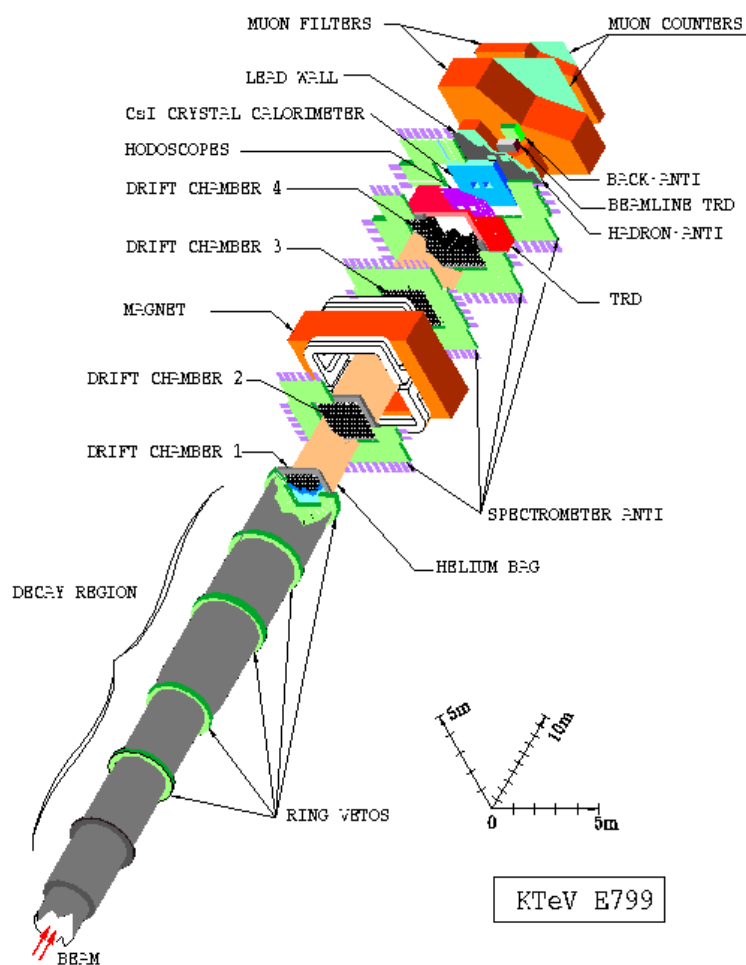


Figure 2.1: The KTeV detector for 799 running (3-D view).

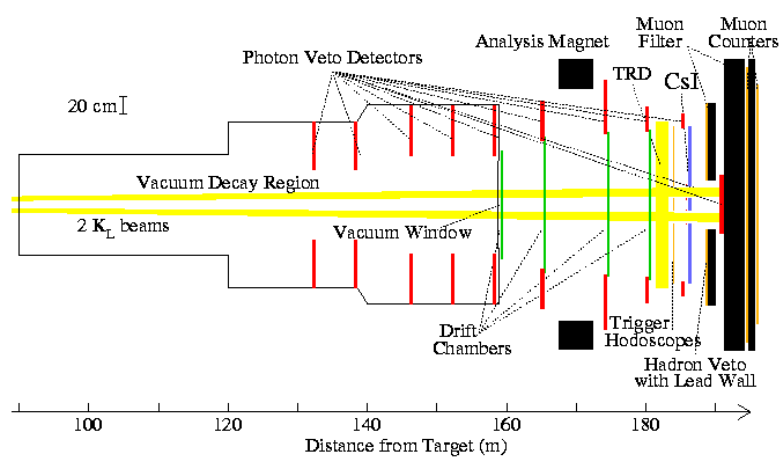


Figure 2.2: The KTeV detector for 799 running (plan view).



53.1 MHz signal corresponding to this microstructure was sent from the Tevatron to the detector, to synchronize the detector trigger with the arrival of the proton beam.

The beam intensity varied over the course of the experiment, but generally  $2 - 4 \times 10^{12}$  protons were delivered per spill in 1997. A larger number,  $6 - 10 \times 10^{12}$  delivered in 1999 was made possible by the doubled spill length.

The proton beam was focused to a diameter of  $250 \mu\text{m}$  and directed onto a rectangular BeO prism, which served as the primary kaon production target. (Beryllium oxide was chosen for its resistance to thermal stresses.) The target was located in the Fermilab beamline enclosure called NM2. The center of the target was the origin of the KTeV coordinate system; the +z direction was chosen as the downstream beam direction while the +y direction was up. The +x direction was chosen to make the system right-handed.

The BeO  $K_0\text{-}\overline{K}_0$  production target was 30 cm long and presented a 3mm by 3mm square cross-section to the incoming beam. The 30 cm length corresponded to 1.1 proton interaction lengths, which maximized kaon production efficiency. In addition, the incident proton beam was aimed downward (the -y direction) at an angle of 4.8 mrad, to optimize the kaon-neutron ratio in the produced beam (since neutrons tend to be produced more forward than kaons.)

A detector called the  $90^\circ$  target monitor was located near the

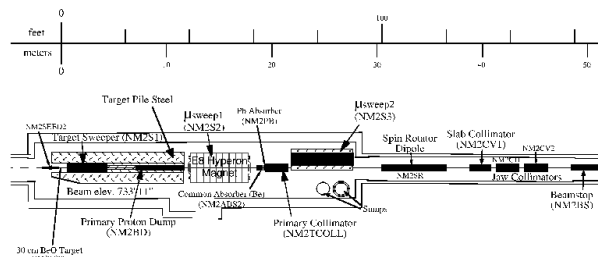


Figure 2.3: Y-view of beamline elements in the NM2 enclosure.

target and used to check for accidental beam activity. This detector consisted of three scintillator counters, located 1.8 m away from the target and aligned perpendicular to the beam direction. A coincidence in all three counters fired an accidental trigger, causing the event to be recorded for later use in Monte Carlo simulations.

## 2.3 Sweepers, Absorbers and Collimators

Many types of neutral and charged particles were produced by the proton interactions in the target; of these, only  $K_L$  particles were used in the analysis. The final neutral KTeV beam was extracted from these interaction products using a system of sweeper magnets, absorbers and collimators, all located inside NM2, to eliminate charged particles and photons. The arrangement of these detector elements is shown in figure 2.3.

The first sweeper magnet was the Target Sweeper, which was

located between 0.6 and 4.4 meters downstream of the BeO target and provided positive particles with a 475 MeV/c momentum kick in the +X direction. Charged particles that were swept out of the beam by this magnet were absorbed by the Primary Proton Dump, a water-cooled hunk of copper located below the primary beam, from 7.2 to 11.8 meters downstream . Neutral particles traveled unimpeded above the dump.

Downstream of the dump, a  $\mu$ -sweeper magnet gave positive particles a 3806 MeV/c kick in the +X direction. It was followed by the Pb-absorber, which was a 3-inch (14 photon radiation length) layer of lead at 19m downstream of the target, designed to absorb photons.

Following the absorber was the Primary Collimator, a piece of brass with two rectangular holes cut through it to shape two kaon beams. The size of the cylinders was 1.18cm by 1.29cm at the downstream face in the winter 1997 run; this was expanded to 1.62cm by 1.73 cm for the summer 1997 and 1999 runs.

After the Primary Collimator, there was a 5mm titanium vacuum window, followed by the  $\mu$ -sweep2 magnet (from 21.9 to 27.2 m downstream) to get rid of charged particles created in interactions with the absorber, collimator and window.

The Defining Collimator at 85-88 m downstream of the target resembled the Primary Collimator but was made of iron. Its aper-

tures were also larger; 4.4cm by 4.4cm for the downstream face in winter 1997, and 5.2 cm by 5.2 cm in summer 1997 and in 1999.

The final sweeper magnet extending from 90m to 93m downstream of the target followed the Defining Collimator. The beam then entered a 65m long,  $1.0 \times 10^{-6}$  torr vacuum region, where the kaon decays took place.

## 2.4 The Beam

After these collimators and sweeping magnets, the beam consisted mostly of  $K_L$  and neutrons, with neutrons dominating in a 3:1 ratio. However, neutrons did not generally decay in the KTeV detector due to their long lifetime, and so they only appeared as accidental interactions in the detector elements. There was also a small number of lambda and cascade hyperons remaining in the beam, as shown in table 2.1, as well as a small number of very high momentum ( $\geq 200$  GeV/c)  $K_S$  particles which survived from the target <sup>15</sup>. The total hadron rate in the secondary beam was 25-50 MHz.

Particle	Flux Relative to $K_L$
n	3.0-3.5
$K_L$	1
$\Lambda$	0.02
$\Xi$	0.0008

Table 2.1: Relative populations of particle species surviving in the E799 beam.

## 2.5 Vacuum Window and Ring Counters

The vacuum region was a long evacuated steel tank terminated at 159m from the target by a thin mylar-kevlar 'vacuum window', which prevented air from entering. This window was approximately 0.0015 radiation lengths thick. The tank diameter increased from 45cm to 2.4 meters along its length.

Inside the tank was a set of five scintillation detectors called 'ring counters' (RCs). The RCs, also called photon vetoes, had circular perimeters and square inner apertures; they were placed perpendicular to the beam-direction with their edges bordering the inner edge of the tank. The RCs were designed to detect photons (with energy greater than 100 MeV) escaping from the vacuum region.

The RCs consisted of 16 radiation lengths of lead-scintillator sandwich. Signals from the RCs were sent along glass fibers to phototubes mounted along the edge of each counter. The phototube signal was then digitized, discriminated and sent to the Level 1 trigger logic. Level 1 vetoed events with more than 0.5 GeV in any RC. The RC system provided hermetic coverage of escaping particles in the decay region.

## 2.6 Charged Particle Spectrometer

The KTeV charged particle spectrometer, located just downstream of the vacuum window, consisted of four drift chambers with

a magnet between chambers 2 and 3. The chambers were numbered from DC1 (upstream) to DC4 (downstream); for acceptance reasons their cross-sectional area increased with distance from the target. The spectrometer was used to measure the trajectories and momenta of charged particles from  $K_L$  decays. The location of the decay vertex could then be inferred by tracing back the charged particle trajectories.

### 2.6.1 Drift Chambers

A drift chamber uses the drift times of electrons in a gas to measure the position of an ionizing particle. Typically it consisted of a chamber filled with a gas which could be ionized by the passage of charged particles. Within the chamber were anode ("sense") and cathode ("field") wires, which were set up to have a uniform electric field between them. The passage of a charged particle through the gas liberated electrons from the gas atoms; these electrons then drifted towards the sense wires. By knowing the typical drift time for the gas, and by using scintillators to measure the exact time that the charged particle originally hit the chamber, it was possible to measure the position (in one dimension) of the original particle.

The KTeV drift chambers consisted of thick aluminum frames with mylar windows on each side. Plastic bags filled with helium were placed between the chambers, to reduce multiple scattering of

charged tracks compared to the scattering they would experience in air. Each chamber had four sense wire planes, two oriented in the y-direction (the "X-view") and two in the x-direction (the "Y-view"). This allowed construction of a three-dimensional trajectory. The sense wires were separated by 12.7 mm in each plane; the two planes in each view were staggered by one-half cell (6.35 mm), to resolve left/right ambiguity. (The "left-right ambiguity" refers to the fact that given a single hit on a drift chamber wire, it is impossible to know which side of the wire the charged particle originally passed through. Obviously, having two staggered sets of wires resolves this ambiguity.) The sense wires consisted of  $25\mu\text{m}$  diameter gold plated tungsten, while the surrounding field wires were  $100\mu\text{m}$  diameter gold plated aluminum. The field wires were arranged in a hexagonal pattern around the sense wire, making a drift cell that consisted of a right hexagonal prism. The arrangement of field and sense wires is shown in figure 2.4.

The normal voltage for the KTeV chambers was about 2500 V. The gas used was 49.75% argon, 49.75% ethane, with 0.5% isopropyl alcohol added to improve the lifespan of the chambers by absorbing damaging low-energy photons. The electron drift velocity was about  $50\mu\text{m}/\text{nsec}$ ; the maximum drift time across a cell was about 200ns.

The sense wire signals were amplified, discriminated and sent to time-to-digital converters (TDCs). The TDC for a sense wire began

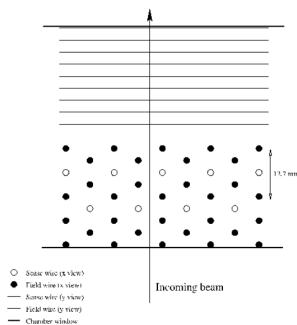


Figure 2.4: The field and sense wire arrangement within a drift chamber.

running when it received an input signal; later in the event all TDCs were stopped at once by a Level 1 trigger signal. The time recorded in the TDC was converted to a distance using standard conversion relations, which were calibrated throughout the run. (The raw sense wire signals were also fanned out to the Level 1 trigger logic.)

One requirement on drift chamber hits was the sum-of-distances for a hit pair (i.e. two hits in the same chamber and orientation from the same track) must add up to  $1/2$  the cell spacing. This "sod" distribution gave an idea of the position resolution of the drift chambers for good events. The resolution was on the order of  $100\mu\text{m}$  for most of the run, although it varied slightly due to changes in the voltage and gas composition throughout the run.



### 2.6.2 The Magnet

The KTeV analysis magnet provided a magnetic field of 2 kilogauss oriented in the vertical direction. The momentum kick in the x-direction due to the field was about 205 MeV/c in 1997; this was reduced to 150 MeV/c in 1999 to increase the four-track acceptance. The polarity of the magnet (and thus the direction of the kick) was frequently flipped during the run to eliminate any systematic effects due to the direction of deflection of positive and negative particles.

### 2.6.3 Momentum Resolution

The momentum resolution of the KTeV spectrometer was measured to be <sup>16</sup>

$$\frac{\sigma_p}{p} = 0.0016\%p + 0.38\%$$

where p is in GeV. The constant term was due to multiple scattering, while the term proportional to p was due to the finite position resolution of the detector. Since for high-momentum particles the magnet's momentum kick was small in comparison to the total momentum, the bend of the track due to the magnet was small and so the momentum measurement was less precise.

## 2.7 The Cesium Iodide Calorimeter

The CsI electromagnetic calorimeter was designed to measure the energies of incoming photons and electrons and was the primary KTeV detector for neutral particles.<sup>17</sup> The calorimeter, located at Z=186 meters, was 1.9 meters by 1.9 meters square and consisted of 3100 rectangular crystals (or "blocks") of cesium iodide. There were two types of crystals, differing only in size; 2232 "small" crystals (2.5 cm by 2.5 cm square) formed the center of the CsI detector while 868 "large" crystals (5.0 cm by 5.0 cm square) lined the edges. The crystals were 27 radiation lengths (50 cm) long, but only 1.4 nuclear interaction lengths; many hadrons passed through the calorimeter without interacting. Two "beam holes", 15cm by 15cm square, allowed the neutral beam to pass through without damaging the calorimeter. The arrangement of crystals in the CsI is shown in figure 2.5.

The light yield in each crystal was about 20 photoelectrons per MeV of deposited energy. There were two components to the scintillation light; a "fast" component which had a decay time of 25ns, and a "slow" component which had a decay time of  $1\mu\text{s}$ .

### 2.7.1 Crystal Readout

A transparent rubber "cookie" was attached to the back of each crystal to couple it to a photomultiplier tube (PMT). A filter was

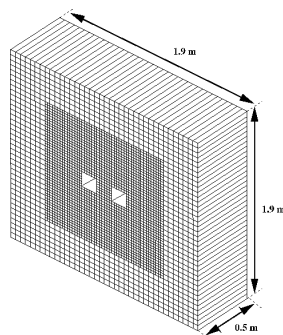


Figure 2.5: The size and structure of the CsI calorimeter.

placed on the cookie to eliminate the slow component of the scintillation light (possible since the slow and fast components were at different wavelengths.). The photomultiplier tubes ran at 900-1500 V and provided a typical gain of 5000. Their maximum current output was 30 mA, roughly corresponding to 80 GeV of energy deposited in one crystal.

The photomultiplier tube dynode signal was used in the Level 1 trigger logic. The anode signal was sent to a DPMT (Digital PMT) board for digitization. This custom board contained an 8-bit flash analog-to-digital converter (ADC), and two custom chips: the charge integrator and encoder (QIE) and the driver-buffer-clock (DBC).

The QIE divided the current from the PMT among eight capacitors, each receiving a fraction of the current ( $I/2$ ,  $I/4$ ... $I/256$ ). The voltage across each capacitor was integrated and compared to a set voltage range. If one of the capacitors was "in range" the charge

was processed by the ADC (resulting in an 8-bit "mantissa") and the identity of the capacitor was stored as a 3-bit exponent.<sup>18</sup> The digitization was a 4-stage process carried out in a round-robin fashion by 4 identical circuits for each DPMT chip. The circuit ran at 53 MHz; each integration period represented one RF bucket.

The mantissa, exponent and 2-bit circuit id number were stored in a FIFO (first-in, first-out) buffer in the DBC. If the Level 1 trigger was satisfied, data was read out to a holding buffer. On receipt of a Level 2 signal data in this buffer was sent to the "pipeline", which removed channels from the readout list if they were below a fixed threshold. This was done to reduce the data to a manageable size. The data in the pipeline was divided into 34 20 nanosecond "slices", corresponding to clock cycles of the DBC. The energy threshold and selection of slices to read could be set individually for each physics trigger.

### **2.7.2 Calibration**

A dye laser, tunable to a range of frequencies, was connected to each crystal using optical fibers. During special runs called laser scans, the response of each crystal across the entire DPMT dynamic range was scanned by tuning a variable filter wheel in front of the laser.

The conversion factor from charge to energy for each channel

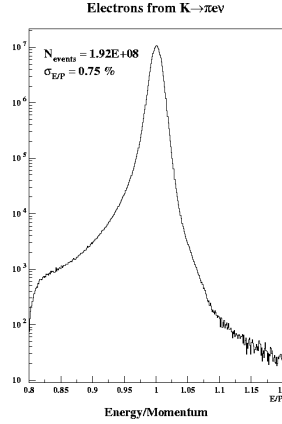


Figure 2.6: Energy/momentum distribution for electrons from  $K_{e3}$  decays. The peak at  $E/p = 1$  indicates that electrons deposit all their energy in the calorimeter. The width of the distribution is due to tracking and calorimeter resolution effects

( $Q/E$  constant) was found by studying the ratio of  $E/p$  for electrons from the  $K_{e3}$  decay. Here  $E$  is the electron energy from the calorimeter, and  $p$  is the corresponding spectrometer momentum.  $E/p$  was expected to be very near 1, since electrons deposit almost all of their energy in the CsI calorimeter. The  $Q/E$  constant for each channel was determined as the value which produced an  $E/p$  spectrum centered at 1 for  $K_{e3}$  electrons. The  $E/p$  spectrum after tuning is shown in figure 2.6.

### 2.7.3 Energy and Position Resolution

The energy resolution of the CsI was found to be<sup>19</sup>

$$\frac{\sigma_E}{E} = \frac{2\%}{\sqrt{E}} + 0.45\%$$

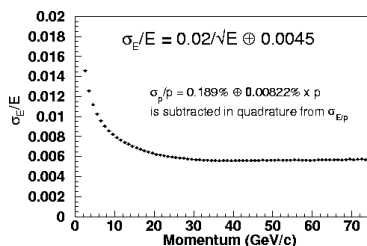


Figure 2.7: Calorimeter energy resolution as a function of track momentum, for electrons.

where  $E$  is in GeV. The constant term was caused by numerous effects such as light leakage, noise and crystal non-uniformity. The other term was due to the statistics of the scintillation light. This resolution is plotted in figure 2.7.

The position resolution was measured to be 1 mm in the small crystals, and 1.8 mm in the large crystals.

## 2.8 Other Parts of the Detector

### 2.8.1 The VV' Trigger Hodoscope

The Level 1 trigger needed information on the existence of charged decay products on a faster timescale than the drift chambers provided. This was provided by two sequential hodoscopes placed at  $Z=184$  m, labeled V (upstream) and V' (downstream). These detectors were 1.9 m by 1.9 m square. Each hodoscope consisted of a number (32 in V, 30 in V') of 1 cm scintillator paddles, in the orientation shown in figure 2.8. The different number, size and orientation of paddles in each plane was designed to prevent particles

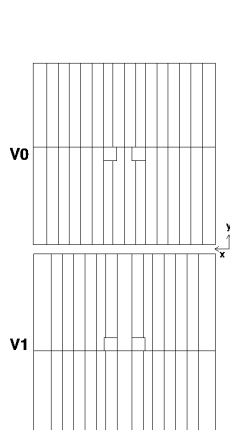


Figure 2.8: Structure of the VV' trigger hodoscope.

from slipping through cracks between paddles in both planes. The paddles were each instrumented with a photomultiplier tube. Both planes had two 15 cm by 15 cm square beam holes to allow passage of the neutral beams.

### 2.8.2 Transition Radiation Detectors

The TRDs were used to discriminate between charged pions and electrons. The TRD system consisted of eight planes, starting at 181.1 m from the target, each consisting of a polypropylene felt radiator followed by a multiwire proportional chamber. The X-ray signature detected by the MWPCs allowed discrimination of particle IDs, particularly between electrons and charged pions. The TRD system was not needed in this analysis.

### 2.8.3 The Hadron Anti

Just downstream of the calorimeter was positioned a 10cm thick lead wall. This had two purposes: to absorb EM shower energy which leaked from the calorimeter, and to induce hadronic showers for detection by the the Hadron Anti (HA). This detector was a plane of 28 scintillator paddles, 2.24 m by 2.24 m square. The sum of HA energy was sent to a trigger and provided a veto on hadron activity. A 1 meter thick steel wall, MUF1, protected the HA from backplash from the neutral beam dump. A beam hole, 64 cm in X and 34 cm in Y, was cut into the lead wall, HA and steel wall to allow passage of the neutral beam.

### 2.8.4 Beam Dump and Muon Detector

A 3 meter deep steel wall (MUF2) served as the neutral beam dump. A bank of 56 scintillator paddles downstream of MUF2 served as a muon veto (MU2). The paddles in MU2 overlapped by 1cm to prevent any cracks.

Downstream of MU2 was a 1 m thick steel wall, MUF3, followed by two muon identification planes, MU3X and MU3Y (together called MU3). They each contained 40 15cm wide scintillator panels. The muon detector was not used in this analysis.



### 2.8.5 Other Vetoes

The Spectrometer Antis (SA2-4) surrounded drift chambers 2-4 and were designed to measure particles leaving the detector. Like the RCs, they consisted of paddles of lead-scintillator sandwich 16 radiation lengths thick. The CsI Anti (CIA) was a similar detector around the face of the CsI calorimeter. Both the SA and CIA thresholds were set at 0.5 GeV.

The Collar Anti (CA) was designed to veto particles which hit the calorimeter near the beam holes. (Particles which hit the CsI near the hole could have mismeasured energies due to the leakage of shower energy into a hole.) The CA consisted of two 1.5cm wide square rings that framed the CsI beam holes. The rings consisted of 3 layers of tungsten-scintillator, for a total of 9.7 radiation lengths. The CA trigger threshold was set at 14 GeV. Signals from the SAs, CIA and CA were sent to the level 1 trigger as well as being recorded by ADCs.

The Back Anti(BA) was located on the face of MUF2 and designed to veto particles escaping down the beam hole. It consisted of thirty lead-scintillator layers (equivalent to 30 radiation lengths, or one nuclear interaction length). The BA was not used in this analysis. Although much of the background consisted of  $K_L \rightarrow \pi^0 \pi^0 \pi_D^0$  events with one photon lost down a beam hole, the constant dumping of the neutral beam in the BA caused it to be full of accidental

activity, making it difficult to use for efficient particle detection.

.

## Chapter 3

# Trigger and Event Selection

The kaon decay rate in the KTeV decay region was on the order of 1 MHz, which is far faster than events could be recorded. A multi-level trigger system was implemented to select events of interest to be recorded by the data acquisition system, or "DAQ". The trigger consisted of two levels of hardware, and a third software level to reject additional events in the DAQ.

The trigger system recorded events if they satisfied one of 16 possible sets of criteria, or "beam triggers". Only events which satisfied the 2E-NCLUS trigger (trigger one), requiring two charged tracks and at least four electromagnetic clusters in the calorimeter, are used in this analysis. After the 1997 run, and again after the 1999 run, an offline "crunch" code was run on all 2E-NCLUS events to further divide the sample into several categories (or "tags") based on event topology.

### 3.1 Level 1

Level 1 was a deadtimeless trigger which operated at the 53 MHz beam RF frequency. The Level 1 system made decisions based on simple logic operations using up to 96 input signals, or "sources", from various parts of the detector.<sup>20</sup> Except for the spill timing signals and the DC OR signals (discussed below), the signals from these sources were typically no more than 1 bucket (19ns) in length. The Level 1 logic units were located outside the detector hall; signals from different parts of the detector reached them approximately simultaneously through the use of delay cables. They were then synchronized with the 53 MHz spill signal.

The Level 1 trigger sources included many photon vetoes, such as the ring counters (RC6-10), the spectrometer anti (SA2-4), the calorimeter anti (CIA) and the collar antis (CA). These were designed to eliminate events with particles outside the acceptance of the spectrometer. In addition, accidental vetoes (such as the accidental muon counter) were used to eliminate events with accidental activity. The DC-OR signals allowed vetoing of events with insufficient drift chamber activity, as described below. Finally, four trigger sources (ET\_THR1 through ET\_THR4) corresponded to different minimum thresholds of total energy in the calorimeter. These thresholds were set to 10, 18, 25 and 38 GeV for 1997 running; for the 1999 run period, the first threshold was increased to 11 GeV

and the second reduced to 16 GeV. The total Level 1 trigger rate was approximately 60 KHz.

### **3.1.1 DC-OR signals**

The slowest component of the Level 1 trigger was the DC-OR system. Since any track in the drift chambers must pass between two sense wires, one of the two wire hits must arrive within half the maximum drift time of 200ns. By taking the logical OR of all sense wire pairs in each view of the first two drift chambers, DC1 and DC2, drift chamber information could be passed to the Level 1 trigger within 100ns of the particle passage.

The number of wire pairs hit in each view of DC1 and DC2 was counted by a central controller and sent to the level one trigger. This corresponded to eight possible Level 1 sources (two chambers, two views in each chamber, two possible states—1 hit or 2 or more hits—in each view).

### **3.1.2 The 2E-NCLUS Trigger**

During normal running there were 16 possible Level 1 triggers. This analysis uses data from one of these, the 2E-NCLUS trigger, with the following requirements:

- GATE: The spill is present
- !PHV: No CIA, SA, or RC (except RC8) with energy above 0.5 MeV;

- !CA: No CA with energy above 14 MeV;
- !MU2: No hit in the MU2 hodoscope plane;
- 2V: The VV' trigger hodoscope has at least two hits in V and one in V' or vice versa. This allows one charged particle to have gone through the cracks in the VV' detector.
- ET\_THR3: More than 25 GeV total raw energy in the CsI calorimeter
- DC12: At least one paddle hit in DC1 or DC2.

The MU2 requirement was removed during the 1997 winter run (run 8577) due to high accidental rates in MU2 . No cut was made on RC8 due to technical problems.

There were approximately  $3.8 \times 10^5$  L1 2E-NCLUS triggers per spill in the winter 1997 run. Changed trigger definitions resulted in  $4.3 \times 10^5$  L1 triggers per spill in the summer 1997 and 1999 runs.

## 3.2 Level 2

Events accepted by Level 1 were given to the Level 2 trigger, which was slower and more complex. Level 2 made decisions based on signals from the drift chambers, calorimeter and TRDs. The processing time for Level 2, which produced a dead time, was generally from 0.8 to 2.5  $\mu$  sec. The Level 2 event rate was about 10 KHz during normal running.

The Level 2 processors used in this analysis, the Hardware Cluster Counter (HCC) and the DC Hit Counters, are described below.

### 3.2.1 Hardware Cluster Counter

The Hardware Cluster Counter was used to quickly estimate the number of particles passing through the CsI calorimeter by reconstructing electromagnetic shower patterns.<sup>21</sup> It was the slowest part of the Level 2 logic, requiring  $2.2\mu\text{sec}$  to return a value. If the energy deposited in one calorimeter channel exceeded a preset threshold, an HCC bit for that channel was set in the Level 1 trigger. The threshold was nominally set to 1 GeV but was adjusted on a channel-by-channel basis every few months to counter gain loss from radiation damage to the calorimeter. The energy was also required to be deposited in the in-time window for that channel. This window was in phase with the 19ns RF clock signal; the width was different for each channel (depending on individual channel characteristics) but was typically from 6 to 10 ns.

The HCC bits set during an event formed clusters corresponding to the particles passing through the calorimeter. To count these clusters, a pattern matching algorithm was used. The algorithm looped over all possible  $2\times 2$  square groups of blocks in the calorimeter, so that each block was counted four times. Each  $2\times 2$  group was assigned a weight based on the pattern of hit blocks that it contained,

as shown in figure 1. This algorithm was designed so that any continuous group of hit blocks, regardless of shape, would produce a sum of weights equal to four. The sum of the weights for the entire calorimeter was divided by four to get the number of clusters and passed to the L2 trigger.

Clusters near the beam holes were found by treating the holes as if they were filled with "ghost blocks" with HCC bits off. Similar treatment was used to find clusters at the edge of the calorimeter. For clusters with both large and small blocks, one large block was treated as four small ones.

### **3.2.2 DC Hit Counters**

The DC hit counter system allowed Level 2 rejection of events with insufficient charged hits. Processors called "kumquats" did fast (205ns) counting of hits in each plane, while more complicated processors called "bananas" looked at the timing of the hits. The "bananas", which required 800ns of processing time, formed "hit pairs" by combining hits in each pair of planes, as will be described in more detail in chapter 4. The bananas then classified hit pairs as in-time or out-of-time and identified isolated hits. Hit pairs which were not in-time with the Level 1 trigger were rejected.



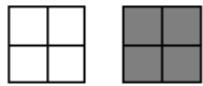
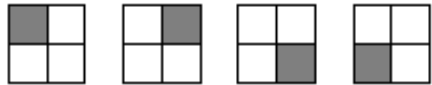
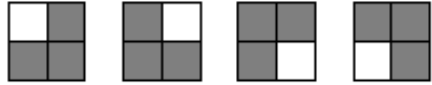
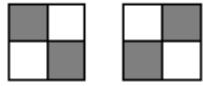
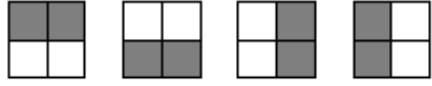
Hit block patterns	Pattern weight
	0
	+1
	-1
	+2
	0

Figure 3.1: Possible HCC bit patterns and corresponding weights for a 2 by 2 group of blocks. Filled blocks represent those with their HCC bits on. The sum of the weights taken over the entire array is 4 times the number of clusters

### 3.2.3 2E-NCLUS trigger: Level 2

The requirements for the 2E-NCLUS Level 2 trigger were as follows:

- HCC\_GE4: At least four HCC clusters were found
- 1HC2X: At least 1 Banana-accepted (i.e. in-time) hit pair in in the DC2 X-View
- 2HCY\_LOOSE: At least 2 hits in each Y view were found, but 1 missing hit in DC1Y or DC2Y (but not both) was allowed.

There were approximately 52000 Level 2 2E-NCLUS triggers per spill during the winter 1997 run, and 59000 in summer 1997 and 1999. The difference is caused by the change in Level 1 trigger definitions mentioned above; in both winter 1997 and summer 1997/1999, the number of level 2 triggers is 13.6% of the number of level 1 triggers.

## 3.3 Event Readout

After an event was accepted by Level 2 the data was digitized and sent into memory. This resulted in a 15-16  $\mu\text{sec}$  deadtime for each event. (Events which were rejected in level 2 were cleared by a fast  $0.5\mu\text{s}$  reset signal.)

The analog output of the TRDs and photon vetoes was digitized by FERA ADC modules, while latch modules recorded bitmasks of the L1 and L2 sources, beam triggers and calibration triggers fired

during an event. The total event, consisting of ADC, TDC, latch and pipelined CsI information, was then stored in one of four VME memory modules. The modules were read out by four SGI challenge computers, which ran the Level 3 trigger software.

### 3.4 Level 3

The Level 3 trigger was a software trigger that implemented a simple reconstruction of events.<sup>22</sup> (The reconstruction algorithms will be described in the next chapter.) The Level 3 trigger processed events from one spill over the entire on-spill and off-spill periods. If one spill was not processed before the next spill began, new triggers were inhibited, resulting in a deadtime period. However, the CPUs running the Level 3 code were optimized so that in practice, virtually no deadtime resulted from Level 3. The Level 3 trigger rate was approximately 0.7 KHz. Events which passed the Level 3 trigger were written to tape.

The following requirements were placed on 2E-NCLUS events in the Level 3 trigger:

- Must have at least two reconstructed tracks
- Must have at least one vertex candidate
- Both tracks must have  $E/p > 0.75$  (i.e. they are electrons)

Events which passed Level 3 were written to Digital Linear Tape

(DLT) drives. During the 1997 run events were recorded in order regardless of which trigger they satisfied. After the run the data sample was "split", or separated by trigger; this resulted in 98 tapes of 2E-NCLUS data. During the 1999 run, a more sophisticated tape writing system performed an "online" split, writing events from each trigger to different tape drives. There were 133 tapes of 2E-NCLUS data in 1999.

### 3.5 2E-NCLUS Crunch

After the data split, the 2E-NCLUS event sample was analyzed using a sophisticated crunch code. The code was designed to reconstruct event tracks, clusters and vertices in order to identify and tag several different physics modes.

The data sample used in this analysis consists of events with the 2PI0EE tag, which requires:

- 2 tracks
- 6 hardware clusters
- Tracks have opposite charge;
- Tracks have  $E/p > 0.9$ ;
- $p_t^2 < 0.001$ ;
- $m_{ee\gamma\gamma\gamma\gamma} > 0.44$

where  $p_t^2$  is the total transverse momentum squared of all the particles, defined with respect to the beam line.

After this crunch the final 1997 data sample consisted of 1.2 mil-

lion events corresponding to 3 DLT tapes. In 1999 it consisted of 1.8 million events corresponding to 5 DLT tapes.<sup>23</sup>

## Chapter 4

# Event Reconstruction

Each KTeV event contained about 6.5 kB of raw data, in the form of ADC, TDC and DPMT counts. It was necessary to reconstruct events using software routines designed to find drift chamber tracks and CsI clusters, and to find the probable location of the original kaon decay vertex.

This reconstruction was done using a program called KTEVANA. This program was created before KTeV began running and has been repeatedly modified and improved since then. This analysis uses two different versions of KTEVANA: version 6\_00 is used for 1997 events, while newer version 6\_04 is used in 1999 analysis. For event reconstruction, the primary differences between these two versions are a new treatment of the fringe magnetic field in the vacuum tank, a method of identifying photons that enter the CsI from inside a beam hole, and a slightly modified way of calculating the energy in the CsI clusters.

## 4.1 Tracking

The first stage of event reconstruction was using drift chamber information to re-create the tracks of charged particles. TDC counts from drift chamber wire hits were converted into drift distances using standard lookup maps. As mentioned in chapter 2, the wire TDCs began counting when a hit was received and were stopped by a common L1 stop signal; this resulted in a range of TDC stop times, as seen in figure 4.1. Hits with TDC times in the range  $115\text{ns} < t < 350\text{ns}$  were counted as "in-time". If there were multiple hits on a wire, the first in-time hit was recorded.

### 4.1.1 Hit Pairs and SODs

Any two in-time hits in adjacent wires of a plane pair were grouped together as a "hit pair". Hit pairs were classified by the sum of their drift distances, or SODs, which should equal the cell spacing (6.35 mm) if the hits were from the same track. Since the drift chamber resolution was  $100\mu\text{m}$ , the SOD resolution was  $\sqrt{2}$  times as large, or  $140\mu\text{m}$ . Hit pairs were classified as "good" if they had SODs within 1mm of the nominal value. The average of the two hit distances was used as the track position.

There were several cases in which the use of SODs could lead to tracking inefficiencies. If two tracks occupied the same cell, the SOD would be low because only the first in-time hit on each wire would

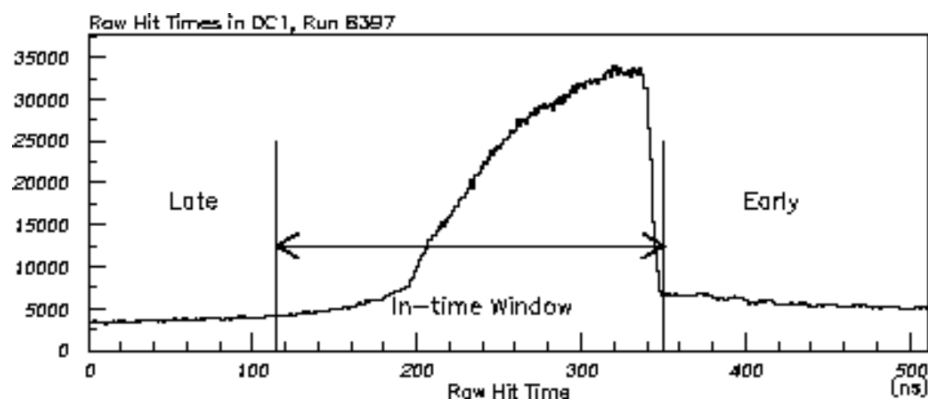


Figure 4.1: The arrival times of signals in DC1 during run 8397. Operated in common-stop mode, hits close to a wire start the TDC counting earlier than other hits and contribute to the "bluff" near 350 ns. Later hits trail off to the left.

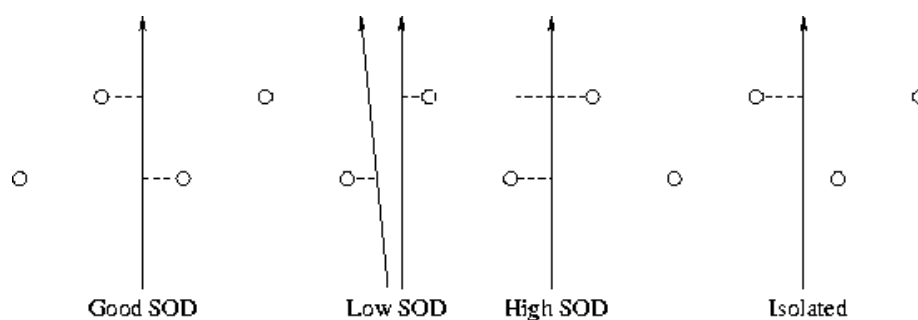


Figure 4.2: Categories of SODs from a charged track. Open circles represent sense wires, while the dashed lines are the inferred trajectories of the drift electrons.



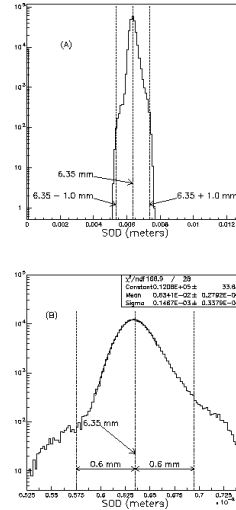


Figure 4.3: SOD distribution from a sample of  $K_L \rightarrow \pi^0 \pi_D^0$  events. The distribution is approximately centered on the cell spacing 6.35 mm. SODs within 1 mm of this value are accepted as "good". Isolated hits are located at 0mm on this plot. (The lower plot shows a Gaussian fit to the data.)

be used. High SOD pairs were generally caused by tracks passing too close to the sense wires. When this occurred, the drift electrons could not avalanche before striking the wire and so would not rise above threshold immediately, resulting in a delayed time measurement. Inefficiencies due to noise, insufficient gain and damage to the chambers could also lead to high SOD pairs or isolated hits, i.e. hits in only one plane of a chamber view. In the case of isolated hits, it was not possible to determine which side of the wire the track was on, and so both possibilities were considered. The method in which multiple tracks and inefficiencies give rise to high and low SODs and isolated hits is shown in figure 4.2. The SOD distribution from a sample of  $K_L \rightarrow \pi^0 \pi_D^0$  events is shown in figure 4.3.

### 4.1.2 y-track Finding

Track candidates were found separately in the x and y views. In the y-view, the hit pairs should lie in a straight line (since tracks are not bent in this direction by the magnet) with hits in all four chambers. Hit pairs in DC1 were matched with hit pairs in DC4 and a line was drawn between them; hits in DC2 and DC3 were required to lie within 5mm of this line. Track candidates were allowed to contain no more than two bad SODs, or one bad SOD and one isolated hit.

For candidates which matched these criteria, a straight line was fit to all four hits. A track  $\chi^2$  value was formed based on the distance of the hits from the fit line. Track candidates in y were required to have track  $\chi^2 < 4$ . Events with less than two y-track candidates were rejected.

### 4.1.3 x-track Finding

In the x-view, track segment candidates were found separately upstream and downstream of the magnet. Upstream segments could contain two bad SOD pairs, or one isolated hit; downstream segments were allowed one bad SOD pair or one isolated hit. The tracking routine then looked at all possible pairs of upstream and downstream segments, looking for pairs that intersected in the mid-plane of the magnet. Because of resolution effects, a 6mm "miss dis-

tance” was allowed. X-tracks (consisting of joined segments) were allowed only two bad SOD pairs, or one bad SOD and one isolated hit, between them. Events with less than two x-tracks were rejected.

The two sets of tracks (x and y) could not be associated with each other at this stage, and the combined tracks were not made until the vertexing stage.

## 4.2 Clustering

The clustering routine reconstructed the position and energy of particles which struck the calorimeter. The process consisted of four stages: hardware clustering, software clustering, cluster positioning, and corrections.

### 4.2.1 Hardware Clustering

The hardware clustering routine searched for local energy maxima among crystals with their HCC bits on (i.e. with more than 1 GeV of in-time energy). These blocks were designated as hardware cluster seeds. The raw energy of the hardware cluster was found by adding the energies from all channels in a grid around the seed block. For small crystals, a  $7 \times 7$  grid was used; for large ones a  $3 \times 3$  grid was used. At the large-small block boundary, a  $3 \times 3$  grid was used with four small blocks counting as a large block.

### 4.2.2 Software Clustering

Due to the requirement of 1 GeV of energy to set an HCC bit, hardware clustering could not find particle clusters below this energy. These might include low-energy bremsstrahlung photons, or minimum ionizing particles such as pions which left only a small fraction of their energy in the calorimeter. These clusters were found using software clustering. The software clustering algorithm looked for seed crystals (local maxima) with more than 50 MeV of energy, excluding hardware cluster seeds. Raw cluster energies were calculated using the same grid system as above. Software clusters were recorded only if the total raw energy exceeded 100 MeV.

### 4.2.3 Cluster Positioning

The exact location where a particle struck the calorimeter was often indeterminate, since the energy could be spread out over several blocks. To find the x-position, the ratio of the energy in the column containing the seed block to the energy in the adjacent columns was calculated. The ratio of these energies was compared to values in a look-up table which returned the cluster x-position. A similar process using rows found the y-position.

The lookup tables were determined experimentally by doing data and MC comparisons for the  $K_L \rightarrow \pi^0 \pi^0$  mode. They provided a position resolution of 1mm for small blocks, and 1.8 mm for large

blocks.

#### 4.2.4 Clustering Corrections

Several second-order corrections were made to the cluster energies after the basic cluster finding routine. These corrections are described below.

The **overlap correction** was used to separate clusters which shared crystals. It divided the energy of the common crystals between the clusters and recalculated the cluster energies and positions. The division was based on expected electromagnetic shower shapes found by using the GEANT simulation program.

The **neighbor correction** was used in cases where clusters did not overlap but were near each other and may have shared energy. It corrected the energy of the smaller cluster by assuming that a percentage of the larger cluster's energy leaked to it and subtracting the leaked energy from the total. Again, the shower shapes found by GEANT were used to calculate the probable amount of energy leakage.

The **intra-block correction** was applied to correct for varying responses across the face of the crystals. A map of the response across the face of each CsI block was made by considering each face to consist of 25 square bins of equal size, and measuring  $E/p$  in each bin for electrons from  $K_{e3}$  calibration decays. This map allowed the

energy of each cluster to be corrected by a factor corresponding to the response of its seed crystal.

The **non-linearity correction** was necessary due to variations in the longitudinal shower development in each crystal. The correction factors were found using GEANT shower simulations and the measured response in each crystal.

Clusters near a beam hole or the calorimeter edge could lose energy. The **missing block correction** estimated the amount of lost energy using GEANT shower simulations and added it to the cluster energy.

Energy lost in the beam hole could also reach crystals on the far side. If there was a cluster on this side of the beam hole, this "sneaky energy" could be added to its total energy. This effect was corrected for by the **sneaky energy correction**, based on studies of  $K_{e3}$  events near the beam hole.

CsI channels below a certain threshold were not read out. Since some of them may have been on the outer edges of clusters, this would have biased the cluster energy downward. The **threshold correction** counteracted this by adding an amount of energy  $E_{thr}$  to each channel in a cluster, where

$$E_{thr} = P_1(r) + P_2(r) \times \log(E)$$

Here  $P_1$  and  $P_2$  depend on the distance of the channel from the

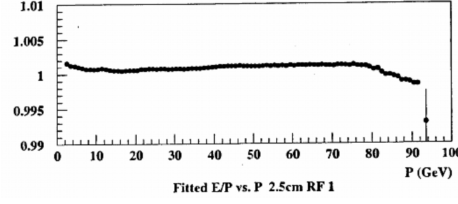


Figure 4.4: Mean  $E/p$  vs.  $p$  of calibration  $K_{e3}$  electrons in small blocks, after all clustering corrections after the linearity fudge. Residual non-linearities cause the mean to drift over the range of  $p$ . The linearity fudge uses this distribution to cancel out these residual effects

seed block. The values of these functions were determined during special runs with no readout threshold.

After all of these corrections, the mean value of the ratio  $E/p$  was plotted as a function of  $p$  for electrons. It should have been constant, but in fact it varied by a few tenths of a percent, as shown in figure 4.4. A **non-linearity fudge** factor, determined from the shape of the  $E/p$  vs.  $p$  plot, was used to cancel out this variation. Separate "fudge factors" were used for large and small blocks.

### 4.3 Vertexing

After the clustering, the vertexing routine was run to pair X- and Y-tracks and form a common decay vertex. First, the routine looped over all pairs of y-tracks, finding a range of Z-positions at which the two y-tracks may have intersected. It then did the same for all pairs of x-tracks. If the z-range for a y-track pair intersected that for an x-track pair, a combined nominal z-value was calculated and the point was considered to be a vertex candidate. (Vertex candidates

were required to have x-view tracks bending in opposite directions, i.e. to have oppositely charged particles.)

For each vertex candidate, the x- and y- tracks were then matched to each other using calorimeter clusters. The downstream part of both x- and y- tracks were projected onto the calorimeter, and the nearest cluster to each track was found. If any track was not within 7mm of a cluster, any vertex candidate including that track was rejected. For each surviving vertex candidate, each possible pairing of x-tracks with y-tracks was considered. The cluster closest to each pair was found, and the track-cluster distance was calculated. The x and y pairing that gives the smallest sum of squares of track-cluster distances was selected for that vertex candidate.

For any vertex candidate that passed the cluster matching criteria, a vertex  $\chi^2$  was calculated. This value was based on the matching of X and Y tracks, the matching of X segments at the magnet, and the number of bad SOD pairs or isolated hits used in tracks. The vertex candidate with the lowest  $\chi^2$  was accepted as the final vertex.

Finally, the momentum of the tracks was calculated. The bend angle of the track at the plane of the magnet was calculated, and the track momentum was just the (known) magnet momentum kick divided by this angle.

Figure 4.5 shows a completely reconstructed  $K_L \rightarrow \pi^+ \pi^- \gamma$  event.



The charged x- and y- tracks from the pions are shown on the lower right, and the pattern of hit blocks in the calorimeter is drawn on the upper right. The sidebar gives information about the event, including the reconstructed vertex position and vertex  $\chi^2$ .

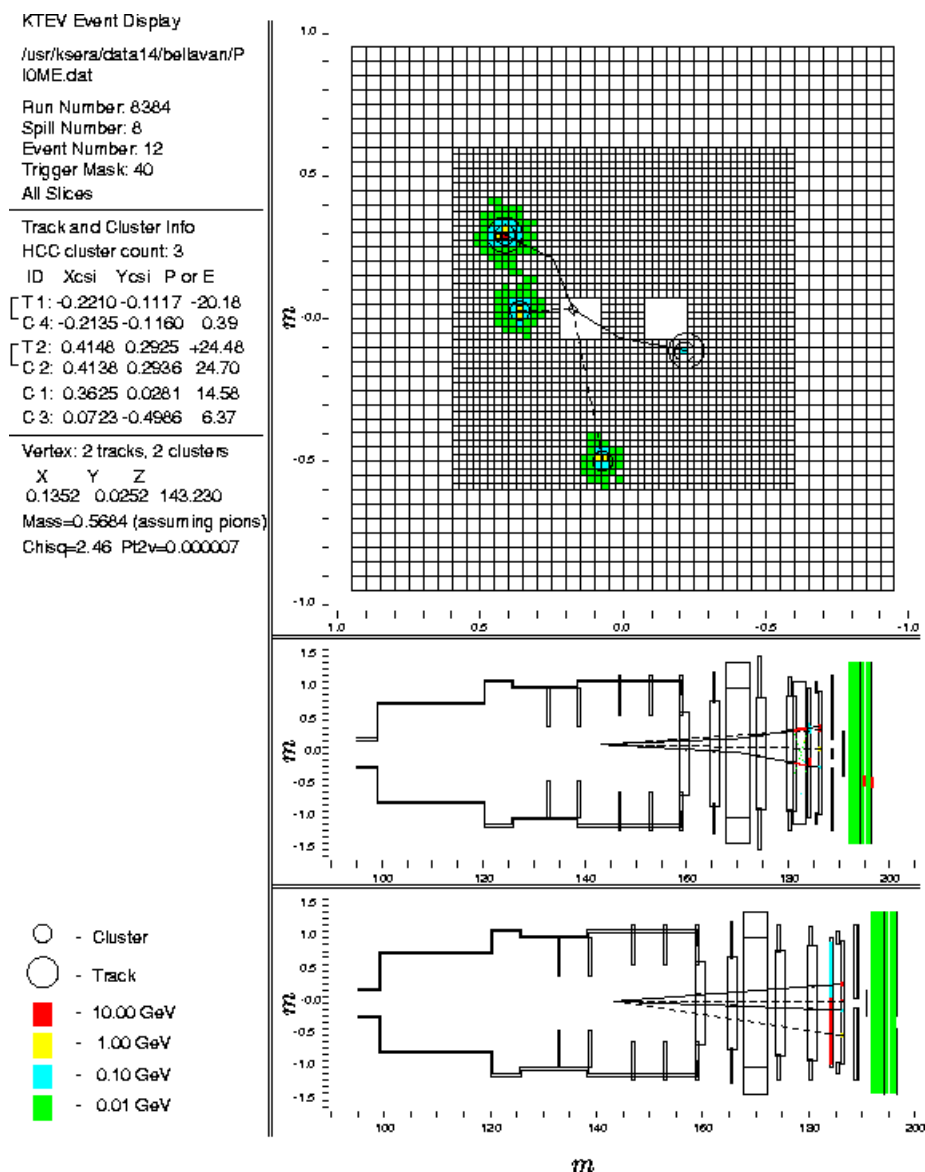


Figure 4.5: A completely reconstructed event displayed using the KDISP program.

## Chapter 5

# KTeV Monte Carlo

In addition to the data sample, the analysis code was run on samples of simulated data generated by a Monte Carlo program. The KTeV Monte Carlo generated a neutral  $K_L$  beam using a momentum spectrum derived from measured  $K_L \rightarrow \pi^+\pi^-$  decays. It then allowed the kaons to decay into a specific mode (or modes) chosen by the user and traced the decay products through a simulation of the KTeV detector. In this analysis two major Monte Carlo decay samples were generated; the signal  $K_L \rightarrow \pi^0\pi_D^0\gamma$  and the normalization sample,  $K_L \rightarrow \pi^0\pi^0\pi_D^0$  (which was also the major background). For the signal mode analysis, cuts were tuned to eliminate  $K_L \rightarrow \pi^0\pi^0\pi_D^0$  events while preserving  $K_L \rightarrow \pi^0\pi_D^0\gamma$  events. To obtain the normalization sample, cuts were designed to preserve  $K_L \rightarrow \pi^0\pi^0\pi_D^0$  events with a clean signature. The final efficiencies for both samples were used to calculate the single event sensitivity and expected background level. In addition, the normalization sam-

ple allowed us to test the Monte Carlo simulation of the detector by comparing data and Monte Carlo events .

## 5.1 Simulation of Kaon Production

The first step in the Monte Carlo was  $K^0 - \bar{K}^0$  production at the BeO target. The particle production cross section for protons on a beryllium target was given by Malensek as<sup>24</sup>:

$$\frac{d^2N}{dP d\Omega} = \frac{Bx}{800\pi} \frac{(1-x)^A (1+5e^{-Dx})}{(1+P_t^2/M^2)}$$

where P is the lab frame momentum of the produced particles, x is the ratio of P to the momentum of protons incident on the target, and  $P_t$  is the transverse momentum of the produced particles with respect to the incoming protons. B, A, D, and M are constants determined by fitting data for various particle types produced in proton interactions.

The Malensk spectrum has been measured only for charged kaon production. However, the neutral kaon production spectrum can be arrived at by a quark counting argument, which allows us to relate the production cross sections for neutral and charged kaons:

$$\begin{aligned} K^0 &\sim \frac{1}{2}(K^+ + K^-) \\ \bar{K}^0 &\sim K^- \end{aligned}$$

These relations predict a mixture of 55%  $K^0$ , 45%  $\overline{K}^0$ . The Malensk spectrum parameters were tuned using KTeV data from  $K_L \rightarrow \pi^+\pi^-$  decays, which resulted in a 5-10% correction.

The kaon momentum was required to be within a specified range of 20 to 220 GeV/c for both the signal and normalization modes. After generation, the kaons were allowed to decay, with the decay z-positions given by a decay probability distribution input into KTEVMC. Kaons which hit the primary collimator were terminated; kaons which hit the defining collimator were either terminated or allowed to scatter.

The kaon state is a superposition of  $K_S$  and  $K_L$  states, which can be considered as a column vector:

$$\begin{pmatrix} A_S(t) \\ A_L(t) \end{pmatrix}$$

The production states in the target are:

$$K^0 = \begin{pmatrix} +1 \\ +1 \end{pmatrix}$$

and

$$\overline{K}^0 = \begin{pmatrix} +1 \\ -1 \end{pmatrix}$$

In vacuum, the kaon state is evolved in time using the mass matrix:

$$\begin{pmatrix} e^{-(im_S + \Gamma_S/2)t} & 0 \\ 0 & e^{-(im_L + \Gamma_L/2)t} \end{pmatrix}$$

where  $t$  is the particle's proper time,  $m_S$  and  $m_L$  are the masses of the  $K_S$  and  $K_L$ , and  $\Gamma_S$  and  $\Gamma_L$  are the corresponding decay rates. Since the decay region began 90m away from the target, the final state was almost entirely  $K_L$ , except at very high energies ( $\geq 200$  GeV).

## 5.2 Simulation of $K_L$ Decay

Decays of the  $K_L$  were generated in Monte Carlo using probability distributions, based on physics parameters, which can be modified by the user. In some cases these reflected calculated decay rates with full matrix elements; in others they consisted only of phase space calculations.

### 5.2.1 $K_L \rightarrow \pi^0 \pi^0 \gamma$ Generation

The signal mode  $K_L \rightarrow \pi^0 \pi^0 \gamma$  was generated using a differential decay rate that was calculated as described in chapter 1. As calculated by Heilliger and Sehgal<sup>25</sup>, this produced a photon energy spectrum given by

$$\frac{d\Gamma}{d\Omega} = \frac{g_{E2}^2}{\Lambda^4} \frac{1}{3840\pi^3 M_K^3} \left(1 - \frac{2\omega}{M_K}\right) \beta^5 \omega^5$$

where  $g_{E2}$  is a constant with dimensions of mass,  $\omega$  is the photon energy,  $\Lambda$  is a mass parameter that characterizes the size of the decay region ( $R \sim \Lambda^{-1}$ ), and  $\beta$  is given by:

$$\beta = \left( \frac{M_K^2 - 2M_K\omega - 4m_\pi^2}{M_K^2 - 2M_K \times \omega} \right)$$

### 5.2.2 $K_L \rightarrow \pi^0\pi^0\pi^0$ Generation

The background decay  $K_L \rightarrow \pi^0\pi^0\pi^0$  was generated using a flat phase-space distribution. Since the effects of the measured form factor are small, this was considered sufficient.

### 5.2.3 $\pi^0 \rightarrow e^+e^-\gamma$ Dalitz Decay

Both signal and background mode events were required to have a pion Dalitz decay. Since this is an electromagnetic decay,  $c\tau$  for the pion is only 25nm, and the pion was assumed to decay at point it was produced. The KTeV Monte Carlo generated this decay using the Kroll-Wada matrix element<sup>26</sup>, with an experimentally determined form factor

$$f(x) = 1 + ax, x = \frac{M_{ee}^2}{M_{\pi^0}^2}$$

where  $a$  is measured to be  $0.032 \pm 0.004$ .

Radiative corrections such as  $\pi^0 \rightarrow e^+e^-\gamma\gamma$  are important in this mode as well. Only the tree-level  $\pi^0 \rightarrow e^+e^-\gamma\gamma$  matrix element is considered in generating the radiative decay. An  $M_{\gamma\gamma} > 1$  MeV cutoff is implemented in the Monte Carlo to avoid divergences. With this cutoff, the probability of radiation from any generated  $\pi^0 \rightarrow e^+e^-\gamma$  event is 16.2%<sup>27</sup>. Despite this large percentage, including radiative corrections with this cutoff raises the total  $\pi^0 \rightarrow e^+e^-\gamma$  branching ratio only slightly, from 1.185% to 1.193%.

### 5.3 Particle Tracing

After generation, the daughter particles were rotated by a random angle about the kaon momentum axis, and were boosted into the lab frame. Particles were then traced through the KTeV detector. The tracing occurred in sequential steps of  $z$ ; at each step the particle's interaction with the corresponding detector element was simulated, along with the detector response. Particles were traced until they were absorbed by the calorimeter, struck a veto or left the detector. Particles which left the detector were considered lost.

### 5.4 Particle Interactions

#### 5.4.1 Photon Conversion

Photons with energy greater than 100 MeV were allowed to convert into an  $e^+e^-$  pair in interactions with the detector elements.



The conversion probability in each detector element was given by

$$P_{conv} = 1 - e^{-\frac{7}{9}(X/X_0)}$$

where  $X$  is the distance the photon travels in the element and  $X_0$  is the element's characteristic radiation length. The  $z$  position of conversion within the element was selected randomly.

The energy of the photon was split according to the Bethe-Heitler spectrum:

$$P(\epsilon_+, \epsilon_-) \approx \epsilon_+^2 + \epsilon_-^2 + \left(\frac{2}{3} - \frac{1}{9\sigma}\right)\epsilon_- \epsilon_+$$

where  $\epsilon_{\pm} = E_{e\pm}/E_{\gamma}$  and  $\sigma$  is a known constant ( $\approx 3.7$ ). The electron and positron directions were offset by a small angle, rotated by a random amount about the axis of the parent photon direction.<sup>28</sup>

#### 5.4.2 Multiple Scattering

Charged particles passing through matter are continuously deflected by Coulomb interactions with nuclei. To simulate this, the KTeV Monte Carlo chose a random scattering angle  $\theta$  immediately after a charged particle left a detector element. The probability spectrum for  $\theta$  was a Gaussian with mean 0 and width  $\theta_0$  taken from the Moliere distribution:

$$\theta_0 = \frac{13.6 \text{ MeV}}{\beta} z \sqrt{X/X_0} [1 + 0.038 \ln(X/X_0)]$$

where  $p$ ,  $\beta$ , and  $z$  are the momentum (in GeV), velocity and charge (in units of the electron charge) of the scattered particle,  $X$  is the distance travelled in the element and  $X_0$  is the element's radiation length. The direction of scatter was randomly chosen.

### 5.4.3 Bremsstrahlung

Electrons and positrons were allowed to radiate one bremsstrahlung photon as they traversed a detector element. Assuming that the particles are ultrarelativistic, and that the Born approximation is valid, the probability of emission of a photon of momentum  $k > k_0$  (where  $k_0$  is a cutoff value) is

$$P_{k>k_0} = \frac{X}{X_0} \frac{1}{18\zeta + 1} [2(12\zeta + 1)(k_0/E_0 - \ln(k_0/E_0) - 1) + 9\zeta(1 - (k_0/E_0)^2)]$$

where  $\zeta = \ln(183/Z^{1/3})$ , and  $E_0$  is the initial energy of the electron. The cutoff in the KTeV Monte Carlo was  $k_0 = 0.001E_0$ .

The expression for the differential momentum spectrum and angular distribution of the radiated photon is complex and is described in ref. 29<sup>29</sup>. To conserve computation time, the full angular simulation was performed only if the radiation occurred upstream of the analysis magnet (in which case the photon and electron would

be well separated at the calorimeter) and if  $E_0 > 1.5$  GeV. Otherwise, a simpler formula was used for the momentum spectrum of the radiated photon <sup>30</sup>.

## 5.5 Detector Simulation

After generation, the products of the  $K_L$  decay passed through a detailed simulation of the KTeV detector. Only the parts used in this analysis are described below; however, all parts of the detector were simulated and could contribute to multiple scattering, photon conversion and bremsstrahlung energy loss.

### 5.5.1 Photon Vetoes and VV' counter

The photon vetoes were simulated by stopping a particle which hit a veto at the veto face; the energy of the particle was Gaussian smeared to account for the detector resolution. Events which had smeared energy in any veto above the Level 1 trigger threshold were rejected immediately to save processing time.

Charged particles which crossed a VV' hodoscope counter generated a pulse for that counter. The counter inefficiencies were simulated by generating a random number for each particles hitting a counter and comparing it to the measured counter efficiency to see if the hit was registered. The cracks between VV' paddles were also accounted for in the simulation. The VV' hodoscope represented a

radiation length of  $0.02X_0$ .

### 5.5.2 Charged Particle Spectrometer Simulation

When a charged particle passed through the drift chambers, hits were recorded in each plane in the sense wire closest to the particle trajectory. The distance between the particle and the wire was Gaussian smeared to account for the finite position resolution of the detector. The sum-of-distances (SODs) for each hit pair were calculated and drift distances were correlated to drift times using the XT maps. Corrections were applied to the simulated SODs to reproduce the high-SOD tail in the data. Extra hits due to 'knock-on' electrons, or  $\delta$  rays, were also simulated.

After all of these corrections, there were still significant data/MC tracking discrepancies due to inaccurate simulation of isolated hits and high SOD pairs. To eliminate this disagreement, DC maps were generated which described isolated hit and high SOD probabilities as a function of wire position and time within the run. The DC maps were applied after all other corrections and greatly improved data/MC agreement.

The magnet was simulated by giving a  $\pm x$  direction transverse momentum kick to charged particles as they crossed the magnet plane. The exact value of the magnet kick was measured periodically during KTeV running by measuring the invariant mass of

reconstructed calibration  $K_L \rightarrow \pi^+\pi^-$  events. These values were put into a database and used in Monte Carlo generation and event reconstruction.

Radiation in the spectrometer was simulated at discrete planes which contained the "compressed" radiation lengths of the surrounding regions, listed in table 5.1. The combined radiation length of the vacuum window, the air gap and the upstream part of DC1 was measured by studying photon conversions in  $3\pi^0$  decays<sup>31</sup>. Since the radiation lengths of the vacuum window and DC1 can be calculated, this effectively measured the amount of material in the air gap. Each drift chamber was modeled as two planes of material, one at the upstream face of the chamber and one at the downstream face. The calculated radiation thickness of the chamber material was divided evenly between the two planes. The helium bags were treated as four planes of material; the radiation thickness was calculated assuming the bags were 97% helium and 3% air. (These percentages were determined by studying the effect of multiple scattering on track resolution for low-momentum tracks.)

### 5.5.3 TRDs

Although the TRDs were not actively used in this analysis, they still represented material in which photon conversions and multiple scattering could occur. The TRDs were simulated as eight planes

Material Simulated	Z position (m)	Total Rad. Thickness ( $X_0$ )
Vacuum window	158.89	0.00156
" Air Gap"	159.25	0.00147
Drift Chamber 1	159.40	0.00050
	159.48	0.00045
Helium Bag 2	159.48 to 165.55	0.00162
Drift Chamber 2	165.55	0.00045
	165.63	0.00045
Helium Bag 3 before magnet	165.3 to 170.01	0.00119
Helium Bag 3 after magnet	170.01 to 173.99	0.00119
Drift Chamber 3	174.65	0.00090
Helium Bag 4	174.65 to 180.02	0.00156
Drift Chamber 4	180.55	0.00090

Table 5.1: Radiation lengths of elements of the charged particle spectrometer. Radiation lengths are modeled as planes that contain the compressed amount of material from the surrounding regions. The helium bags are modeled with four such planes to better simulate the continuous nature of the physical regions.

located from  $Z=181.1\text{m}$  to  $Z=183.4\text{ m}$ . The total radiation length of the TRD system was calculated to be  $0.14X_0$  outside the beam region, where there was radiator material. Inside the beam region the total radiation length was  $0.04X_0$ .

#### 5.5.4 Calorimeter Simulation

The tracing of photons and electrons was stopped at the CsI calorimeter face. The energy of the incident photon or electron was smeared to account for resolution effects; the smearing depended on the measured resolution of the hit block.

#### EM Showers

Photons and electrons passing through the CsI deposited energy in the form of electromagnetic showers. Since it would have been

time-consuming to generate simulated EM showers in the CsI blocks for every MC event, a fixed shower library was used. This library was created using GEANT simulations of a  $32.5 \text{ cm} \times 32.5 \text{ cm}$  array of crystals (corresponding to  $13 \times 13$  small blocks; large blocks were counted as 4 small blocks). The showers were classified according to the incident particle energy (6 bins, with upper bounds of 2, 4, 8, 16, 32, and 64 GeV) and the x and y position of the shower within the block (325 bins). Since there were 5 showers in each energy-position bin, a total of 9,750 showers comprised the library.

When a particle hit the CsI, the mean longitudinal shower position within the crystal,  $\bar{z}$ , was calculated. This distribution was different for electrons and photons:

$$\bar{z}_e = 0.11 + 0.18 \ln E_e$$

$$\bar{z}_\gamma = 0.12 + 0.18 \ln E_\gamma$$

where  $\bar{z}$  is in meters and  $E$  is in GeV.

Following this step, a shower was selected from the library, based on the particle energy and its x and y position when projected to  $\bar{z}$ . The shower energy was scaled to match the smeared energy of the incident particle. Energy from showers bordering a beam hole was allowed to 'sneak' across to crystals on the opposite side of the hole. This effect was simulated using distributions of "sneaky energy" measured using  $K_{e3}$  data. The measured longitudinal response of

each shower crystal was convoluted with the shower's longitudinal energy distribution in that crystal to determine the total response of each crystal.

### **Digitization and Readout Simulation**

After the shower simulation, events were digitized as described in chapter 2 using a simulation of the phototubes and DPMT board. The energy from each photon was converted into a charge and spread out over a series of time slices, using pulse shape distributions measured from the data. The charge from each phototube was smeared to account for the effects of photostatistics.

## **5.6 Accidental Overlays**

In order to have an accurate simulation, it is necessary to account for accidental effects in the detector. These include beam interactions, cosmic rays, and extra particles produced in the target and vacuum window. This accidental activity could affect the drift chambers, calorimeter or photon vetoes, producing tracking inefficiencies, mismeasurement of cluster energies and even accidentally firing L1 trigger sources.

During KTeV running, a special trigger recorded events containing only accidental activity. These events were stored on disk and were used as overlays during Monte Carlo generation. Upon generation of an MC event, an accidental event was randomly selected.



ADC values (such as photon veto energies) from the accidental event were directly added to those from the generated event; calorimeter crystal energies were added on a slice-by-slice basis TDC entries (such as DC hits) from the accidental event were added to the list of those in the general event.

## 5.7 Trigger Simulation

The trigger definitions used in the Monte Carlo were identical to those used during data taking. Photon veto trigger sources were evaluated during generation to save computing time; the other L1 triggers were processed after event generation. The L2 and L3 triggers were implemented by software routines. Events which passed the L3 trigger were written to disk in the same format as the data.

## 5.8 Monte Carlo Samples

For this analysis, two major samples of Monte Carlo were generated; the signal mode  $K_L \rightarrow \pi^0 \pi_D^0 \gamma$  and the major background  $K_L \rightarrow \pi^0 \pi^0 \pi_D^0$ , which was also the normalization mode. For  $K_L \rightarrow \pi^0 \pi_D^0 \gamma$ , 25 million events were produced for 1997 running and 25 million for 1999, for a total of 50 million. For  $K_L \rightarrow \pi^0 \pi^0 \pi_D^0$ , 8.66 billion events were generated for 1997 running and 10.42 billion for 1999, for a total of 19.08 billion. Generation was done using KTEVANA version 6\_00 for 1997 and version 6\_04 for 1999. ( The newer version in-

cludes more accurate simulation of bremsstrahlung, delta rays, and photon conversions in the helium bags.)

### 5.8.1 2E-NCLUS Trigger and Crunch

Generated MC events were required to pass through the level 1 and level 2 2E-NCLUS triggers (as described in chapter 3). For 1997 running, 6.54% of generated  $K_L \rightarrow \pi^0 \pi_D^0 \gamma$  passed the trigger requirements, compared with 5.94% of generated  $K_L \rightarrow \pi^0 \pi^0 \pi_D^0$  events. For 1999 running, these percentages were higher: 8.37% of generated  $K_L \rightarrow \pi^0 \pi_D^0 \gamma$  passed the trigger requirements, compared with 7.38% of generated  $K_L \rightarrow \pi^0 \pi^0 \pi_D^0$  events. The increased 1999 acceptance was due to the fact that the magnetic field was lower in 1999 than in 1997, making it less likely that electrons or positrons would be swept out of detector.

These Monte Carlo samples were then passed through a slightly modified version of the 2E-NCLUS crunch cuts described in chapter 3. The only change was in the track energy/momentum requirement ( $E/p$ ); events were accepted if they had  $0.95 < E/p < 1.05$  for both tracks. In addition, events were rejected if they came from a "bad" run or spill, i.e. one which had a known detector problem. For the signal  $K_L \rightarrow \pi^0 \pi_D^0 \gamma$  mode, 201736 events passed the crunch in 1997 and 312329 in 1999. For the primary background mode  $K_L \rightarrow \pi^0 \pi^0 \pi_D^0$ , 3.2 million events passed the crunch in 1997, while

6.2 million did in 1999.

The new  $E/p$  cut and the bad runs/bad spills cut were applied to the crunched data as well. For 1997 data, 712499 events survived this stage of the analysis; for 1999 data, 1.6 million events did.

## Chapter 6

# The Combined Vertexing Routine

In KTEVANA, the  $K_L$  decay vertex is usually found simply as the intersection point of the charged particle tracks in the drift chamber. However, in modes with two tracks this "charged vertex" has a large uncertainty if the opening angle between tracks is small. In this case the fixed error in the drift chamber resolution produces a large error in the z-vertex projection.

To avoid this problem, a combined vertexing routine written by Alexander Ledovsky<sup>32</sup> was run on all events—data,  $K_L \rightarrow \pi^0 \pi^0 \pi_D^0$  MC and  $K_L \rightarrow \pi^0 \pi_D^0 \gamma$  MC, immediately following the crunch. (The word "combined" refers to the fact that both neutral and charged particle information is used in finding the vertex.)

The combined vertexing routine works by considering all possible particle combinations—that is, all possible reconstructions of  $\pi^0 \rightarrow e^+ e^- \gamma$  and  $\pi^0 \rightarrow \gamma \gamma$  from the four photons and two electrons

that are found. For each possible combination, it loops over the decay volume in small steps in x, y and z, and forms a chi-squared value for each position. This value is found as:

$$\chi_{vtx}^2 = \chi_{trk}^2 + \chi_{\gamma\gamma}^2 + \chi_{ee\gamma}^2$$

where  $\chi_{trk}^2$  is a measure of how far the combined vertex position is from both electron tracks,  $\chi_{\gamma\gamma}^2$  is a measure of how far the  $\gamma\gamma$  invariant mass is from the  $\pi^0$  mass, and  $\chi_{ee\gamma}^2$  is a measure of how far the  $e^+e^-\gamma$  invariant mass is from the  $\pi^0$  mass. (These three terms are explained in more detail in the following sections.) The particle combination and decay location which give the minimum  $\chi^2$  are taken to be correct. The minimization of the multi-variable function is done using a Powell method<sup>33</sup>.

## 6.1 Track Component of Combined Vertex

This component of the combined vertex is calculated as follows:

$$\chi_{trk}^2 = \sum_{i=1}^{NTRK} \frac{(x_i - x)^2}{\sigma_{i,x}^2} + \frac{(y_i - y)^2}{\sigma_{i,y}^2}$$

where i is the index of the track,  $(x_i, y_i)$  is the projected position of the track at the z-coordinate of the vertex candidate,  $(x, y, z)$  is the vertex candidate position, and  $\sigma_i$  is the uncertainty in the track position.

The error in the track position can be due to either the uncertainty in the drift chamber hit positions or the effects of multiple scattering in the vacuum window. The error due to the track position in the drift chamber can be found according to<sup>34</sup>

$$\sigma_x = \frac{1}{S_1} + \frac{S_1}{D}(z - \frac{S_z}{S_1})$$

where

$$\begin{aligned} D &= S_1 S_2 - S_z^2 \\ S(1) &= \sum_{i=1}^{NTRK} \frac{1}{\sigma_i^2} \\ S(z) &= \sum_{i=1}^{NTRK} \frac{z_i}{\sigma_i^2} \\ S(2) &= \sum_{i=1}^{NTRK} \frac{z_i^2}{\sigma_i^2} \end{aligned}$$

where  $\sigma_x$  is the uncertainty of the track X-position at the vertex,  $z$  is the vertex z-position,  $z_i$  are the z-positions of the DC planes, and  $\sigma_i$  are the DC position resolutions. For simplicity, only the track hits in DC1 and DC2 were considered, and the DC resolution was taken to be  $\delta = 100\mu m$  for all chambers (in both the X- and Y-directions). This reduces the track position uncertainty to:

$$\sigma_{x,y} = \frac{\delta^2}{2} + \frac{2\delta^2}{(Z_{DC1} - Z_{DC2})^2} \left( z - \frac{Z_{DC1} + Z_{DC2}}{2} \right)$$

The other term in the uncertainty comes from multiple scattering in the vacuum window, which could alter the trajectory of the

track before it enters the drift chamber. The scattering angle of an electron with momentum  $p$  traveling through a material of length  $x/X_0$  (where  $X_0$  is the radiation length of the electron) is given by:

$$\theta_0 = \frac{13.6 MeV}{p} \sqrt{x/X_0} (1 + 0.038 \ln(x/X_0))$$

In the KTeV detector, most of the material is in the vacuum window, and  $x/X_0$  is measured to be  $3.56 \times 10^{-3}$ . Therefore, the track uncertainty due to scattering is given by:

$$\sigma_z = (z - Z_{vw})^2 \theta_0^2 = (z - Z_{vw})^2 \left( \frac{6.35 \times 10^{-4}}{p[GeV]} \right)^2$$

where  $Z_{vw}$  is the  $z$  position of the vacuum window, and  $\theta_0$  is assumed to be small.

## 6.2 $\gamma\gamma$ Component of Combined Vertex

The  $\gamma\gamma$  part of  $\chi_{vtx}^2$  is given by:

$$\chi_{\gamma\gamma}^2 = \frac{(M_{\pi^0} - M_{\gamma\gamma})^2}{\sigma_{\gamma\gamma}^2}$$

where  $\sigma_{\gamma\gamma}$  is the error on the  $\gamma\gamma$  invariant mass. In a two body decay, the error on the two-body invariant mass is

$$\sigma_{12}^2 = \frac{m_{12}^2}{4} \left[ \frac{\sigma_{p1}^2}{p_1^2} + \frac{\sigma_{p2}^2}{p_2^2} + \frac{\sigma_\alpha^2}{\alpha^2} \right]$$

where  $p_i$  and  $\sigma_{pi}$  are the momentum and uncertainty in the momentum of the  $i$ th particle, and  $\alpha$  is the angle between the particles. The particle momentum and uncertainty are given, for photons, by the calorimeter cluster energy and its uncertainty. The angle  $\alpha$  and its uncertainty are calculated using the positions of the photon clusters and their uncertainties.

### 6.3 $ee\gamma$ Component of Combined Vertex

Similarly, the  $ee\gamma$  portion of the vertex  $\chi^2$  is given by

$$\chi_{ee\gamma}^2 = \frac{(M_{\pi^0} - M_{ee\gamma})^2}{\sigma_{ee\gamma}^2}$$

where  $\sigma_{ee\gamma}$  is the error on the three-body invariant mass. This error can be found by first considering the uncertainty in the  $ee$  system, and then by treating the  $\gamma(ee)$  system as a two-body decay.

$$\sigma_{ee\gamma}^2 = \frac{1}{4m_{ee\gamma}^2} [(m_{ee\gamma}^2 - m_{ee}^2)^2 \left( \frac{\sigma_{ee}^2}{p_{ee}^2} + \frac{\sigma_\gamma^2}{p_\gamma^2} + \frac{\sigma_\alpha^2}{\alpha^2} \right) + m_{ee}^4 \left( \frac{\sigma_{e+}^2}{p_{e+}^2} + \frac{\sigma_{e-}^2}{p_{e-}^2} + \frac{\sigma_\beta^2}{\beta^2} \right)]$$

where  $\beta$  is the angle between the electrons and  $\alpha$  is the angle between the photon and the  $ee$  system.



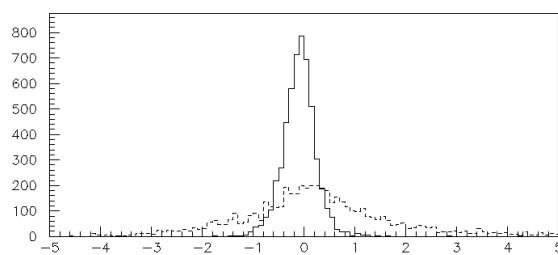


Figure 6.1: Z resolution in meters of the combined (solid line) vs. charged (dotted line) vertex routines.

## 6.4 Accuracy of the Combined Vertex

The accuracy of the combined vertexing routine can be checked using Monte Carlo events, simply by measuring the difference between the reconstructed vertex position and the generated MC value. Figure 6.1 shows this plot for both the charged and combined vertex, for a well-reconstructed sample of  $K_L \rightarrow \pi^0 \pi^0 \pi_D^0$  MC normalization mode events. As shown in the plot, the combined vertex has a sharper Z-resolution than the charged vertex.

## Chapter 7

# The Normalization Mode Analysis

### 7.1 Definition of the Normalization Mode

The normalization mode for this analysis was chosen to consist of a subset of the primary background  $K_L \rightarrow \pi^0 \pi^0 \pi_D^0$  events, specifically events where one of the photons is presumed lost down a beam hole. This allowed the same data sample—2E-NCLUS events with four neutral clusters—to be used in both the normalization and signal mode analyses.

The missing photon was located using a ktevana subroutine called T3MISP. This routine calculates the total "missing" photon energy assuming that, when combined with the found particles, it should give an exact  $K_L$  mass with zero transverse momentum squared. The missing energy is then given by a quadratic equation with two solutions—"high" and "low". A  $\pi^0$  mass is then calculated for each possible pairing of the "high" and "low" energy solutions with the

unpaired photon. The unpaired photon is the one of the four found photons that is not part of the  $\pi^0 \rightarrow \gamma\gamma$  or  $\pi^0 \rightarrow ee\gamma$  decays, as found by the combined vertex routine. The solution which gives the best  $\pi^0$  mass is taken as correct.

## 7.2 Normalization Mode Selection Cuts

### 7.2.1 Missing Photon Position Cut

The first cut made on the normalization mode is a cut on the x-y position of the photon returned by T3MISP when projected to the CsI face. The photon is required to be well within one of the two CsI beam holes.

$$8.5cm < |x_\gamma| < 21.5cm$$

$$|y_\gamma| < 6.5cm$$

Figures 7.1 and 7.2 show the data-Monte Carlo agreement for the photon x- and y- position, after all other normalization mode cuts.

### 7.2.2 Gamma-Gamma Mass Cut

The next cut is made on the mass of the  $\pi^0$  formed by combining the beamhole photon with the unpaired photon. The cut requires the mass to be within 50 MeV of the  $\pi^0$  mass. Figure 7.3 shows the data-Monte Carlo agreement for this variable for both 1997 and 1999, after all other normalization mode cuts.

### 7.2.3 Beamhole Photon Energy Cut

The energy of the chosen beamhole photon is required to be greater than 4 GeV. This rejects possible spurious low-energy solutions. Figure 7.4 shows the data-Monte Carlo agreement for this variable for both 1997 and 1999, after all other normalization mode cuts.

### 7.2.4 PP0KINE Cut

PP0KINE is a kinematic variable designed to indicate the presence of an additional pion in an event where two pions are already reconstructed. It is defined as the longitudinal momentum squared of the unreconstructed  $\pi^0$ , calculated in the frame in which the momentum of the other  $\pi^0 \pi^0$  pair is transverse. ("Longitudinal" momentum refers to momentum along the beam direction.) PP0KINE is calculated as:

$$\text{PP0KINE} = \frac{(M_K^2 - M_{\pi^0}^2 - m_{\pi\pi}^2)^2 - 4M_{\pi^0}^2 m_{\pi\pi}^2 - 4M_K^2 p_{t\pi\pi}^2}{p_{t\pi\pi}^2 - m_{\pi\pi}^2}$$

where  $M_K$  and  $M_{\pi^0}$  are the masses of the  $K_L$  and  $\pi^0$ , respectively, and  $m_{\pi\pi}$  refers to the reconstructed mass of the two pions in the laboratory frame.  $p_{t\pi\pi}^2$  is the total transverse momentum of the two reconstructed pions with respect to the target, again in the lab frame. (In this case  $m_{\pi\pi}$  and  $p_{t\pi\pi}^2$  refer to the two pions reconstructed by the combined vertexing routine; the unpaired photon is ignored in

this calculation.) PP0KINE should be positive for  $K_L \rightarrow \pi^0 \pi^0 \pi_D^0$  events, with a small negative tail due to resolution. All events with PP0KINE  $< 0.0$  are rejected from the normalization sample. Figure 5 shows the data-Monte Carlo agreement for this variable for both 1997 and 1999, after all other normalization mode cuts. The negative peak is due to events where the photons from  $\pi^0 \rightarrow e^+ e^- \gamma$  and  $\pi^0 \rightarrow \gamma \gamma$  are incorrectly paired by the combined vertex routine, resulting in a badly calculated mass and transverse momentum for the two pions.

#### 7.2.5 Vertex $\chi^2$ Cut

The vertex  $\chi^2$  returned from the combined vertex routine is required to be less than 5.0 for 1997, and less than 4.0 for 1999. The tighter 1999 cut is done due to the increased backgrounds in 1999 from having a lower magnet momentum kick. Figure 7.6 shows this variable after all other normalization mode cuts for 1997 and 1999.

#### 7.2.6 Vertex Z-position Cut

The vertex z-position is required to be between 95m and 150m. The plots for 1997 and 1999 are shown in figure 7.7 after all other normalization mode cuts. As shown in the plots the cut at 150m rejects a region of data/Monte Carlo disagreement due to poor simulation of conversions in the vacuum window (at Z=158).

### 7.2.7 $m_{ee\gamma}$ Cut

For the 1997 analysis, the mass of the  $ee\gamma$  pairing chosen by the combined vertex routine was required to be within 3 MeV of the actual  $\pi^0$  mass; this was tightened to 2 MeV for 1999 to eliminate mispairings. Figure 7.8 shows the distributions for the two years after all other normalization mode cuts. This cut has a small effect, since  $m_{ee\gamma}$  was already constrained to be close to the  $\pi^0$  mass by the combined vertexing routine .

### 7.2.8 $m_{\gamma\gamma}$ Cut

The mass of the  $\gamma\gamma$  pairing was required to be within 2 MeV of the actual  $\pi^0$  mass for 1997, and 1 MeV for 1999. The distribution of this variable for 1997 and 1999 is shown in figure 7.9 after all other normalization mode cuts. Again, this cut has a small effect due to the fact that the variable has been constrained by the combined vertexing routine.

### 7.2.9 Vertex x- and y- position cut

A cut is done on the x- and y- position of the decay vertex, as projected to the CsI face. It is required to be well within the beam region:

$$8.5cm < |x| < 21.5cm$$

$$|y| < 6.5cm$$

Figures 7.10 and 7.11 plot the x- and y- projections of the decay vertex, for 1997 and 1999 data after all other normalization mode cuts.

### 7.2.10 Fusion $\chi^2$ Cut

Fusion  $\chi^2$  is a variable which measures the likelihood that any given photon cluster is actually a "fusion" of two different clusters. It does this based on the shape of the cluster's EM shower. The energy in each block of the cluster is compared to the expected energy from GEANT shower shapes, to get a  $\chi^2$  value for each block. The fusion  $\chi^2$  variable in this analysis is the sum of these values over a  $3 \times 3$  grid of blocks centered on the seed block. It is required to be less than 7.0 for all six clusters.

Figure 7.12 shows fusion  $\chi^2$  after all other normalization mode cuts for 1997 and 1999. There is a significant difference between data and Monte Carlo for this variable, probably due to inaccuracies in the GEANT modeling of EM showers in the calorimeter. However, the cut is wide enough that this has a small effect on the total acceptance. For 1997, the acceptance for data is 97.2%, while that for  $K_L \rightarrow \pi^0 \pi^0 \pi_D^0$  MC is 95.8%; for 1999, the acceptance is 97.4% for data and 96.0% for  $3\pi_D^0$  MC.



### 7.2.11 Next-best Vertex $\chi^2$ Cut

Events with a next-best combined vertex  $\chi^2$  within 25.0 of the chosen value were cut, to eliminate events with an ambiguous vertex. Figure 7.13 shows plots of the next-best vertex  $\chi^2$  minus the best vertex  $\chi^2$ , after all other normalization mode cuts.

### 7.2.12 $\gamma\gamma$ Mispairing Cut

Events were cut if any pair of photons (other than the correct pairing) gave a mass in the range 0.130-0.155 GeV. This was done to eliminate events where the photons were mispaired. The minimum  $\gamma\gamma$  mass for any pairing other than the correct one is plotted (after all other normalization mode cuts) in figure 7.14.

### 7.2.13 Overlapping Clusters Cut

Like the fusion  $\chi^2$  cut, this cut was done to eliminate events where one of the found clusters is actually an overlap of two nearby photon hits. If a fraction of the energy of one cluster ( $E_{overlap}$ ) is assumed to come from another overlapping photon, an "overlap  $\chi^2$ " can be formed for the seven-body final state using the combined vertexing routine. An overlapping cluster routine formed this overlap  $\chi^2$ , stepping through each of the four clusters; for each cluster, several values of  $E_{overlap}$ , from 5% to 50% of the total cluster energy, were considered. The minimum  $\chi^2$  for all possible clusters and values of  $E_{overlap}$  was chosen.

The minimum overlapping cluster  $\chi^2$  was required to be less than 25.0 for the 1997 analysis, and 50.0 for the 1999 analysis. This variable is plotted for both data and  $K_L \rightarrow \pi^0\pi^0\pi_D^0$  MC after all of the above cuts, for 1997 and 1999, in figure 7.15.

Figure 7.16 shows on a logarithmic scale the reconstructed  $\pi^0$  mass from the combination of the T3MISP photon with the unpaired photon, after all normalization mode cuts. This plot demonstrates that there is no significant background to the  $K_L \rightarrow \pi^0\pi^0\pi_D^0$  normalization mode. This was confirmed by generating several other possible backgrounds and checking their effect on the normalization mode; the results of this procedure are described in chapter 9.

### 7.3 $K_L$ Flux Calculation

One purpose of the normalization mode is to provide an estimate of the total  $K_L$  flux used in the single event sensitivity, using the following formula:

$$N_n^d = N_K \times BR(K_L \rightarrow \pi^0\pi^0\pi_D^0) \times A_n$$

where  $N_n^d$  is the number of normalization mode events in data,  $N_K$  is the kaon flux,  $BR(K_L \rightarrow \pi^0\pi^0\pi_D^0)$  is the  $3\pi^0$  Dalitz branching ratio, and  $A_n$  is the normalization mode acceptance, as calculated from the Monte Carlo. Applying this formula gives a 1997 flux value of  $2.43 \times 10^{11} K_L$ . The 1999  $K_L$  flux is then  $3.66 \times 10^{11}$ .

## 7.4 The Final Normalization Sample

Tables 7.1 and 7.2 show the number of events at each stage of the normalization mode analysis, for both data and  $K_L \rightarrow \pi^0 \pi^0 \pi_D^0$  Monte Carlo, for the 1997 and 1999 analyses respectively. For 1997 the final number of events was 7725 for data, 36446 for  $K_L \rightarrow \pi^0 \pi^0 \pi_D^0$  MC. For 1999 the numbers were 9024 for data and 34002 for  $K_L \rightarrow \pi^0 \pi^0 \pi_D^0$  MC.

Cut	Data Events	$K_L \rightarrow \pi^0 \pi^0 \pi_D^0$ Events	MC/Data Ratio
Start (T3MISP returns non-zero energy)	402476	1851443	4.60
T3MISP Photon Position	86508	402451	4.65
$m_{\pi^0}$ (Beamhole + Unpaired Photon)	63912	305018	4.77
Beamhole $E_\gamma$	62917	299830	4.77
PP0KINE	39749	195904	4.92
Vertex $\chi^2$	27136	137489	5.02
Vertex Z	21590	104999	4.86
$m_{ee\gamma}$	21443	104227	4.86
$m_{\gamma\gamma}$	21328	103820	4.87
Vertex x-y position	21093	102305	4.85
Fusion $\chi^2$	20510	97979	4.78
Next best $\chi^2$	14805	70857	4.79
$\gamma\gamma$ Mispairing Cut	11587	55088	4.75
Overlap $\chi^2$ Cut	7725	36446	4.72

Table 7.1: Number of events past each normalization mode cut, for data and  $K_L \rightarrow \pi^0 \pi^0 \pi_D^0$  MC, for 1997.

Cut	Data Events	$K_L \rightarrow \pi^0 \pi^0 \pi_D^0$ Events	MC/Data Ratio
Start (T3MISP returns non-zero energy)	924233	3492693	3.78
T3MISP Photon Position	171172	689436	4.02
$m_{\pi^0}$ (Beamhole + Unpaired Photon)	128963	520578	4.03
Beamhole $E_\gamma$	126068	508917	4.04
PP0KINE	81225	330256	4.07
Vertex $\chi^2$	52447	204282	3.90
Vertex Z	40113	151235	3.77
$m_{ee\gamma}$	38352	144305	3.76
$m_{\gamma\gamma}$	34440	130290	3.78
Vertex x-y position	33103	124436	3.76
Fusion $\chi^2$	32249	119564	3.71
Next best $\chi^2$	22760	85084	3.74
$\gamma\gamma$ Mispairing Cut	17482	65774	3.76
Overlap $\chi^2$ Cut	9024	34002	3.77

Table 7.2: Number of events past each normalization mode cut, for data and  $K_L \rightarrow \pi^0 \pi^0 \pi_D^0$  MC, for 1999.

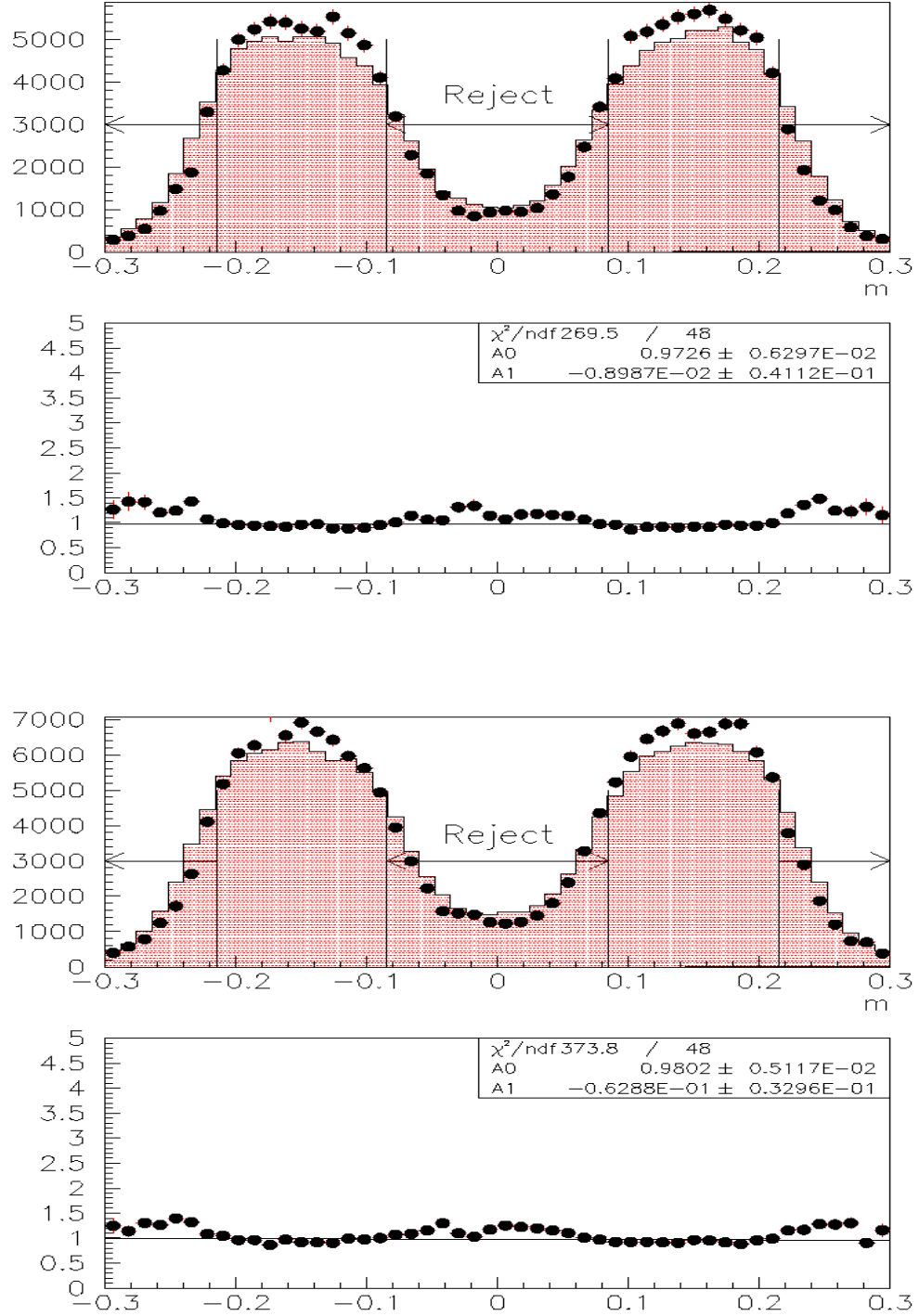


Figure 7.1: Reconstructed x-position of the T3MISP photon at the CsI face for 1997 (top) and 1999 (bottom) running, after all normalization mode cuts except the cut on this variable. Dots are data, colored histograms are  $K_L \rightarrow \pi^0 \pi^0 \pi_D^0$  MC. The data/MC ratios for each year are shown below the comparison plots.

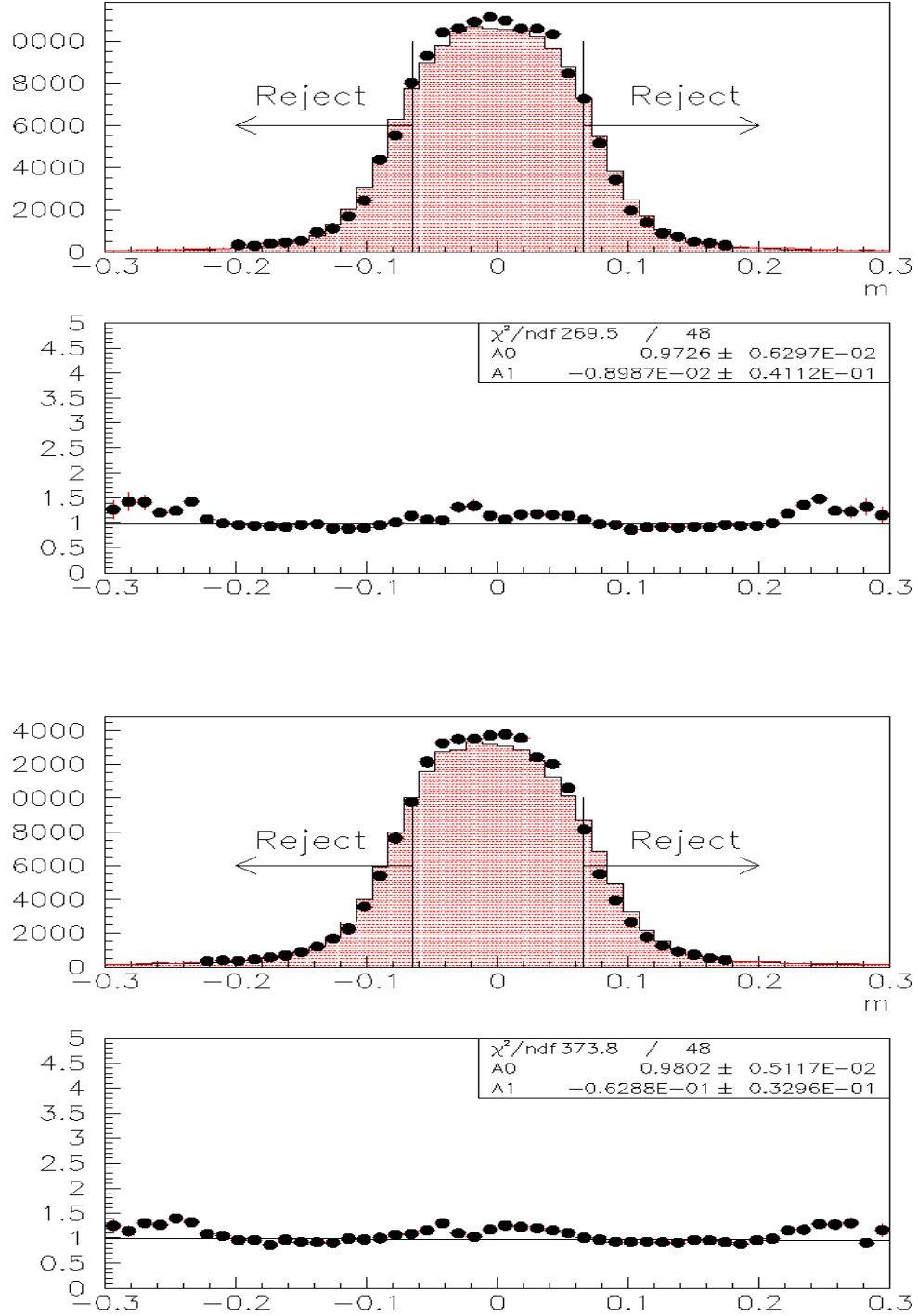


Figure 7.2: Reconstructed y-position of the T3MISP photon at the CsI face for 1997 (top) and 1999 (bottom) running, after all normalization mode cuts except the cut on this variable. Dots are data, colored histograms are  $K_L \rightarrow \pi^0 \pi^0 \pi_D^0$  MC. The data/MC ratios for each year are shown below the comparison plots.

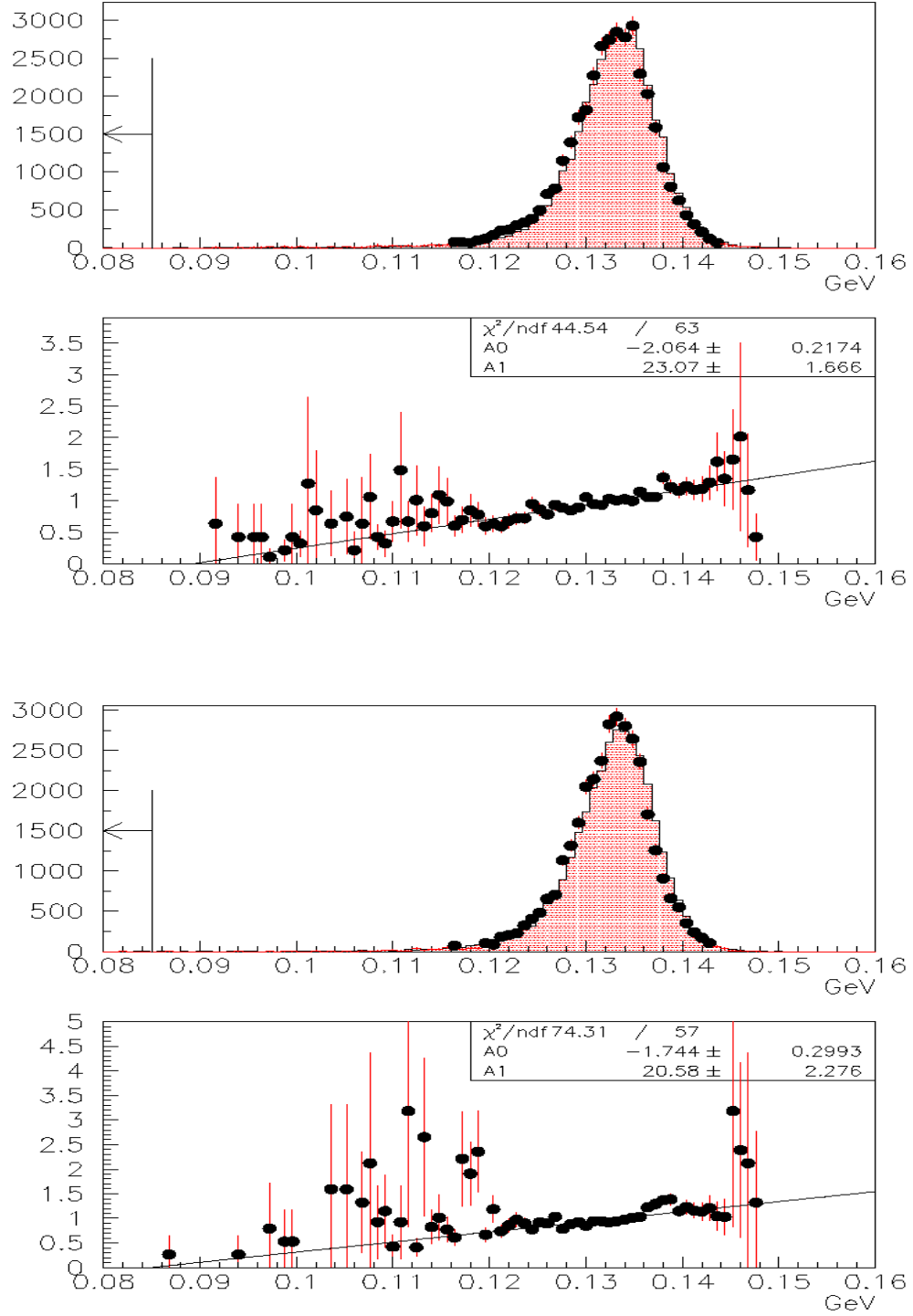


Figure 7.3: Combined mass of the T3MISP photon and the direct emission photon for 1997 (top) and 1999 (bottom) running, after all normalization mode cuts except the cut on this variable. Dots are data, colored histograms are  $K_L \rightarrow \pi^0 \pi^0 \pi_D^0$  MC. The data/MC ratios for each year are shown below the comparison plots.

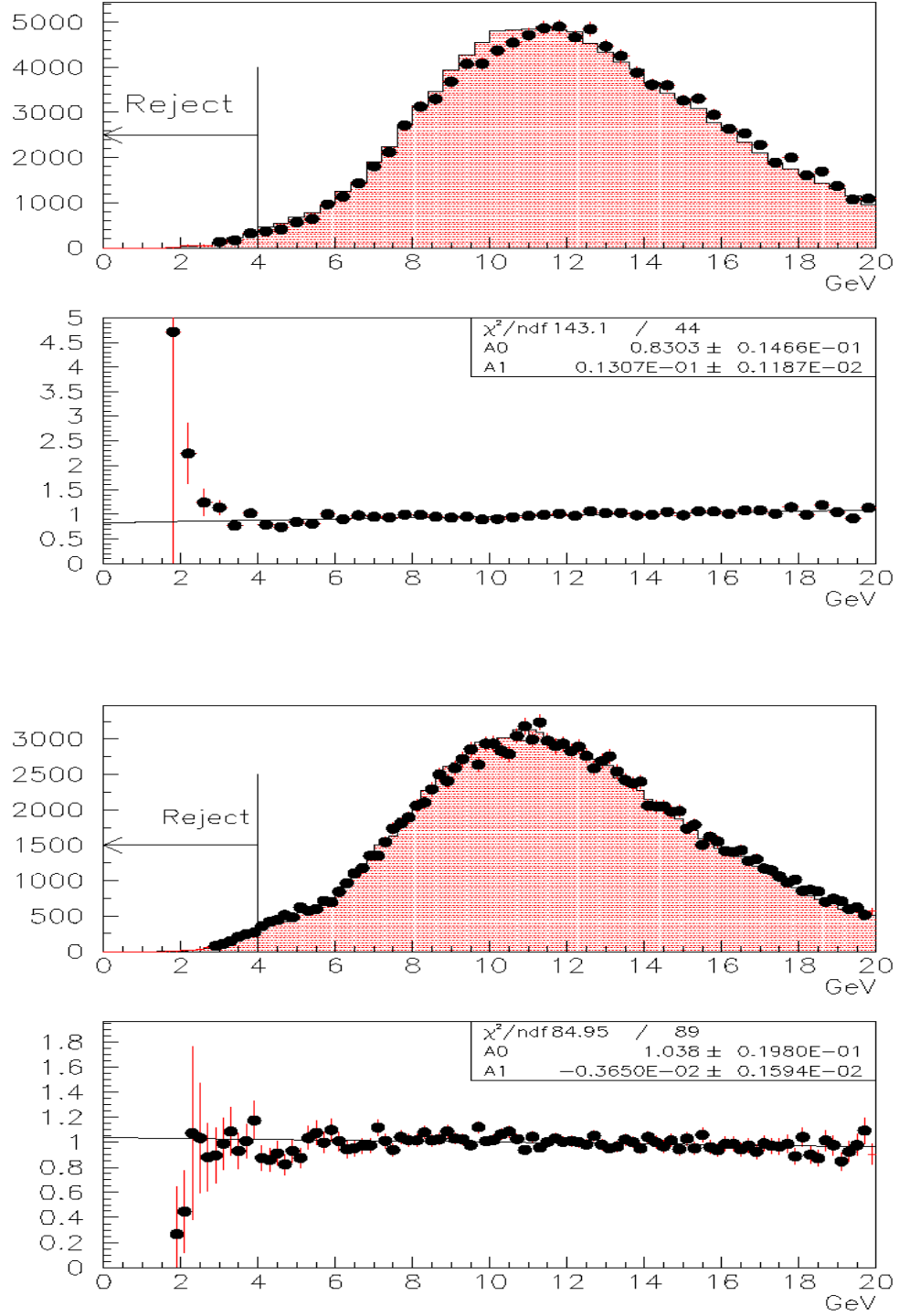


Figure 7.4: Energy of the T3MISP (beamhole) photon for 1997 (top) and 1999 (bottom) running, after all normalization mode cuts except the cut on this variable. Dots are data, colored histograms are  $K_L \rightarrow \pi^0 \pi^0 \pi_D^0$  MC. The data/MC ratios for each year are shown below the comparison plots.



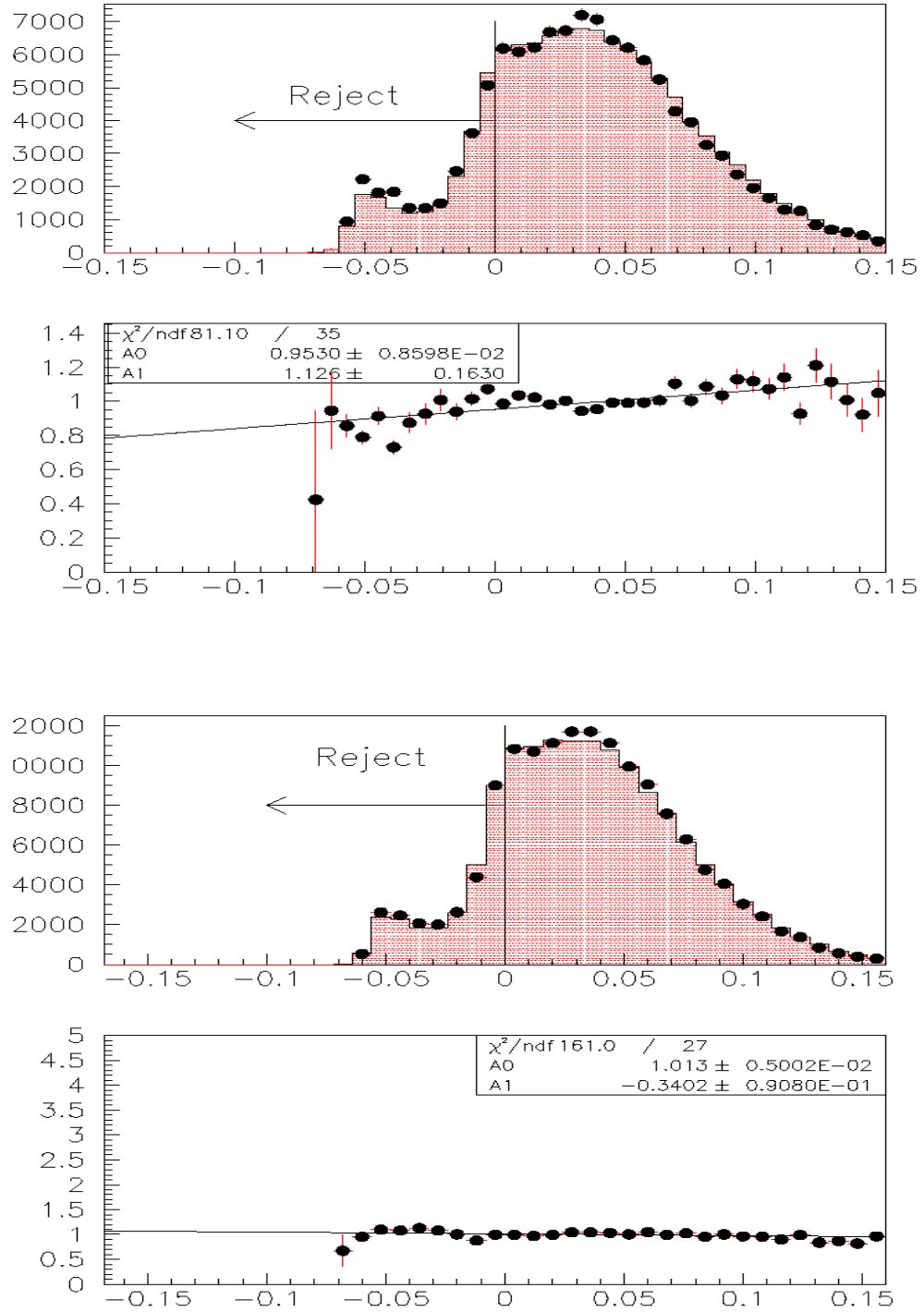


Figure 7.5: PP0KINE for 1997 (top) and 1999 (bottom) running, after all normalization mode cuts except the cut on this variable. Dots are data, colored histograms are  $K_L \rightarrow \pi^0 \pi^0 \pi_D^0$  MC. The data/MC ratios for each year are shown below the comparison plots.

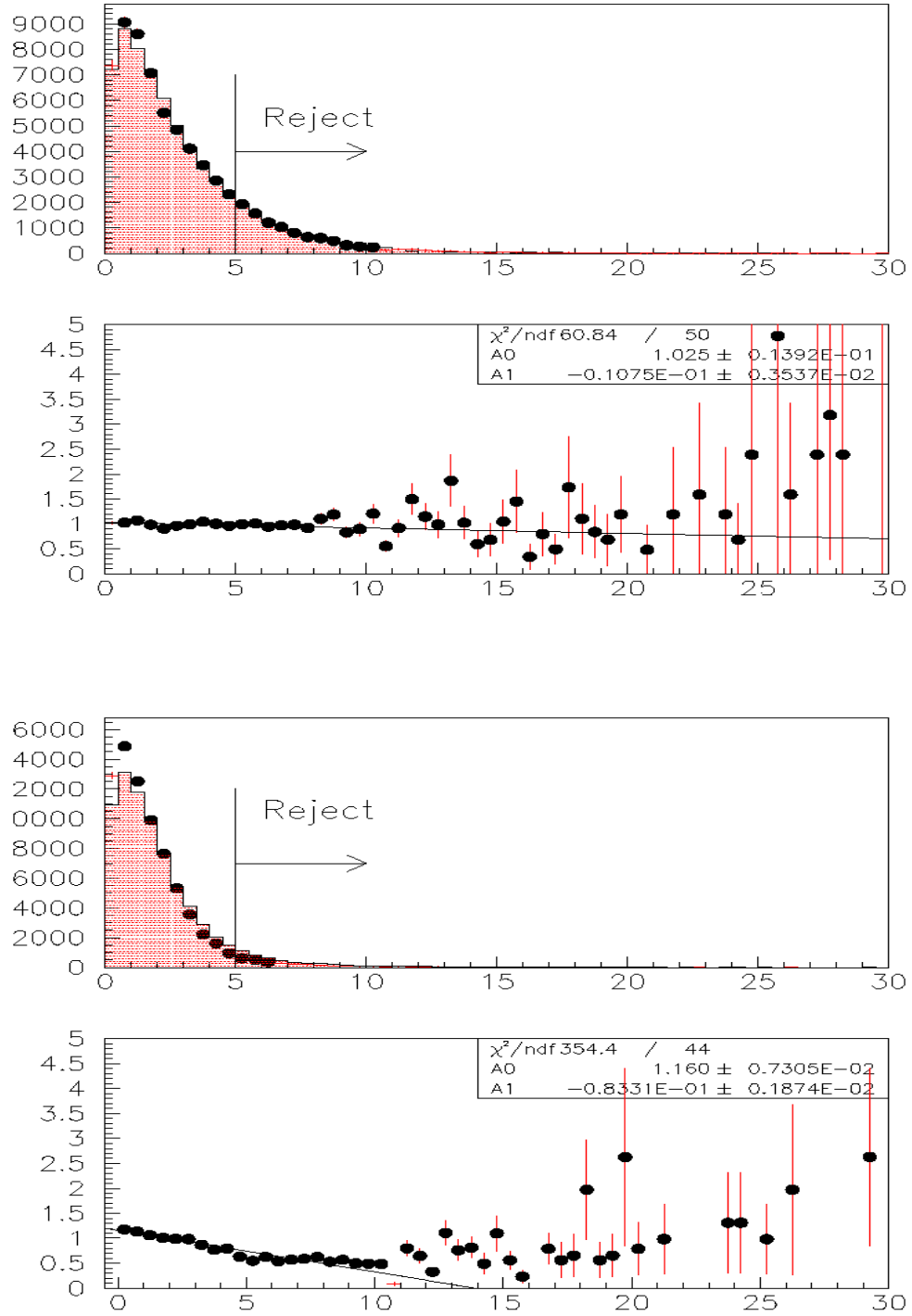


Figure 7.6: Combined Vertex  $\chi^2$  for 1997 (top) and 1999 (bottom) running, after all normalization mode cuts except the cut on this variable. Dots are data, colored histograms are  $K_L \rightarrow \pi^0 \pi^0 \pi_D^0$  MC. The data/MC ratios for each year are shown below the comparison plots.

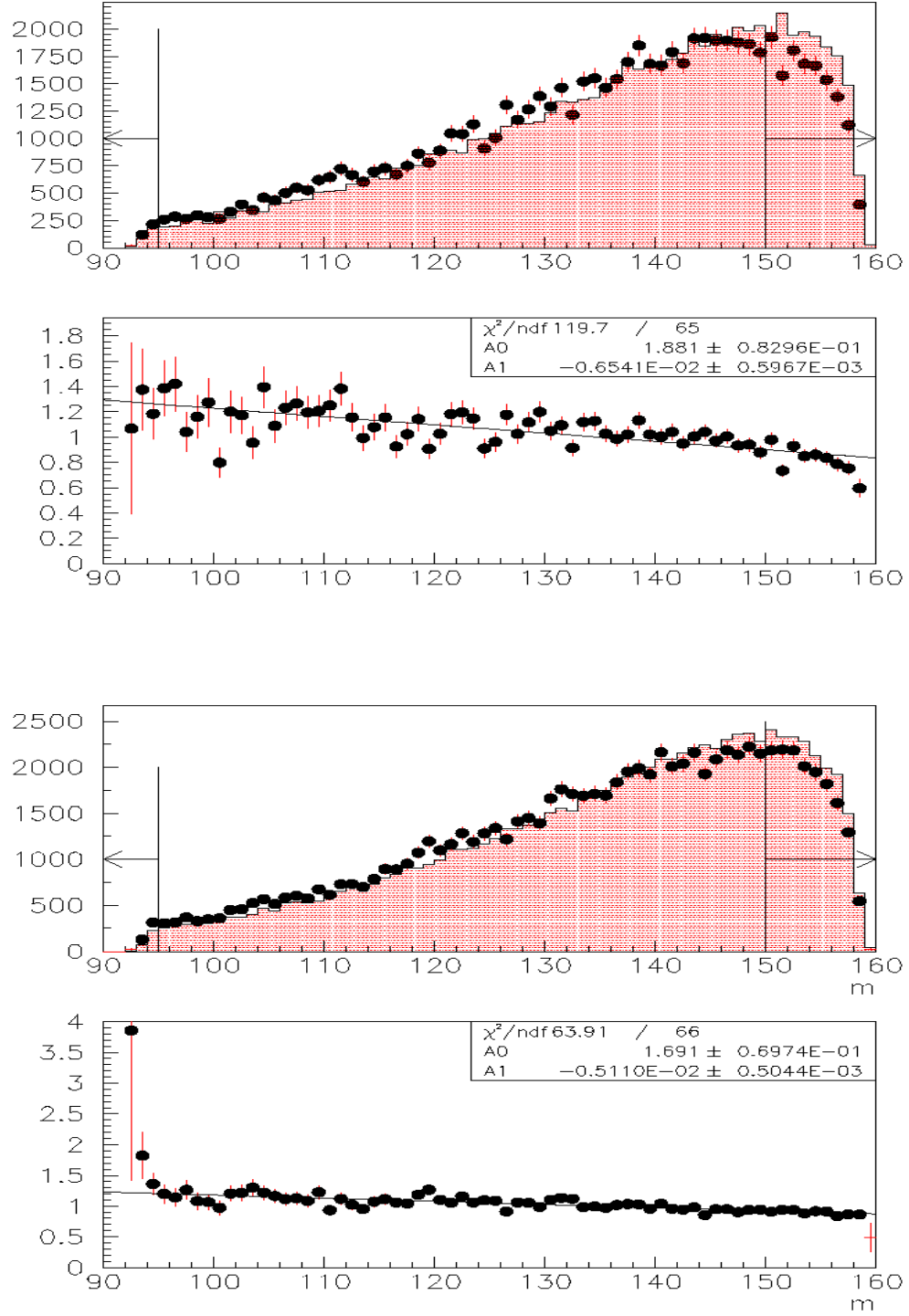


Figure 7.7: Vertex z-position for 1997 (top) and 1999 (bottom) running, after all normalization mode cuts except the cut on this variable. Dots are data, colored histograms are  $K_L \rightarrow \pi^0 \pi^0 \pi_D^0$  MC. The data/MC ratios for each year are shown below the comparison plots.

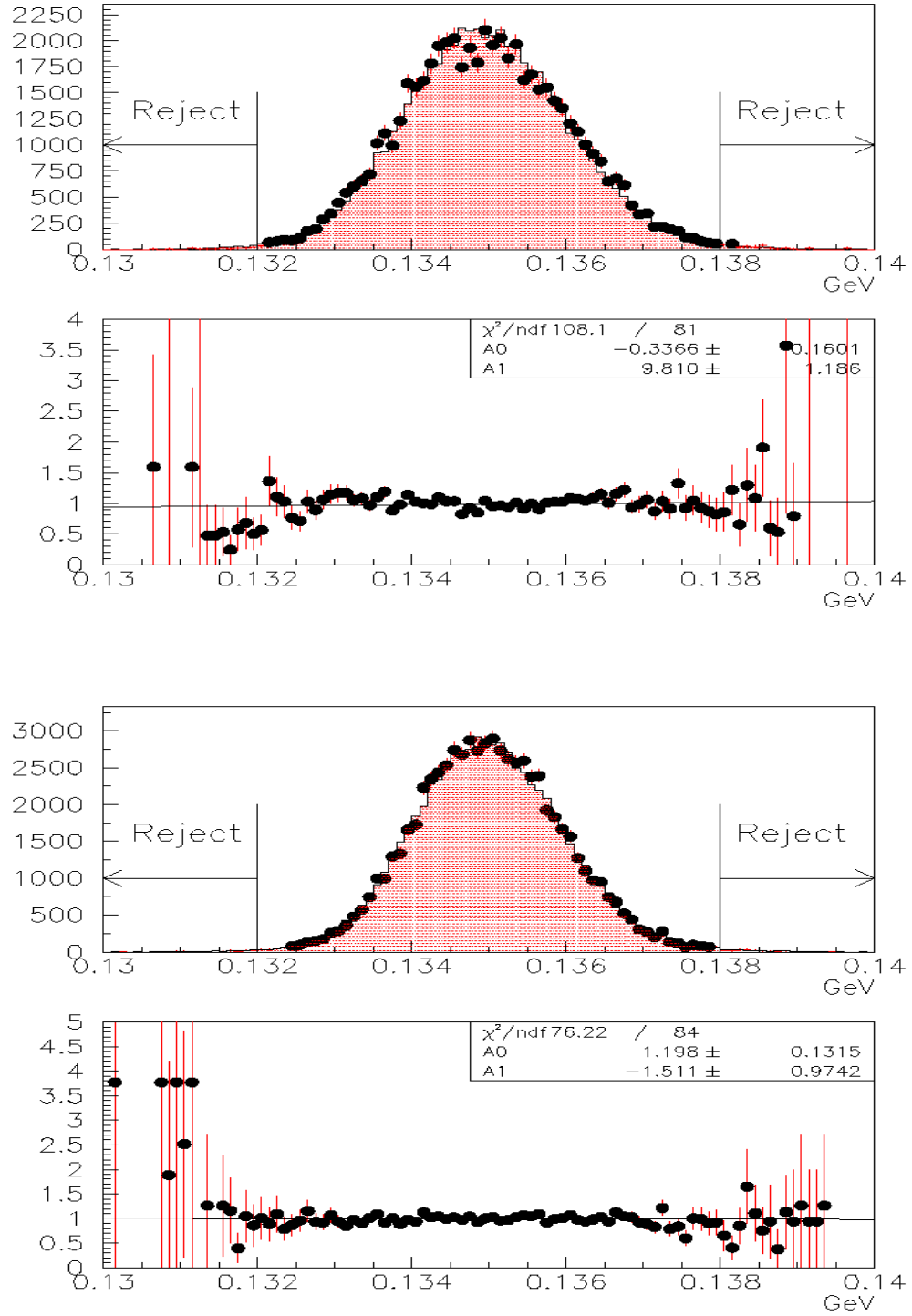


Figure 7.8:  $m_{ee\gamma}$  for 1997 (top) and 1999 (bottom) running, after all normalization mode cuts except the cut on this variable. Dots are data, colored histograms are  $K_L \rightarrow \pi^0 \pi^0 \pi_D^0$  MC. The data/MC ratios for each year are shown below the comparison plots.

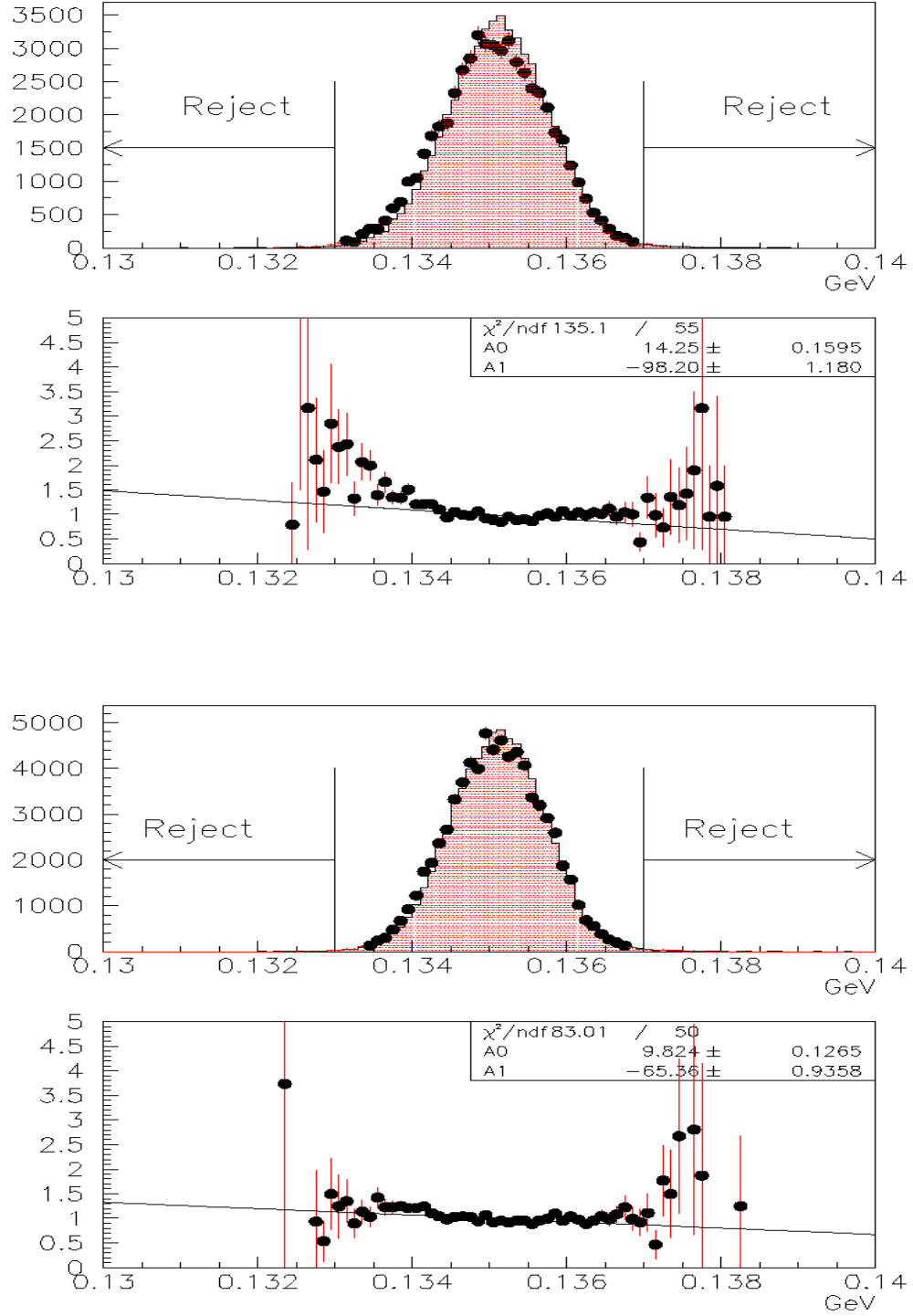


Figure 7.9:  $m_{\gamma\gamma}$  for 1997 (top) and 1999 (bottom) running, after all normalization mode cuts except the cut on this variable. Dots are data, colored histogram is  $K_L \rightarrow \pi^0 \pi^0 \pi_D^0$  MC. The data/MC ratios are shown below the comparison plots.

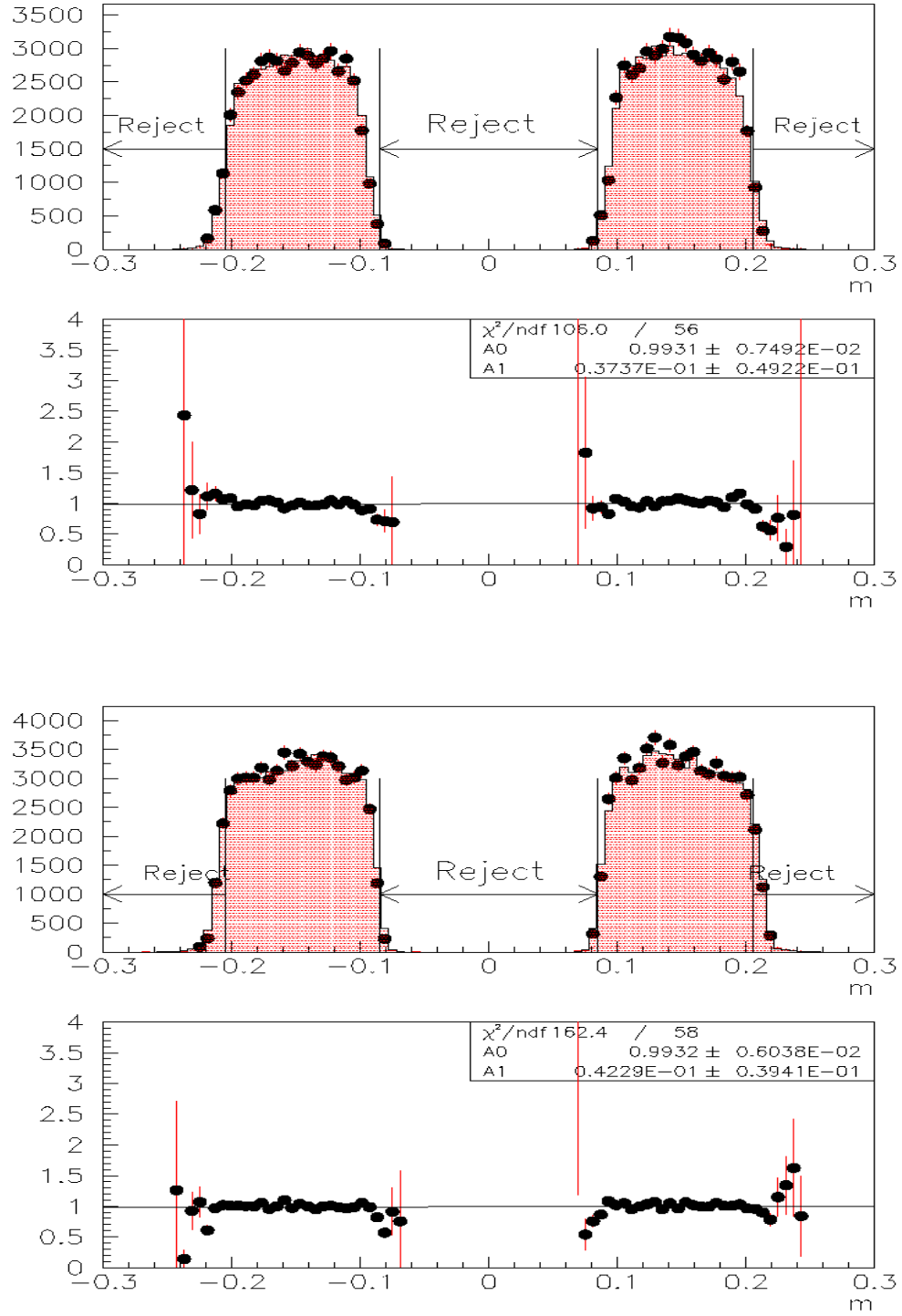


Figure 7.10: Vertex x-projection at the CsI face for 1997 (top) and 1999 (bottom) running, after all normalization mode cuts except the cut on this variable. Dots are data, colored histogram is  $K_L \rightarrow \pi^0 \pi^0 \pi_D^0$  MC. The data/MC ratios are shown below the comparison plots.

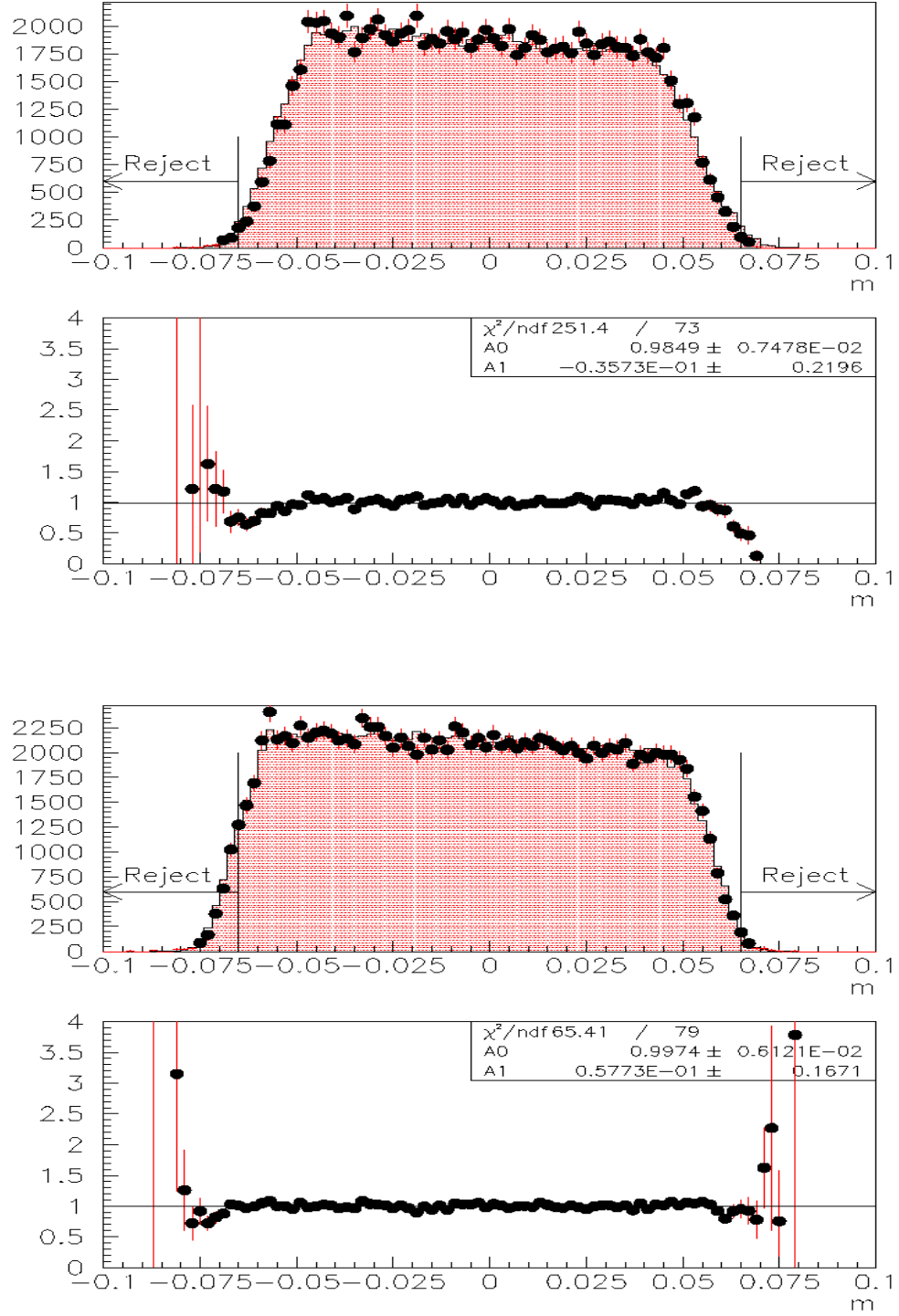


Figure 7.11: Vertex y-projection at the CsI face for 1997 (top) and 1999 (bottom) running, after all normalization mode cuts except the cut on this variable. Dots are data, colored histogram is  $K_L \rightarrow \pi^0 \pi^0 \pi_D^0$  MC. The data/MC ratios are shown below the comparison plots.

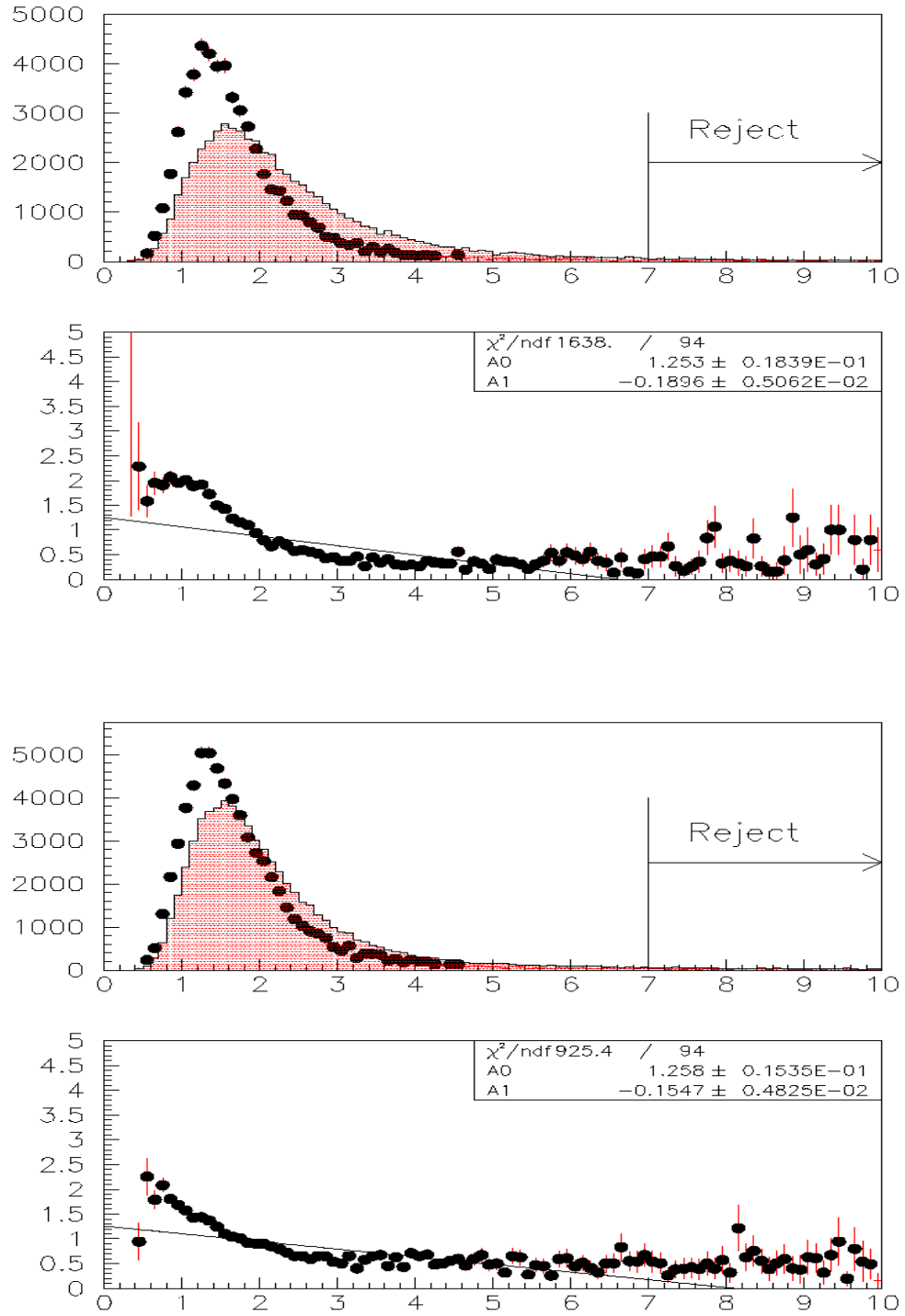


Figure 7.12: Fusion  $\chi^2$  for 1997 (top) and 1999 (bottom) running, after all normalization mode cuts except the cut on this variable. Dots are data, colored histograms are  $K_L \rightarrow \pi^0 \pi^0 \pi_D^0$  MC. The data/MC ratios for each year are shown below the comparison plots.



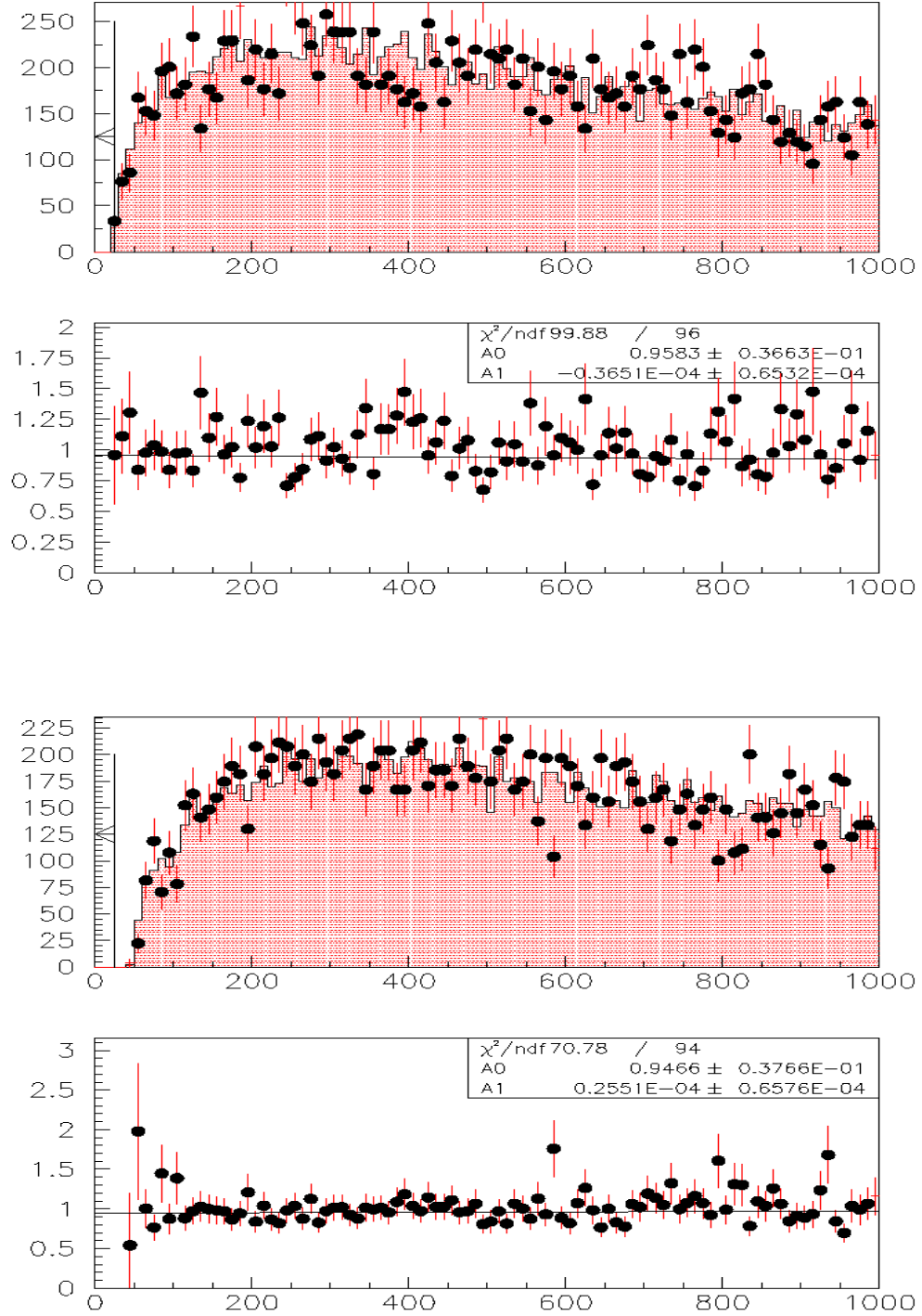


Figure 7.13: Difference between the next best and best vertex  $\chi^2$  for 1997 (top) and 1999 (bottom) running, after all normalization mode cuts except the cut on this variable. Dots are data, colored histograms are  $K_L \rightarrow \pi^0 \pi^0 \pi_D^0$  MC. The data/MC ratios for each year are shown below the comparison plots.

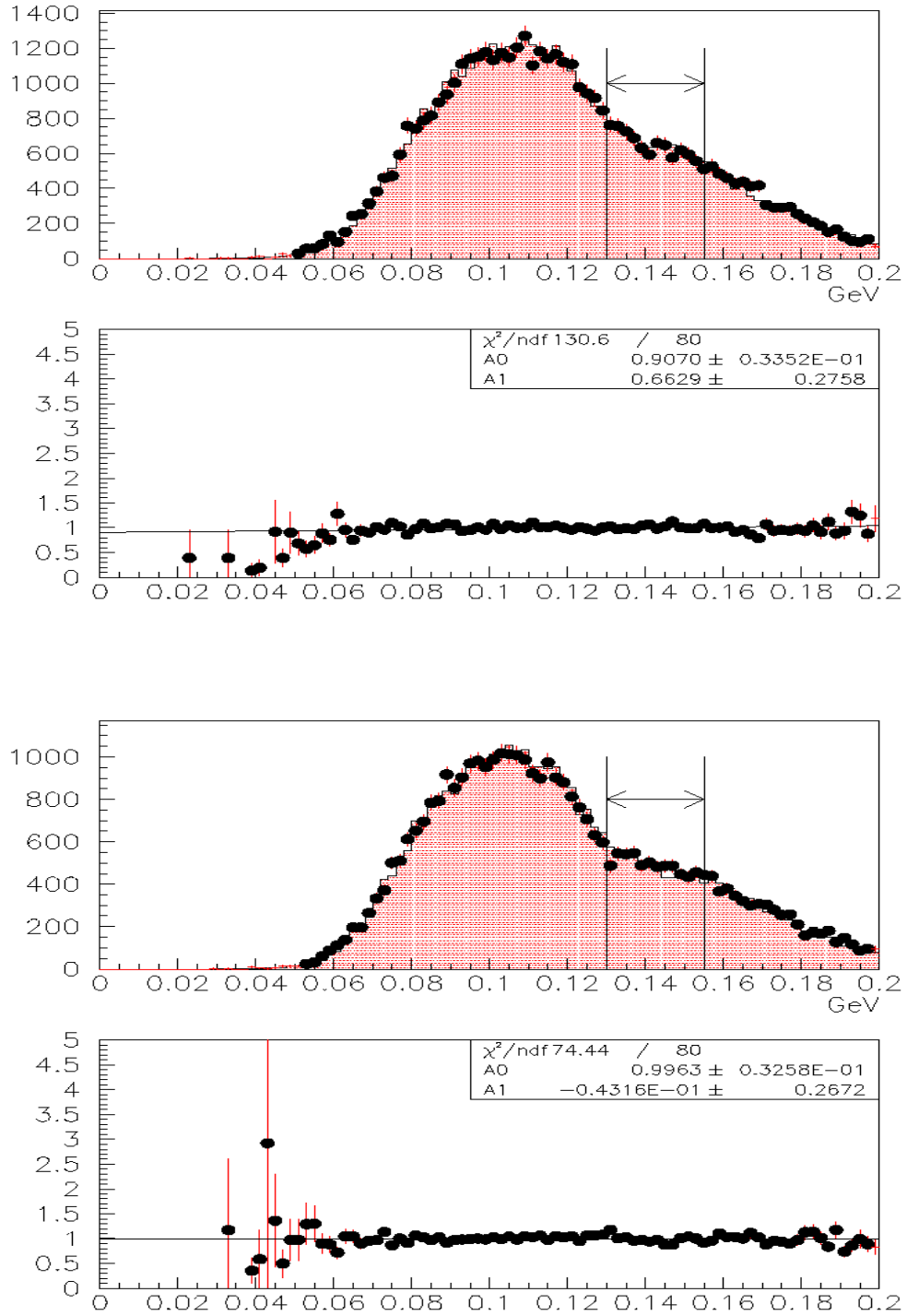


Figure 7.14: Minimum mass of any  $\gamma\gamma$  pair other than the correct one for 1997 (top) and 1999 (bottom) running, after all normalization mode cuts except the cut on this variable. Dots are data, colored histograms are  $K_L \rightarrow \pi^0\pi^0\pi_D^0$  MC. The data/MC ratios for each year are shown below the comparison plots.

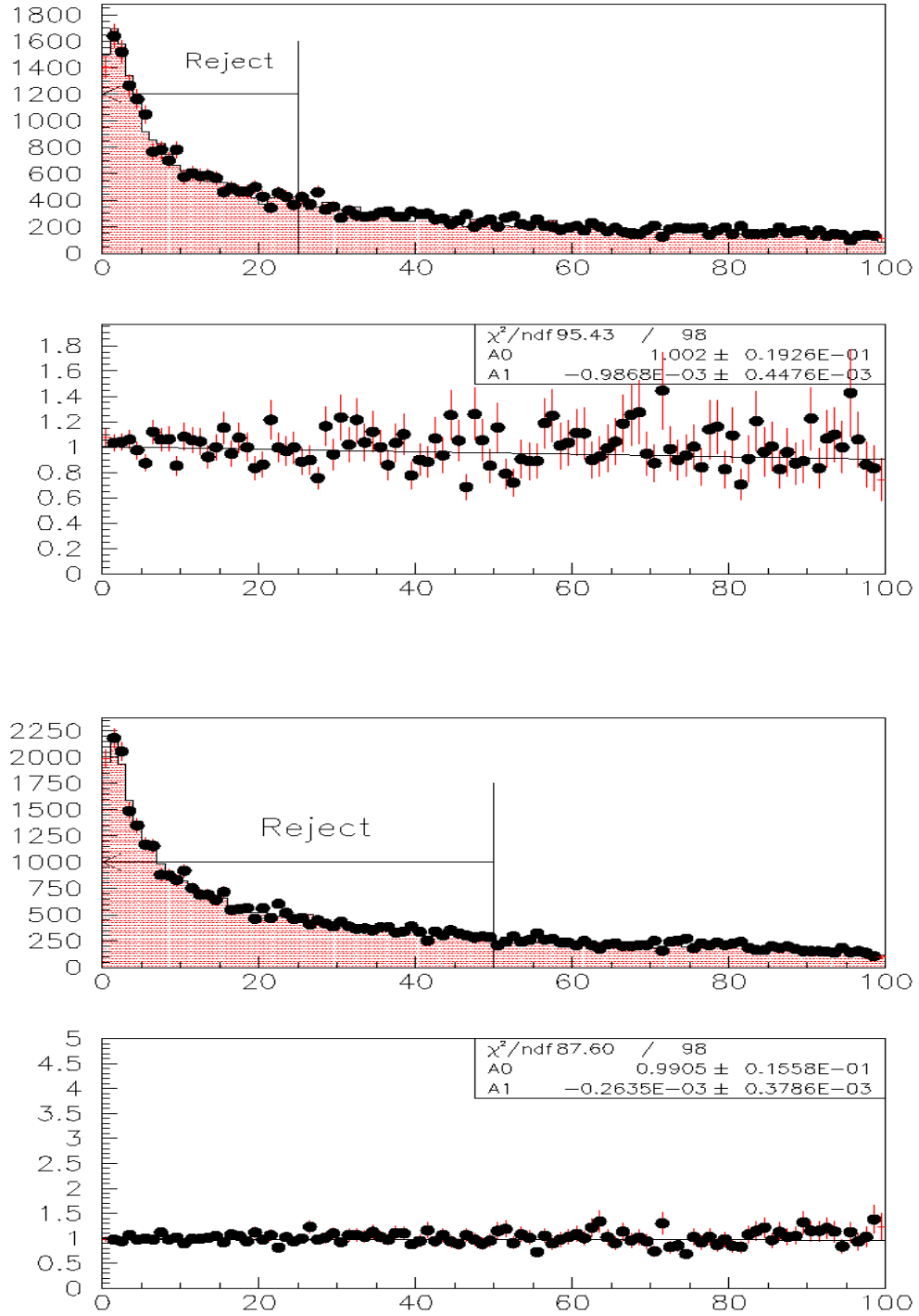


Figure 7.15: Overlapping cluster  $\chi^2$  for 1997 (top) and 1999 (bottom) running, after all normalization mode cuts except the cut on this variable. Dots are data, colored histograms are  $K_L \rightarrow \pi^0 \pi^0 \pi_D^0$  MC. The data/MC ratios for each year are shown below the comparison plots.

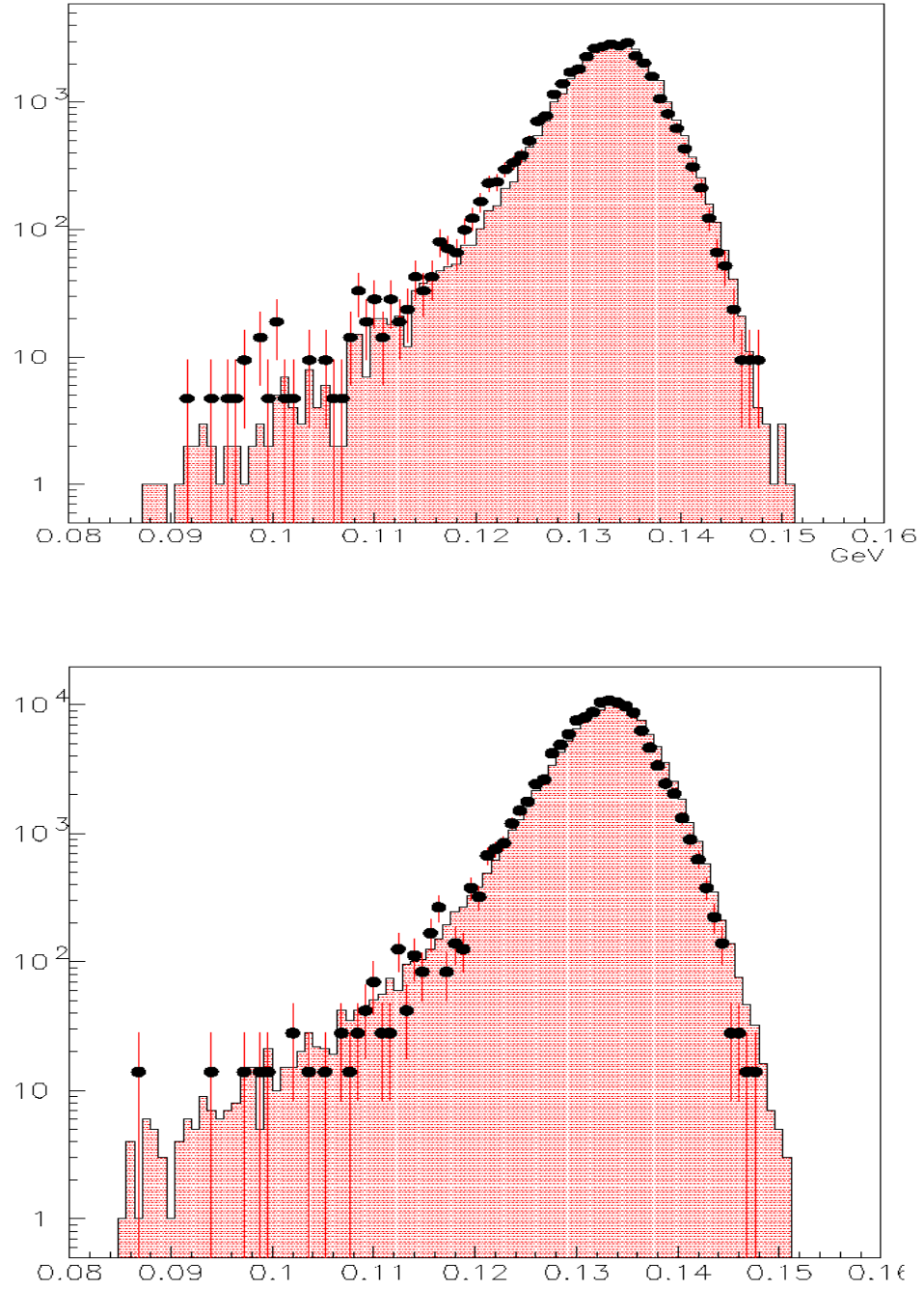


Figure 7.16: Combined mass of the T3MISP photon and the direct emission photon for 1997 (top) and 1999 (bottom) running, after all normalization mode cuts on a logarithmic scale. Dots are data, colored histograms are  $K_L \rightarrow \pi^0 \pi^0 \pi_D^0$  MC. The data/MC ratios for each year are shown below the comparison plots.

## Chapter 8

# The Signal Mode Analysis

### 8.1 Defining the Signal Region

After the crunch, events were selected starting with two variables:  $m_{ee\gamma\gamma\gamma\gamma}$ , the combined invariant mass of the six found particles, and  $p_t^2$ , the total transverse momentum relative to the beam direction of these six particles. Signal mode events were expected to have a total mass close to the nominal  $K_L$  mass and a  $p_t^2$  close to zero. To select events on this basis, a "signal region" was defined as a two-dimensional region of a  $m_{ee\gamma\gamma\gamma\gamma}$  vs  $p_t^2$  plot. Different shapes for the signal region were used in the 1997 and 1999 analyses.

In the 1997 analysis, the signal region was a rectangular "box" defined as:

$$\begin{aligned} |m_{ee\gamma\gamma\gamma\gamma} - m_K| &\leq 0.003 \text{ GeV} \\ p_t^2 &\leq 0.00015 \text{ GeV}^2 \end{aligned}$$

Using this definition, 80% of  $K_L \rightarrow \pi^0 \pi_D^0 \gamma$  MC events which pass

the crunch and bad run/spill cuts are in the signal region. Figure 8.1 shows the  $m_{ee\gamma\gamma\gamma}$  vs  $p_t^2$  plot, with the signal box (red), for signal mode MC events.

For the 1999 analysis, the signal region was defined using a more complicated procedure. First, normalized histograms of the total event mass and  $p_t^2$  were produced for all signal MC events past the crunch; these plots are shown in figure 8.2. Then, each event was assigned a "signal probability"  $P(m_{ee\gamma\gamma\gamma}, p_t^2)$ , defined as

$$P(m_{ee\gamma\gamma\gamma}, p_t^2) = P(m_{ee\gamma\gamma\gamma}) P(p_t^2)$$

where  $P(m_{ee\gamma\gamma\gamma})$  was the value of the normalized signal mode histogram in the bin containing that event's value of  $m_{ee\gamma\gamma\gamma}$  (and similarly for  $p_t^2$ ). Finally, the event was accepted into the signal mode if the logarithm of the signal probability was less than -6.6; this cut was chosen to accept 68% of signal mode MC events past the crunch. Figure 8.3 shows a plot of the logarithm of the signal probability for all 1999 signal mode events (shaded) and background mode events (dots). Figure 8.4 shows a plot of the total mass vs.  $p_t^2$  for all 1999 signal mode MC events past the crunch; the signal region is outlined on the plot.

## 8.2 Blind Analysis Method

At this stage of the analysis there were still a large number of  $K_L \rightarrow \pi^0 \pi^0 \pi_D^0$  background Monte Carlo events in the signal region. Looking at the signal region for data would therefore show many events, nearly all if not all of which would be background, and it would be impossible to determine whether any signal  $K_L \rightarrow \pi^0 \pi_D^0 \gamma$  events were present. Therefore, it was necessary to introduce other cuts to eliminate background events while preserving as many signal mode events as possible in the signal region.

To avoid bias, cut selection must be done using only Monte Carlo events. To ensure objectivity, the signal region was made "blind", which means that events in the signal region for data were not counted or looked at. After selecting a series of cuts that eliminate background MC events in the signal region, the signal region was opened for data.

## 8.3 Justification of $K_L \rightarrow \pi^0 \pi^0 \pi_D^0$ As Primary Background

This analysis assumed that  $K_L \rightarrow \pi^0 \pi^0 \pi_D^0$  was the primary background to the signal  $K_L \rightarrow \pi^0 \pi_D^0 \gamma$  mode, due to the large branching ratio for  $K_L \rightarrow \pi^0 \pi^0 \pi_D^0$  compared to any other topologically similar modes. This assumption was checked by comparing plots of variables for the data with those for the  $K_L \rightarrow \pi^0 \pi^0 \pi_D^0$  Monte Carlo

after all cuts. Figures 8.5-8.8 show plots of  $m_{ee\gamma\gamma\gamma}$ ,  $p_t^2$ ,  $Vertex\chi^2$ , and vertex z-position for data and  $K_L \rightarrow \pi^0\pi^0\pi_D^0$  MC events outside the signal box, after the set of cuts listed below. The good agreement in these plots demonstrates that the data at this stage consisted almost entirely of  $K_L \rightarrow \pi^0\pi^0\pi_D^0$  events.

## 8.4 The Analysis Cuts

These cuts are described in terms of the acceptance for signal  $K_L \rightarrow \pi^0\pi_D^0\gamma$  MC and background  $K_L \rightarrow \pi^0\pi^0\pi_D^0$  MC. The acceptances are calculated at the stage where the cut is applied, for events in the signal region only.

### 8.4.1 Vertex $\chi^2$

The first analysis cut was on the combined vertex  $\chi^2$ . In the 1997 analysis, events were required to have  $\chi^2 \leq 5.0$ ; in 1999 they were required to have  $\chi^2 \leq 4.0$ . In both cases this cut is identical to the one done on the normalization mode. The effect of this cut was significant; in 1997 the signal mode acceptance was 81.7%, while the  $K_L \rightarrow \pi^0\pi^0\pi_D^0$  background acceptance was 29.5%. For the tighter 1999 cut the signal acceptance was 73.1% and the background acceptance was 24.8%.

This distribution is shown in Figure 8.9 for  $K_L \rightarrow \pi^0\pi^0\pi_D^0$  MC (dots) and  $K_L \rightarrow \pi^0\pi_D^0\gamma$  MC (colored histogram), just before the



cut. .

#### 8.4.2 Vertex Z-Position

The next cut required the vertex-z position to be within a range  $95m \leq VT XZ \leq 150m$ . This was mainly done to eliminate neutral  $K_L \rightarrow \pi^0 \pi^0 \pi^0$  events with pair conversion in the vacuum window, but it eliminated some  $K_L \rightarrow \pi^0 \pi^0 \pi_D^0$  background as well. The signal mode acceptance was 86.7% in 1997 and 82.8% in 1999, while the background acceptance was 72.0% in 1997 and 65.7% in 1999. This distribution is shown in Figure 8.10 for  $K_L \rightarrow \pi^0 \pi^0 \pi_D^0$  MC (dots) and  $K_L \rightarrow \pi^0 \pi_D^0 \gamma$  MC (colored histogram), just before the cut. This cut is identical to one in the normalization mode.

#### 8.4.3 $m_{ee\gamma}$

A cut was done on the mass of the  $\pi^0$  from  $\pi^0 \rightarrow e^+ e^- \gamma$  (as reconstructed by the combined vertex routine); it was required to be within 3 MeV of the  $\pi^0$  mass. This cut is identical to one done for the normalization mode. This cut had a small effect: the signal acceptance was 99.5% in 1997 and 96.9% for the tighter 1999 cut, while the background acceptance was 98.6% in 1997 and 94.5% in 1999. This distribution is shown in Figure 8.11 for  $K_L \rightarrow \pi^0 \pi^0 \pi_D^0$  MC (dots) and  $K_L \rightarrow \pi^0 \pi_D^0 \gamma$  MC (colored histogram), just before the cut.

#### 8.4.4 $m_{\gamma\gamma}$

Similarly to the previous cut, the mass of the gamma-gamma pairing returned by the combined vertexing routine was required to be within 2 MeV of the  $\pi^0$  mass. This cut is identical to one done for the normalization mode. The signal mode acceptance was 99.8% in 1997 and 91.8% for 1999, while the background acceptance was 99.4% for 1997 and 85.8% for 1999..This distribution is shown in Figure 8.12 for  $K_L \rightarrow \pi^0\pi^0\pi_D^0$  MC (dots) and  $K_L \rightarrow \pi^0\pi_D^0\gamma$  MC (colored histogram), just before the cut.

#### 8.4.5 Vertex X- and Y- Position

The combined vertex x- and y- coordinates were required to be well within a beam hole when projected onto the CsI face. The requirement was

$$0.085m \leq |x_{CsI}| \leq 0.215m$$

$$|y_{CsI}| \leq 0.065cm$$

This is identical to the cut on the normalization mode. This cut did very little; signal acceptance was 99.9% in both years, while background acceptance was 99.7% in both years. These distributions are shown in figures 8.13-8.14 for  $K_L \rightarrow \pi^0\pi^0\pi_D^0$  MC (dots) and  $K_L \rightarrow \pi^0\pi_D^0\gamma$  MC (colored histogram), just before the cut.

#### 8.4.6 Fusion $\chi^2$

As described in Chapter 7, fusion  $\chi^2$  is a variable that measures the probability of any found cluster being a "fusion" of separate EM showers from two incident particles. Fusion  $\chi^2$  was required to be less than 7.0, the same as in the normalization mode. This cut had a dramatic effect—95.9% of signal events passed in 1997, but only 24.0% of  $K_L \rightarrow \pi^0 \pi^0 \pi_D^0$  background events did. For 1999, 96.3% of signal events passed the cut, but only 25.8% of background events did.

This distribution is shown in figure 8.15 for  $K_L \rightarrow \pi^0 \pi^0 \pi_D^0$  MC (dots) and  $K_L \rightarrow \pi^0 \pi_D^0 \gamma$  MC (colored histogram), just before the cut. (Note that the distribution of fusion  $\chi^2$  for  $K_L \rightarrow \pi^0 \pi^0 \pi_D^0$  events in the box is much different than that for  $K_L \rightarrow \pi^0 \pi^0 \pi_D^0$  events in the normalization mode. Since events in the normalization mode have the extra photon found going down the beamhole, they are unlikely to have a cluster that is a fusion of two photons.)

#### 8.4.7 PP0KINE Cut

As described in the previous chapter, PP0KINE is a kinematic variable which should be positive for  $K_L \rightarrow \pi^0 \pi^0 \pi_D^0$  events, and negative for  $K_L \rightarrow \pi^0 \pi_D^0 \gamma$  events. For events in the signal box, PP0KINE was required to be less than 0.02. (This is the opposite of the normalization mode cut, which required events to have

PP0KINE  $> 0.0$ ). The signal mode PP0KINE cut produced a signal acceptance of 96.8% for 1997 and 96.9% for 1999; the background acceptance was 93.1% for 1997 and 92.2% for 1999. (The large background acceptance is due to the fact that most background events in the signal region have incorrectly paired photons or overlapping clusters, leading to a miscalculated negative PP0KINE.) This distribution is shown in figure 8.16 for  $K_L \rightarrow \pi^0 \pi^0 \pi_D^0$  MC (dots) and  $K_L \rightarrow \pi^0 \pi_D^0 \gamma$  MC (colored histogram), just before the cut.

#### 8.4.8 $m_{\pi\pi}$ Cut

The combined mass of the two pions from  $K_L \rightarrow \pi^0 \pi_D^0 \gamma$  was required to be in the range 0.3-0.4 GeV. The high-end (0.4 GeV) cut was done to eliminate  $K_L \rightarrow \pi^0 \pi^0 \pi_D^0$  background. This cut was not done on the normalization mode. The signal mode acceptance for this cut was 82.2% in 1997 and 82.0% in 1999; the background acceptance was 71.3% in 1997 and 73.7% in 1999. This distribution is shown in figure 8.17 for  $K_L \rightarrow \pi^0 \pi^0 \pi_D^0$  MC (dots) and  $K_L \rightarrow \pi^0 \pi_D^0 \gamma$  MC (colored histogram), just before the cut.

#### 8.4.9 $\pi^0 - \gamma$ Angle Cut

A cut was made on the angle between the direct emission photon and one of the two pions, randomly chosen, in the  $2\pi$  rest frame. Due to the form of the matrix element for  $K_L \rightarrow \pi^0 \pi_D^0 \gamma$ , this distribution is non-isotropic for the signal mode, while it is flat for the

$K_L \rightarrow \pi^0 \pi^0 \pi_D^0$  background. The angle  $\alpha$  was required to satisfy

$$0.25 \leq \cos(\alpha) \leq 0.9$$

This cut was not done on the normalization mode. The signal mode acceptance for this cut was 91.8% in 1997 and 91.6% in 1999, while the background acceptance was 62.6% in both years. This distribution is shown in figure 8.18 for  $K_L \rightarrow \pi^0 \pi^0 \pi_D^0$  MC (dots) and  $K_L \rightarrow \pi^0 \pi_D^0 \gamma$  MC (colored histogram), just before the cut.

#### 8.4.10 Overlapping Clusters Cut

As described in Chapter 7, the overlapping cluster routine calculated a  $\chi^2$  for each event based on the probability that one of the clusters was a "fusion" of two separate photons. The minimum overlapping cluster  $\chi^2$  was required to be less than 25.0 in 1997 and 50.0 in 1999, in both cases the same as the normalization mode.

This is the most efficient single cut. The signal mode acceptance was 64.9% for 1997 and 49.0% for the tighter 1999 cut, but the  $K_L \rightarrow \pi^0 \pi^0 \pi_D^0$  background acceptance was only 3.9% in 1997 1.8% in 1999. The distribution is shown in figure 8.19 for  $K_L \rightarrow \pi^0 \pi^0 \pi_D^0$  MC (dots) and  $K_L \rightarrow \pi^0 \pi_D^0 \gamma$  MC (colored histogram), just before the cut.

#### 8.4.11 Next-best Vertex $\chi^2$ Cut

Events with a next-best combined vertex  $\chi^2$  within 25.0 of the chosen value were cut, to eliminate events with an ambiguous vertex. The same cut was done on the normalization mode. The signal mode acceptance for this cut was 73.6% in both 1997 and 1999, while the background acceptance was 34.6% in 1997 and 31.1% in 1999. This distribution is shown in figure 8.20 for  $K_L \rightarrow \pi^0 \pi^0 \pi_D^0$  MC (dots) and  $K_L \rightarrow \pi^0 \pi_D^0 \gamma$  MC (colored histogram), just before the cut.

#### 8.4.12 $\gamma\gamma$ Mispairing Cut

Events were cut if any pair of photons (other than the correct pairing) gave a mass in the range 0.130-0.155 GeV. This was done to eliminate events where the photons were mispaired; the same cut was done on the normalization mode. The signal acceptance for this cut was 81.8% in 1997 and 83.6% in 1999, while the background acceptance was 15.3% in 1997. For 1999 the background acceptance at this stage cannot be calculated since the cut eliminated all of the 14 remaining events in the signal region. This distribution is shown in figure 8.21 for  $K_L \rightarrow \pi^0 \pi^0 \pi_D^0$  MC (dots) and  $K_L \rightarrow \pi^0 \pi_D^0 \gamma$  MC (colored histogram), just before the cut.

#### 8.4.13 Summary of Cuts

The effect of the cuts is summarized in tables 8.1 and 8.2, which show the total acceptance after each cut for both  $K_L \rightarrow \pi^0 \pi_D^0 \gamma$  and

$K_L \rightarrow \pi^0 \pi^0 \pi_D^0$  MC, for 1997 and 1999 respectively.

## 8.5 Opening the Signal Regions

At this stage, there were 4  $K_L \rightarrow \pi^0 \pi^0 \pi_D^0$  MC events left in the signal box for 4.72 generated 1997 background MC fluxes. Figure 8.22 shows the box after all cuts for  $K_L \rightarrow \pi^0 \pi^0 \pi_D^0$  Monte Carlo. Upon opening the signal box for 1997 data, zero events were discovered. The box for data events (after all cuts) is shown in figure 8.23.

There were 0  $K_L \rightarrow \pi^0 \pi^0 \pi_D^0$  events left in the signal region for 3.77 generated 1999 background fluxes; this is shown in figure 8.24. Upon opening the signal region for 1999 data, one event was discovered, as shown in Figure 25 .

Cut	$K_L \rightarrow \pi^0 \pi_D^0 \gamma$ MC	$K_L \rightarrow \pi^0 \pi^0 \pi_D^0$ MC
START	100	100
Vertex $\chi^2$	81.7	29.5
Vertex Z position	70.8	21.3
$m_{ee\gamma}$	70.5	20.9
$m_{\gamma\gamma}$	70.4	20.9
Vertex x/y Projection	70.3	20.8
Fusion $\chi^2$	67.5	4.98
PP0KINE	65.4	4.64
$m_{\pi\pi}$	53.7	3.40
$\pi^0 - \gamma$ angle	49.3	2.13
Overlapping clusters	32.0	0.083
Next-best $\chi^2$	23.5	0.028
Mispairing Cut ( $\gamma - \gamma$ mass)	19.3	0.004

Table 8.1: Total acceptance (in percent) of each analysis cut for 1997 signal and background Monte Carlo in the signal box, after the crunch and bad run/spill cuts .

Cut	$K_L \rightarrow \pi^0 \pi_D^0 \gamma$ MC	$K_L \rightarrow \pi^0 \pi^0 \pi_D^0$ MC
START	100	100
Vertex $\chi^2$	73.0	24.8
Vertex Z position	60.5	16.2
$m_{ee\gamma}$	58.7	15.4
$m_{\gamma\gamma}$	53.9	13.2
Vertex x/y Projection	53.9	13.2
Fusion $\chi^2$	51.9	3.41
PP0KINE	50.2	3.15
$m_{\pi\pi}$	41.3	2.32
$\pi^0 - \gamma$ angle	37.8	1.45
Overlapping clusters	18.5	0.026
Next-best $\chi^2$	13.7	0.0081
Mispairing Cut ( $\gamma - \gamma$ mass)	11.4	0

Table 8.2: Total acceptance (in percent) of each analysis cut for 1999 signal and background Monte Carlo in the signal region, after the crunch and bad run/spill cuts.



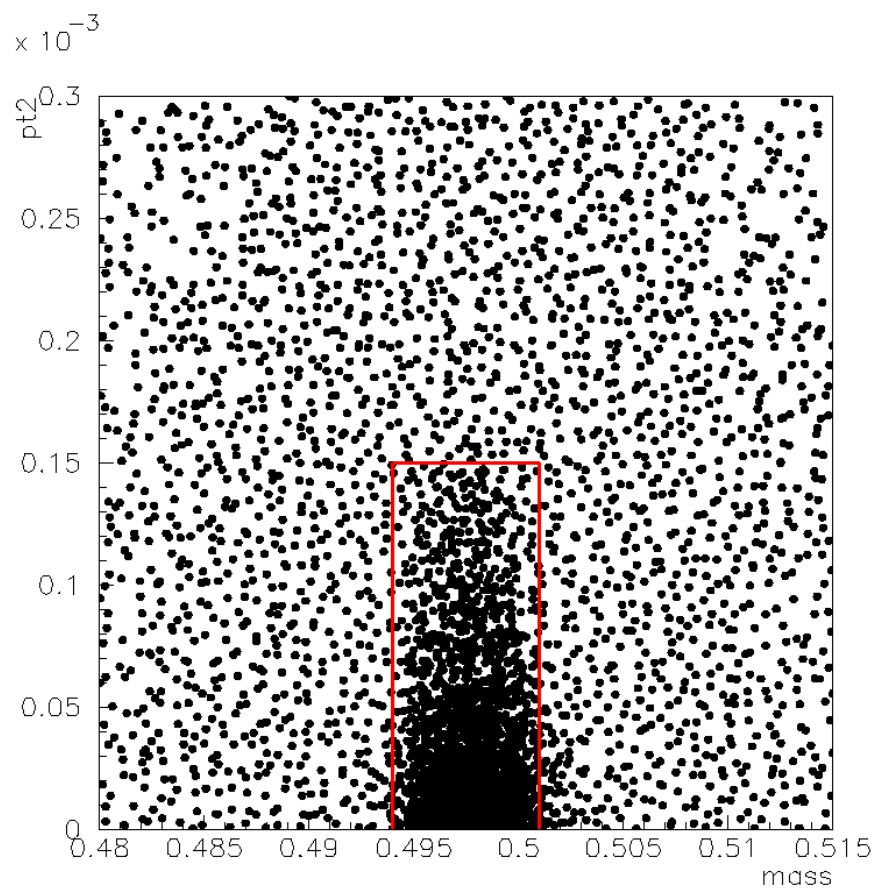


Figure 8.1:  $m_{ee\gamma\gamma\gamma}$  (in  $\text{GeV}/c^2$ ) vs  $p_t^2$  (in  $(\text{GeV}/c)^2$ ) for  $K_L \rightarrow \pi^0 \pi_D^0 \gamma$  MC events after the bad run/spill cut. The signal box is marked.

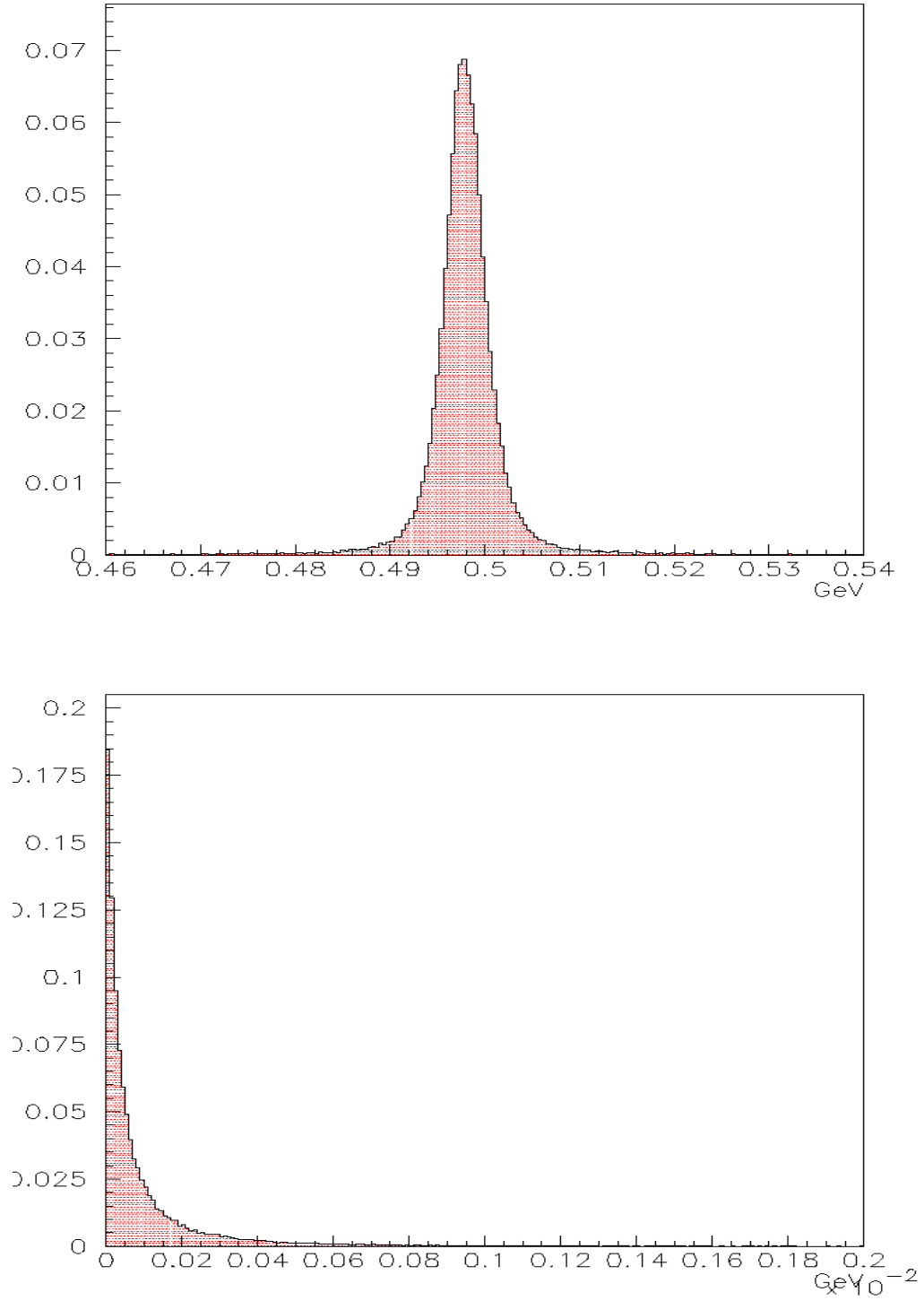


Figure 8.2:  $m_{ee\gamma\gamma\gamma}$  (top, in  $\text{GeV}/c^2$ ) and  $p_t^2$  (bottom, in  $(\text{GeV}/c)^2$ ) distributions for 1999 signal mode events past the crunch, used as an input in determining the 1999 signal region.

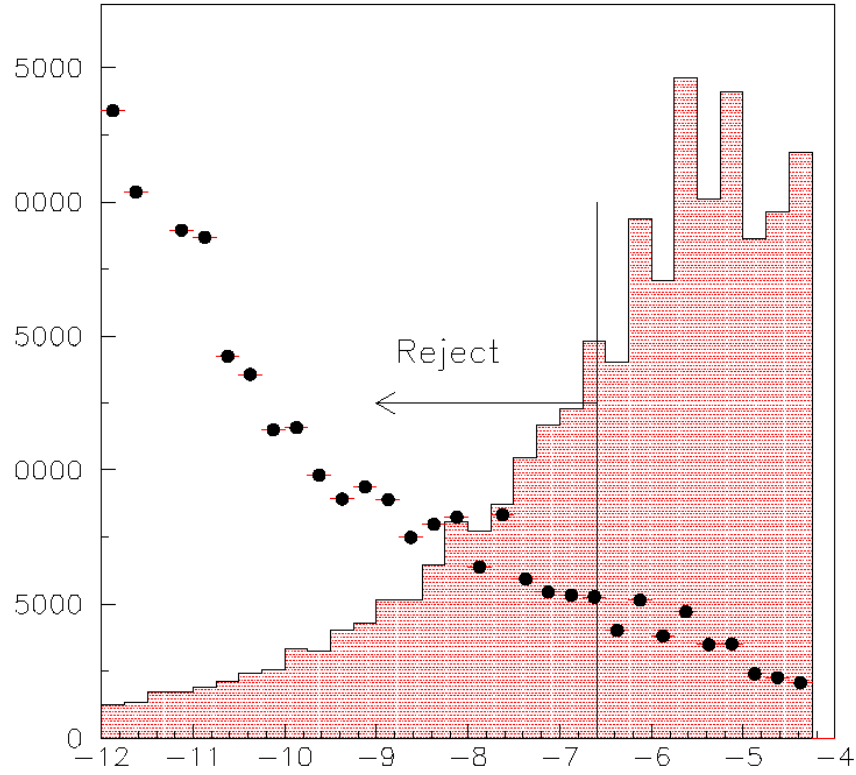


Figure 8.3: Logarithm of  $P(m_{ee\gamma\gamma\gamma}, p_t^2)$  for 1999  $K_L \rightarrow \pi^0 \pi_D^0 \gamma$  MC events (red) and  $K_L \rightarrow \pi^0 \pi^0 \pi_D^0$  MC events (dots) after the bad run/spill cut. Events with a value greater than -6.6 are considered to be in the signal region.

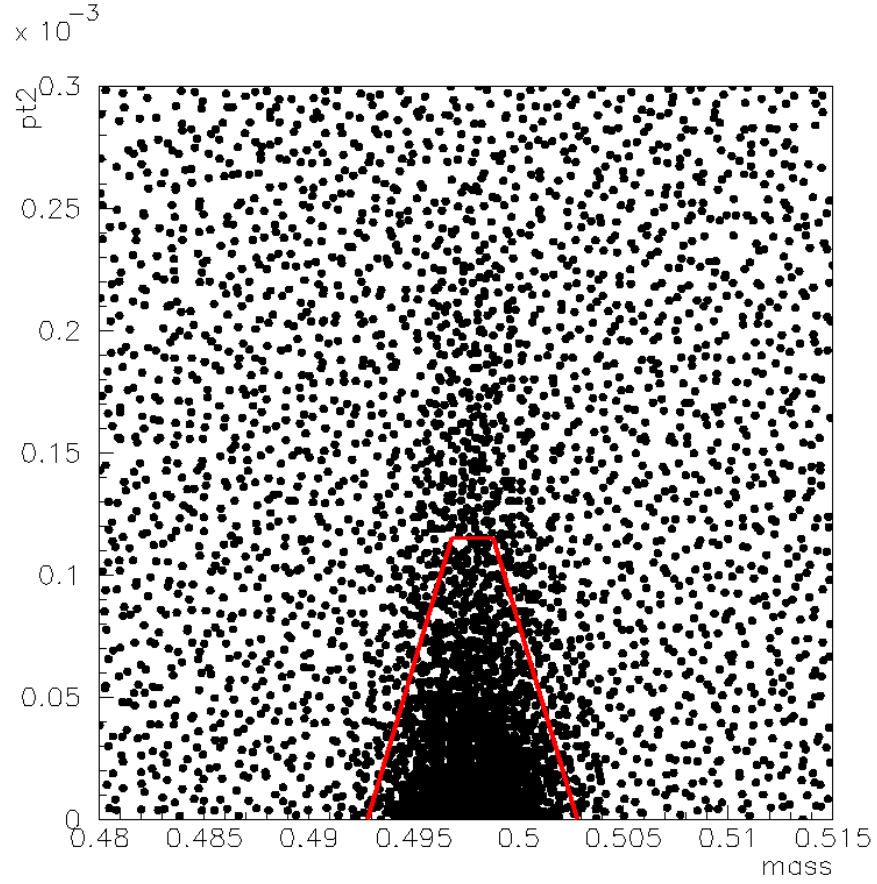


Figure 8.4:  $m_{ee\gamma\gamma\gamma}$  (in  $\text{GeV}/c^2$ ) vs.  $p_t^2$  (in  $(\text{GeV}/c)^2$ ) for 1999  $K_L \rightarrow \pi^0 \pi_D^0 \gamma$  MC events after the bad run/spill cut. The signal region is marked.

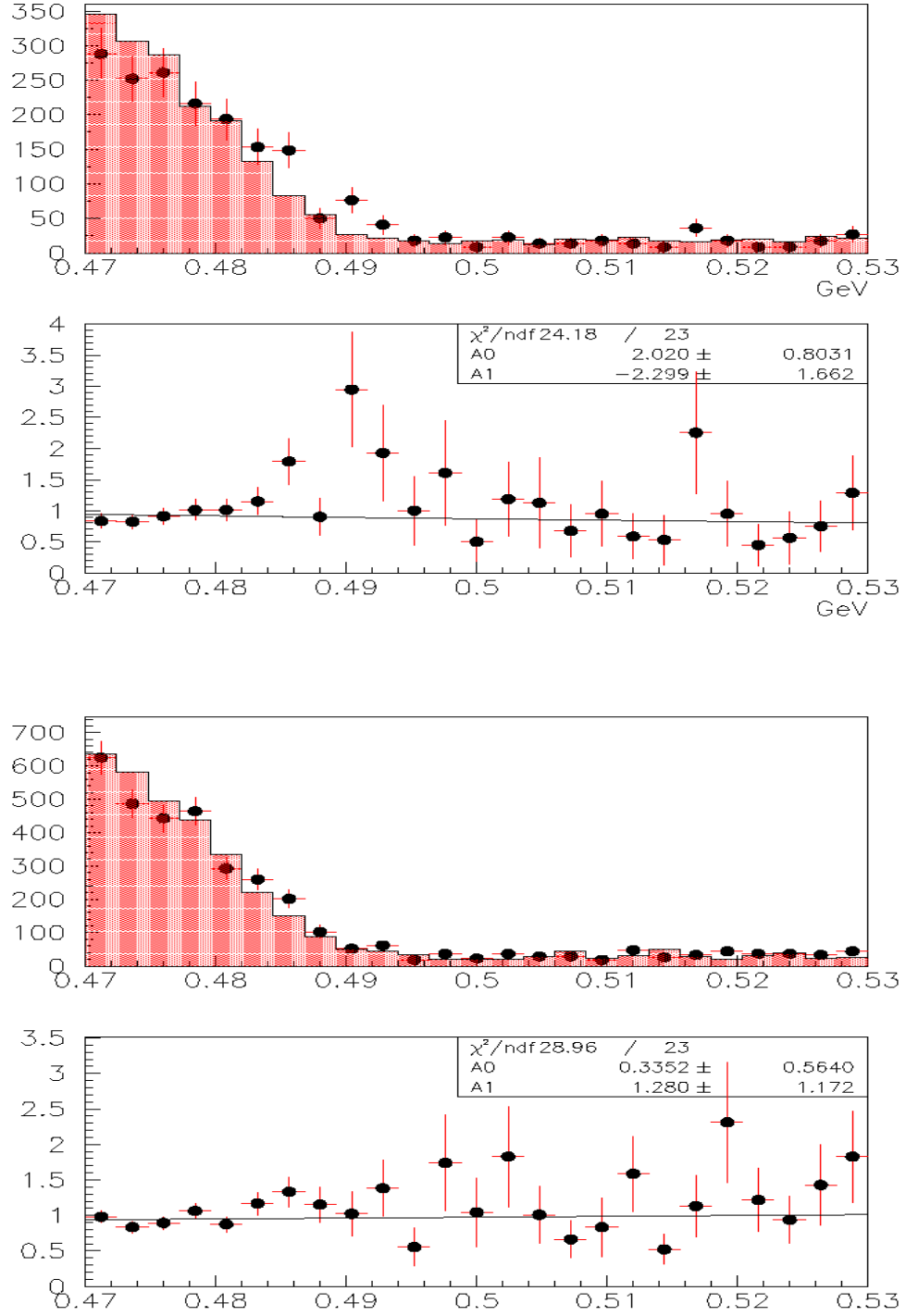


Figure 8.5: Total mass  $m_{ee\gamma\gamma\gamma}$  in  $\text{GeV}/c^2$  for events outside the signal region for 1997 (top) and 1999 (bottom) running, after all cuts. Dots are data, colored histograms are  $K_L \rightarrow \pi^0\pi^0\pi_D^0$  MC. The data/MC ratios for each year are shown below the comparison plots.

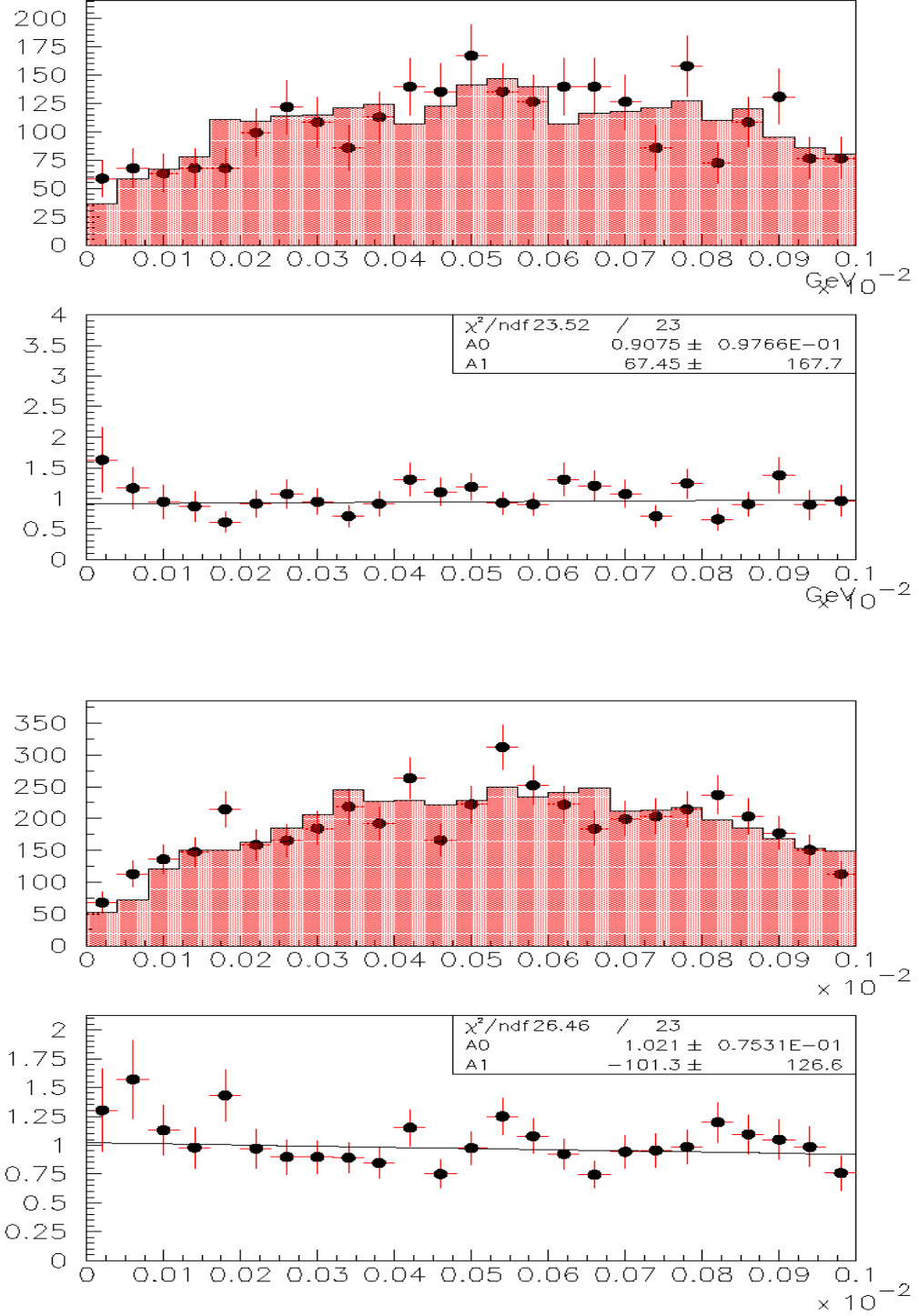


Figure 8.6:  $p_t^2$  in  $(\text{GeV}/c)^2$  for events outside the signal region for 1997 (top) and 1999 (bottom) running, after all cuts. Dots are data, colored histograms are  $K_L \rightarrow \pi^0 \pi^0 \pi_D^0$  MC. The data/MC ratios for each year are shown below the comparison plots.

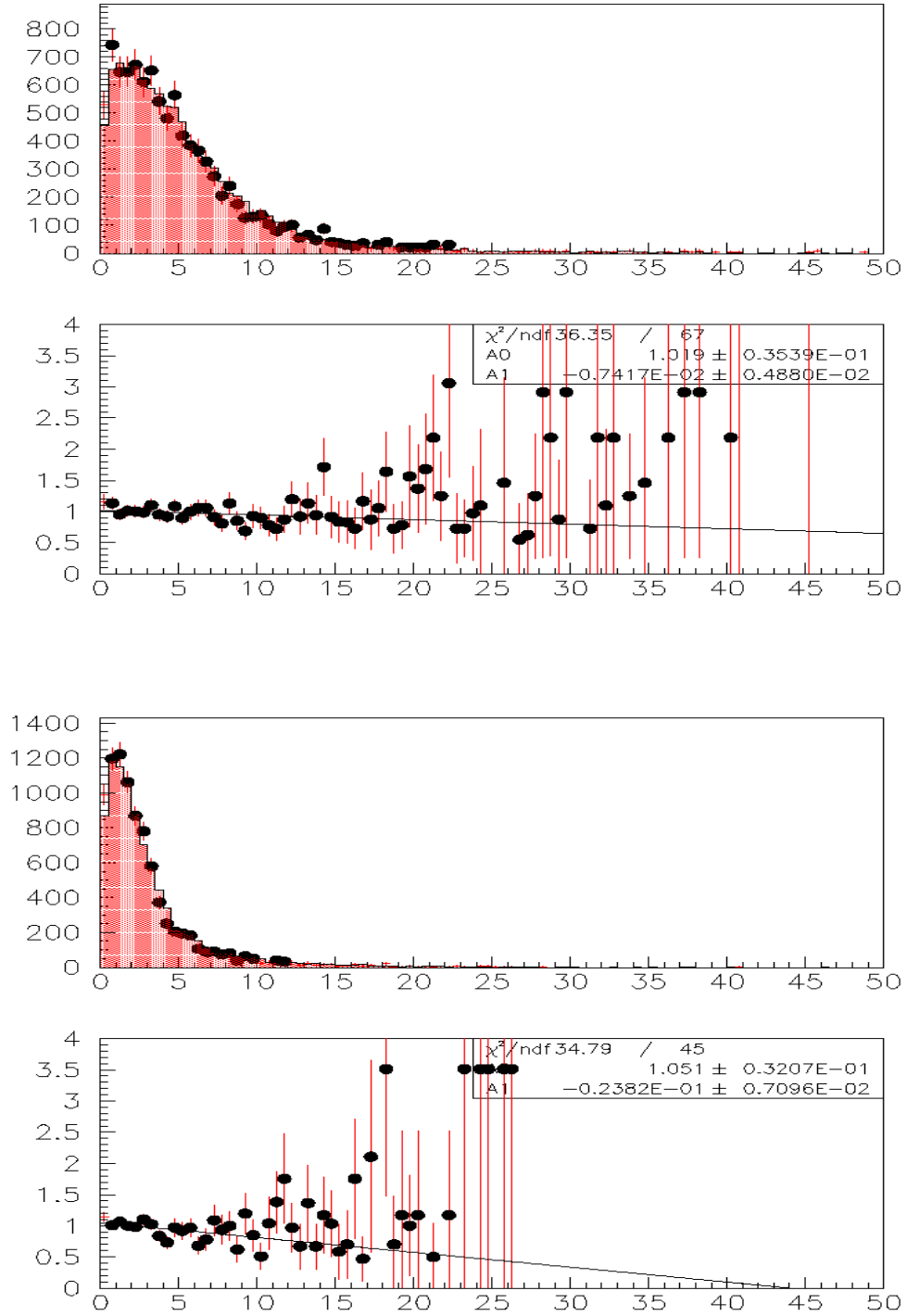


Figure 8.7: Vertex  $\chi^2$  for events outside the signal region for 1997 (top) and 1999 (bottom) running, after all cuts. Dots are data, colored histograms are  $K_L \rightarrow \pi^0 \pi^0 \pi_D^0$  MC. The data/MC ratios for each year are shown below the comparison plots.

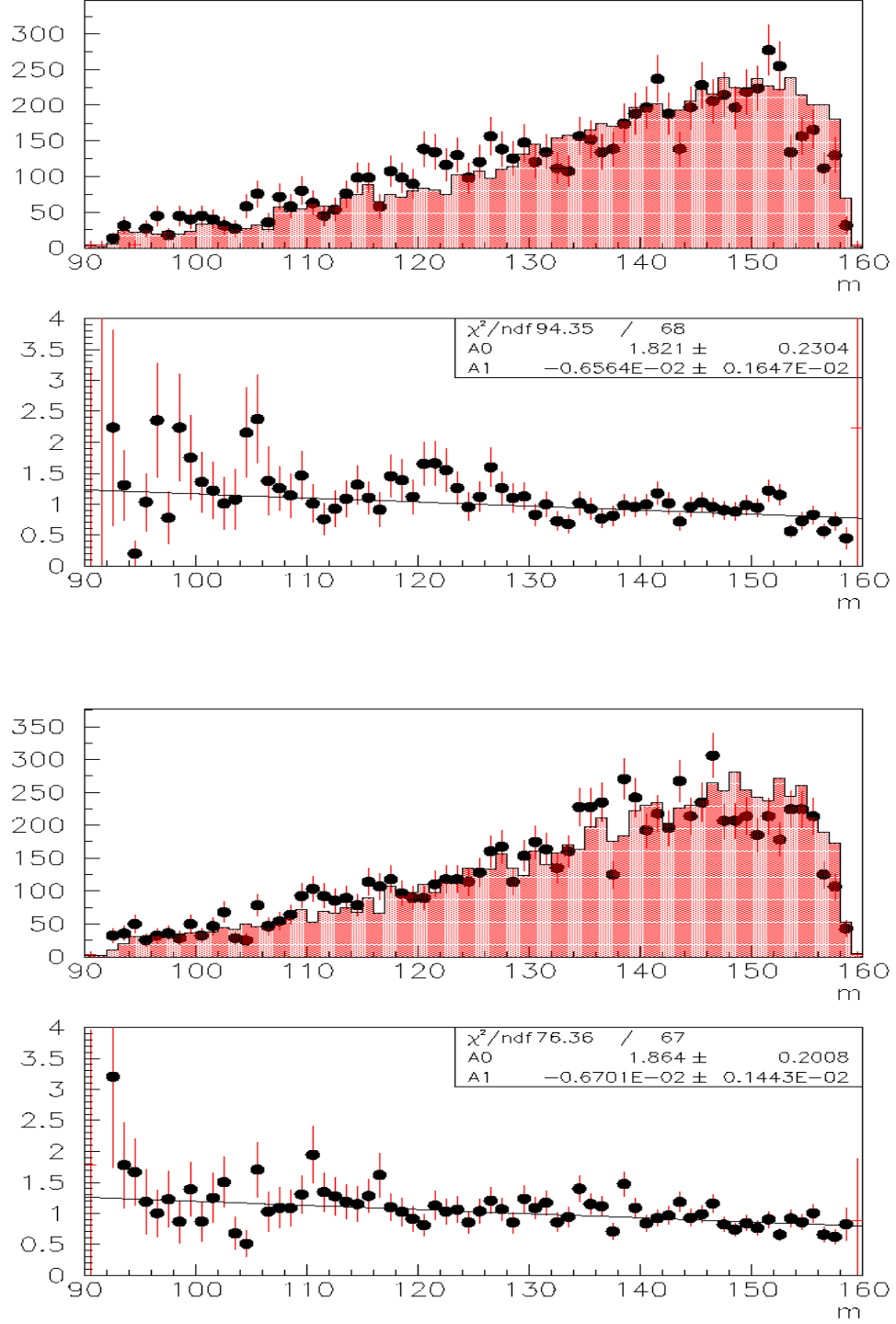


Figure 8.8: Vertex z-position in meters for events outside the signal region for 1997 (top) and 1999 (bottom) running, after all cuts. Dots are data, colored histograms are  $K_L \rightarrow \pi^0 \pi^0 \pi_D^0$  MC. The data/MC ratios for each year are shown below the comparison plots.



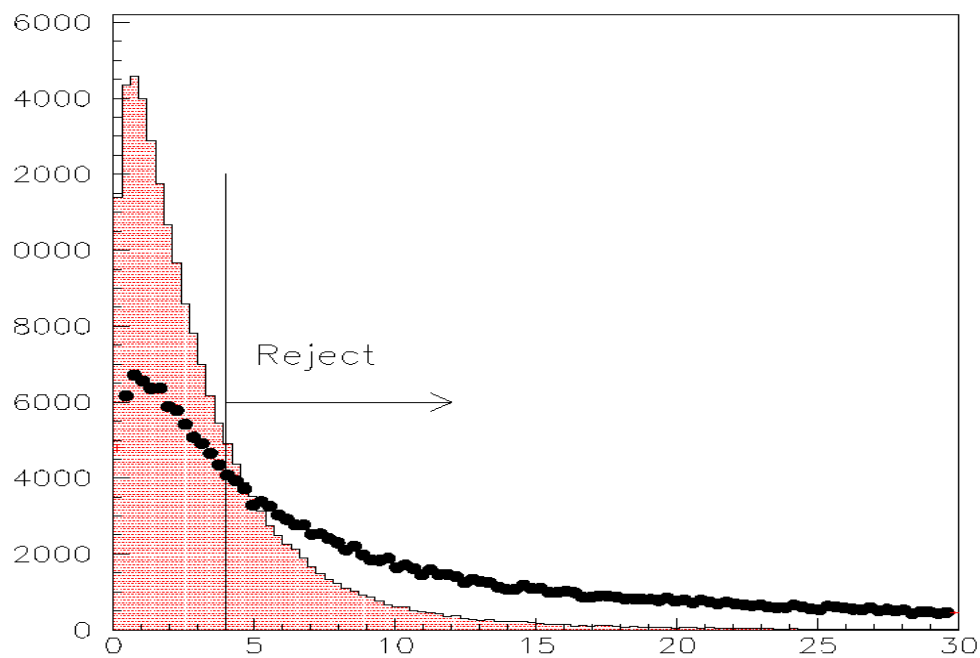
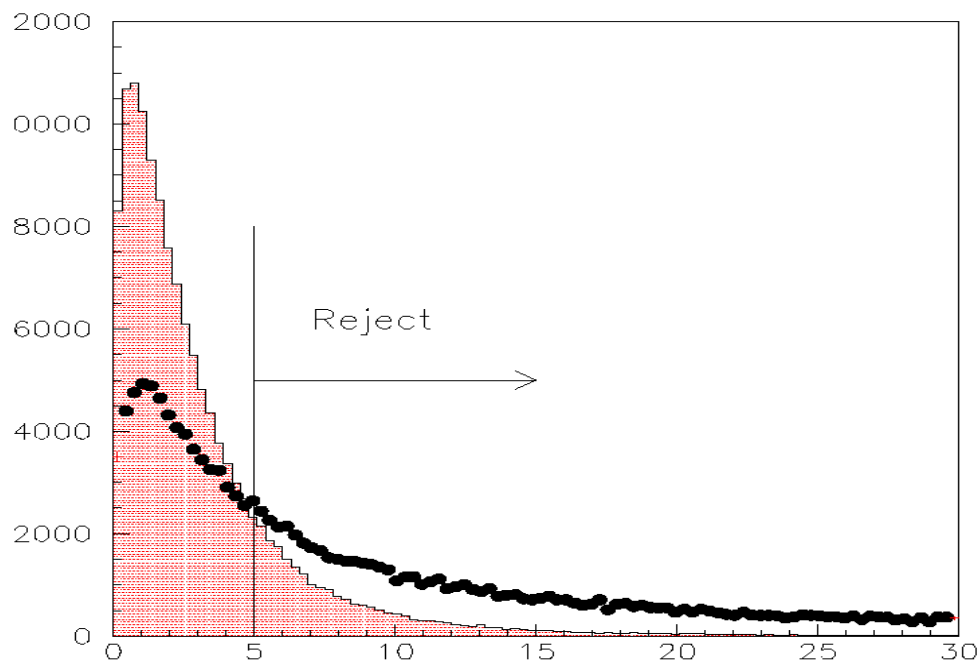


Figure 8.9: Vertex  $\chi^2$  for events inside the signal region for 1997 (top) and 1999 (bottom) running, before the cut. Dots are background  $K_L \rightarrow \pi^0 \pi^0 \pi_D^0$  MC, colored histogram is  $K_L \rightarrow \pi^0 \pi_D^0 \gamma$  signal MC.

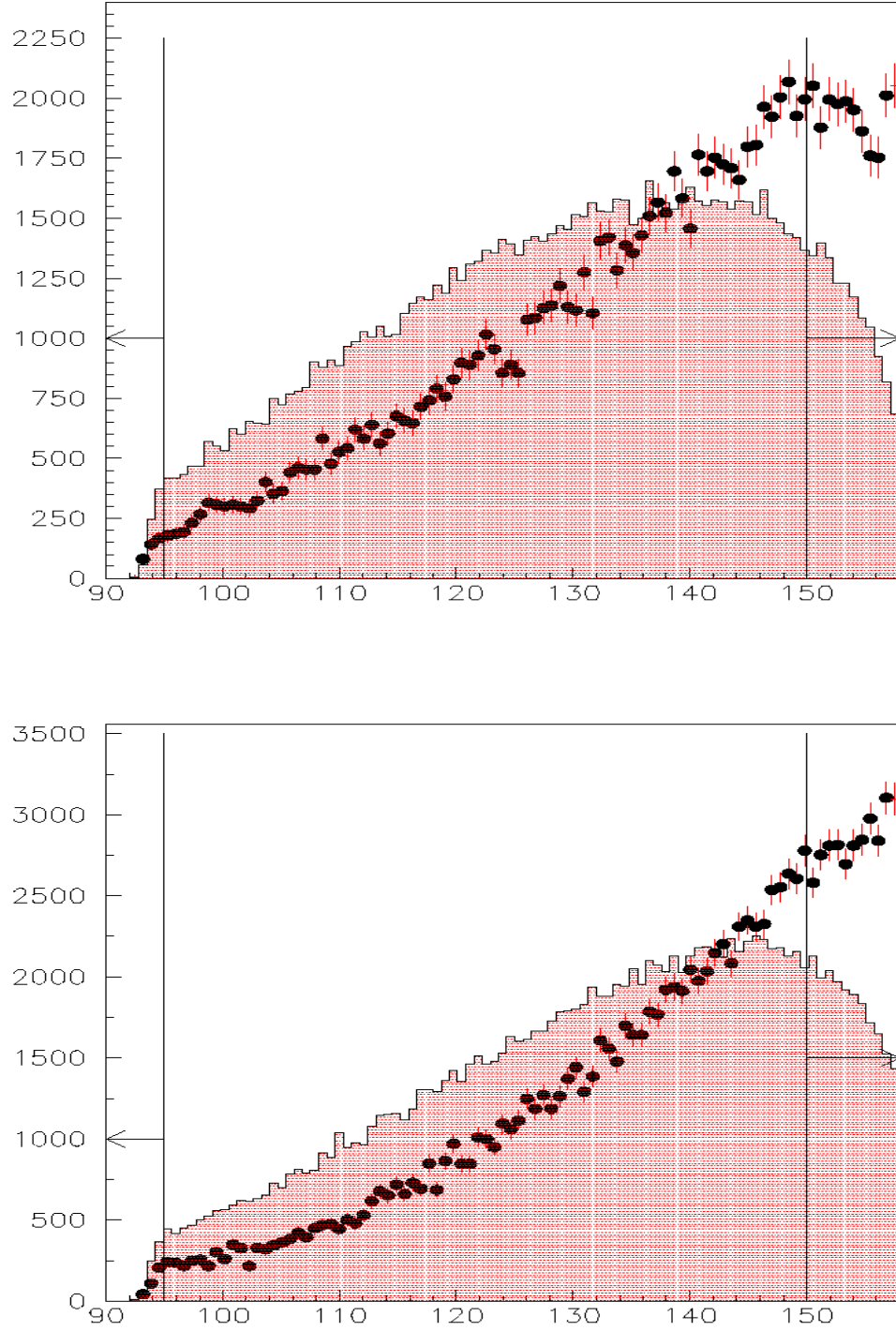


Figure 8.10: Vertex z-position in meters for events inside the signal region for 1997 (top) and 1999 (bottom) running, before the cut. Dots are background  $K_L \rightarrow \pi^0 \pi_D^0$  MC, colored histogram is  $K_L \rightarrow \pi^0 \pi_D^0 \gamma$  signal MC.

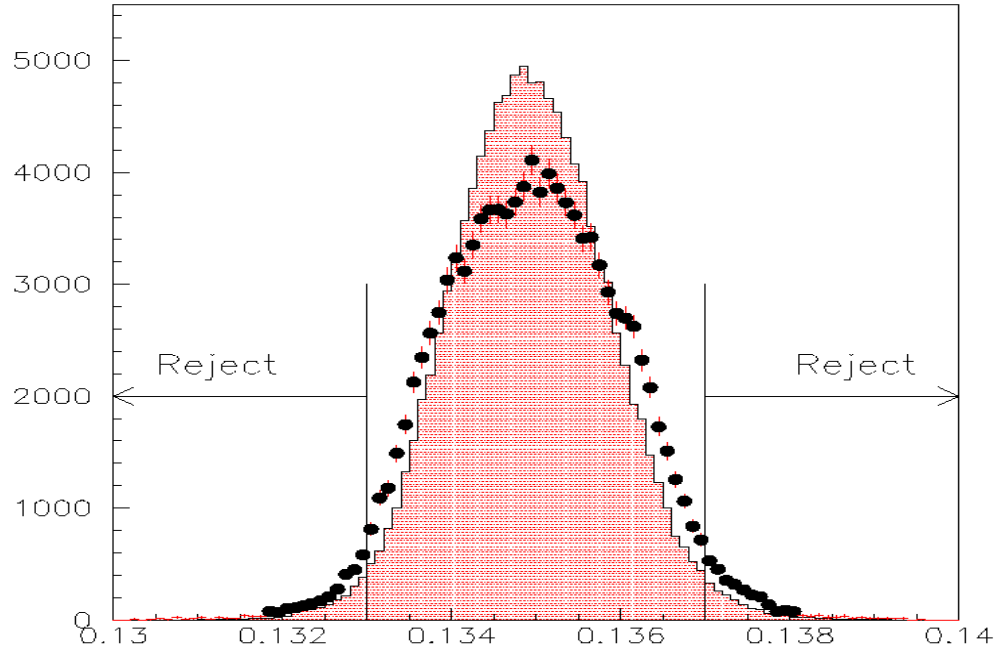
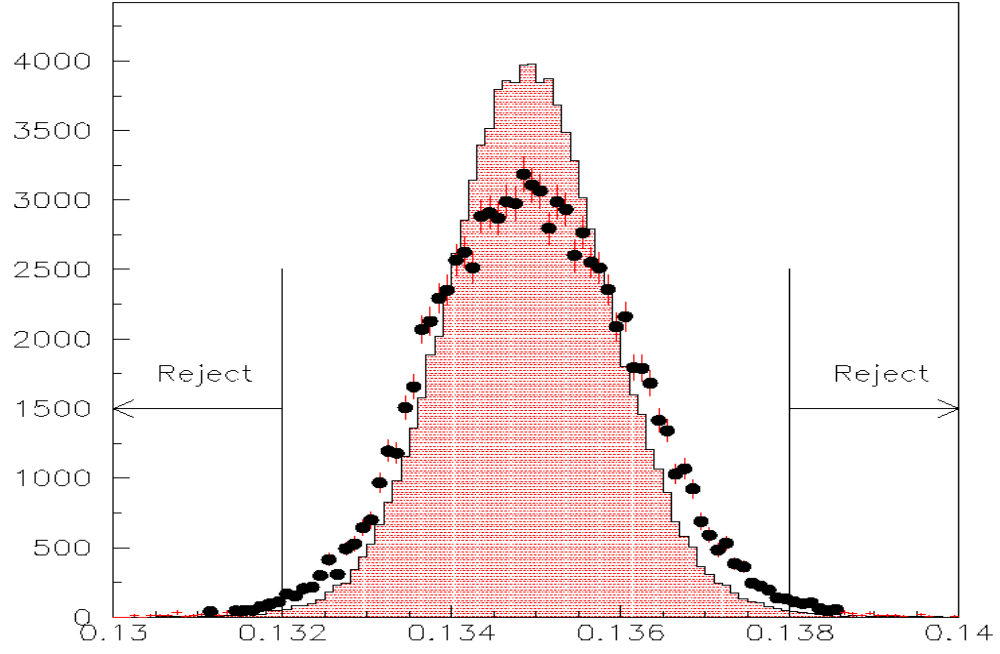


Figure 8.11:  $m_{ee\gamma}$  in  $GeV/c^2$  for events inside the signal region for 1997 (top) and 1999 (bottom) running, before the cut. Dots are background  $K_L \rightarrow \pi^0 \pi^0 \pi_D^0$  MC, colored histogram is  $K_L \rightarrow \pi^0 \pi_D^0 \gamma$  signal MC.

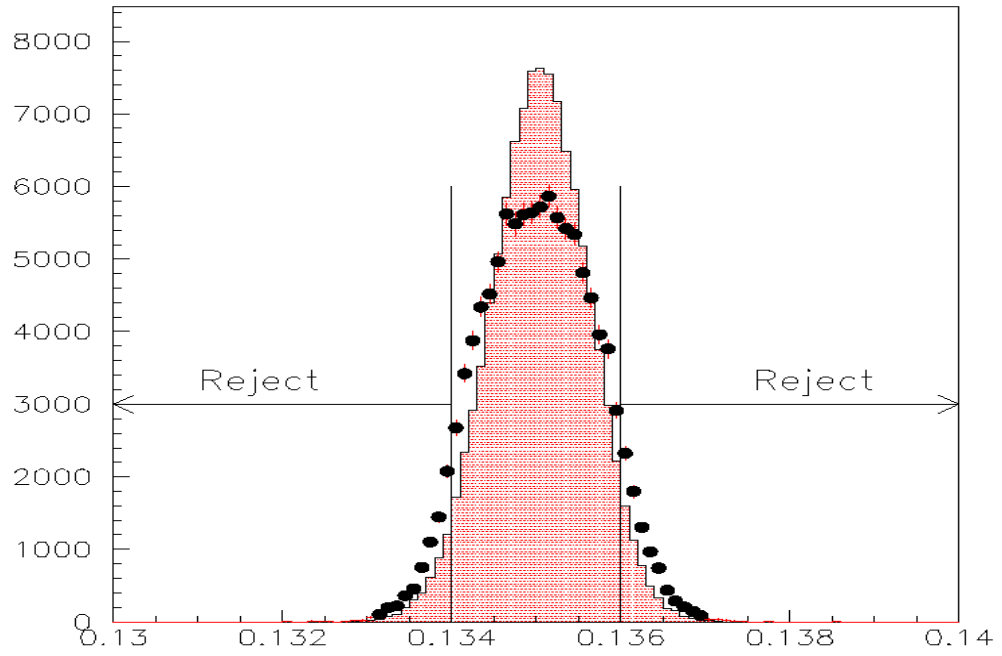
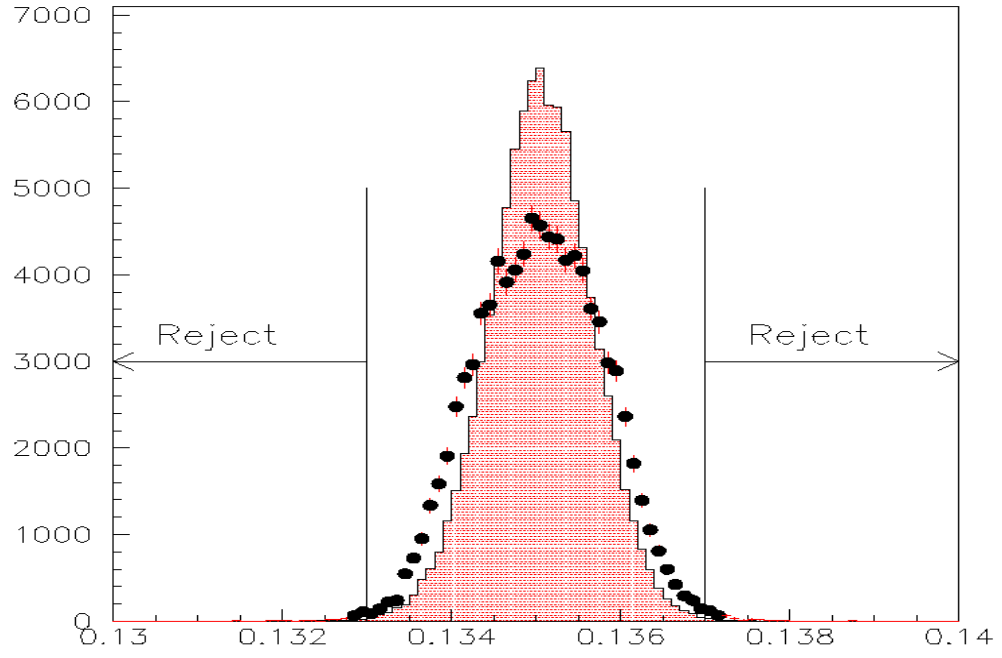


Figure 8.12:  $m_{\gamma\gamma}$  in  $\text{GeV}/c^2$  for events inside the signal region for 1997 (top) and 1999 (bottom) running, before the cut. Dots are background  $K_L \rightarrow \pi^0 \pi^0 \pi_D^0$  MC, colored histogram is  $K_L \rightarrow \pi^0 \pi_D^0 \gamma$  signal MC.

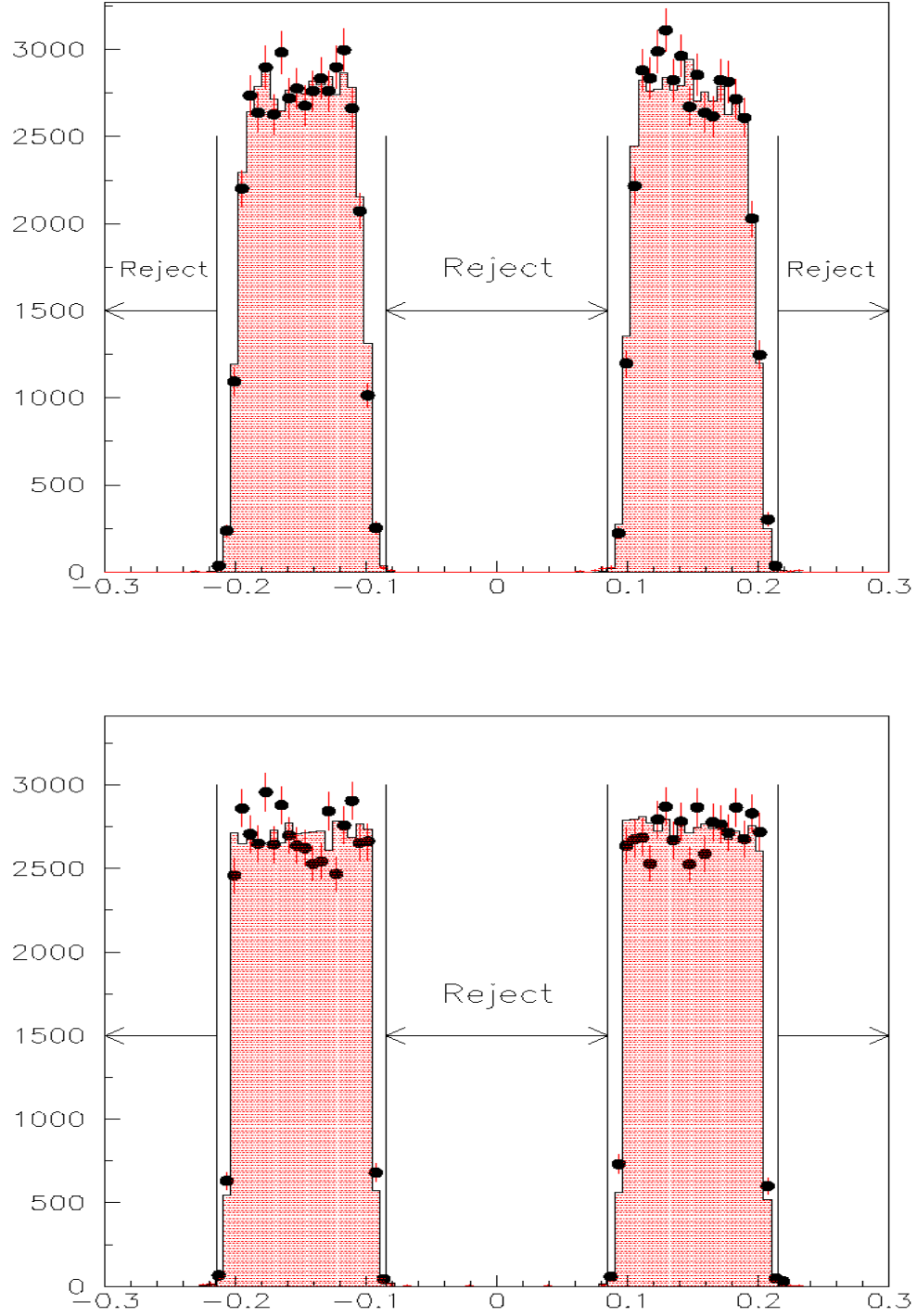


Figure 8.13: Vertex x-projection at the calorimeter face in meters for events inside the signal region for 1997 (top) and 1999 (bottom) running, before the cut. Dots are background  $K_L \rightarrow \pi^0 \pi^0 \pi_D^0$  MC, colored histogram is  $K_L \rightarrow \pi^0 \pi_D^0 \gamma$  signal MC.

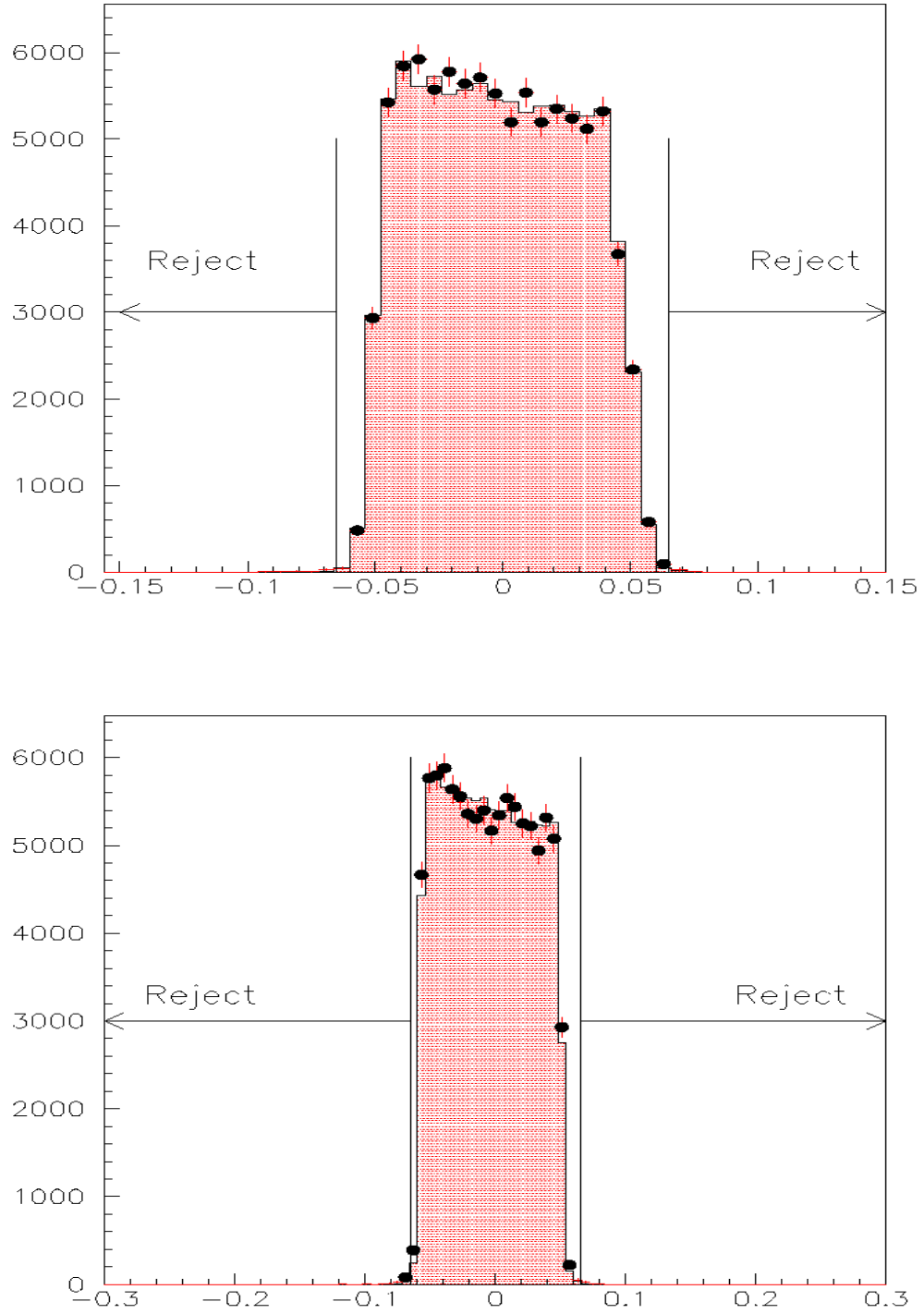


Figure 8.14: Vertex y-projection at the calorimeter face in meters for events inside the signal region for 1997 (top) and 1999 (bottom) running, before the cut. Dots are background  $K_L \rightarrow \pi^0 \pi^0 \pi_D^0$  MC, colored histogram is  $K_L \rightarrow \pi^0 \pi_D^0 \gamma$  signal MC.

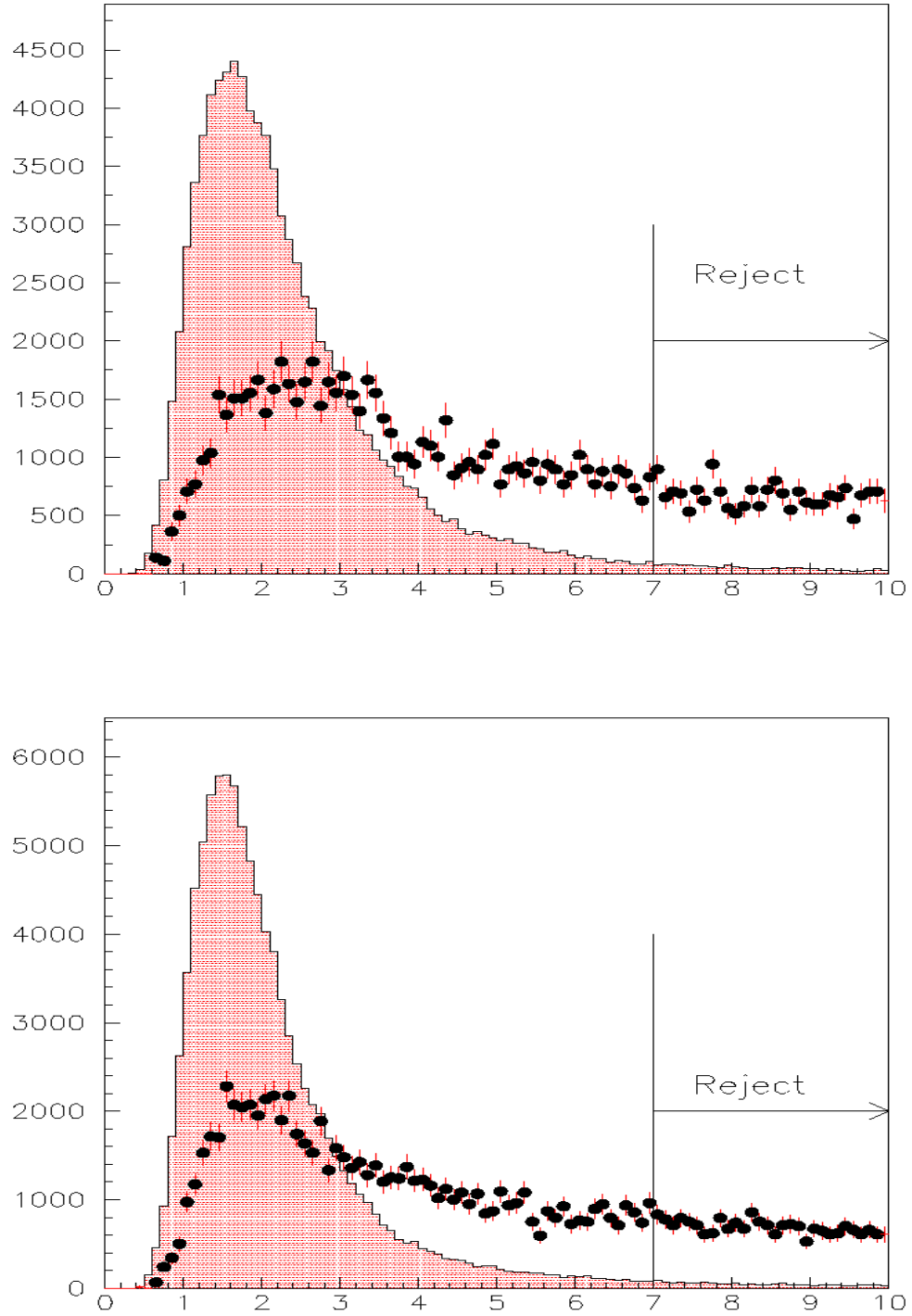


Figure 8.15: Fusion  $\chi^2$  for events inside the signal region for 1997 (top) and 1999 (bottom) running, before the cut. Dots are background  $K_L \rightarrow \pi^0 \pi^0 \pi_D^0$  MC, colored histogram is  $K_L \rightarrow \pi^0 \pi_D^0 \gamma$  signal MC.

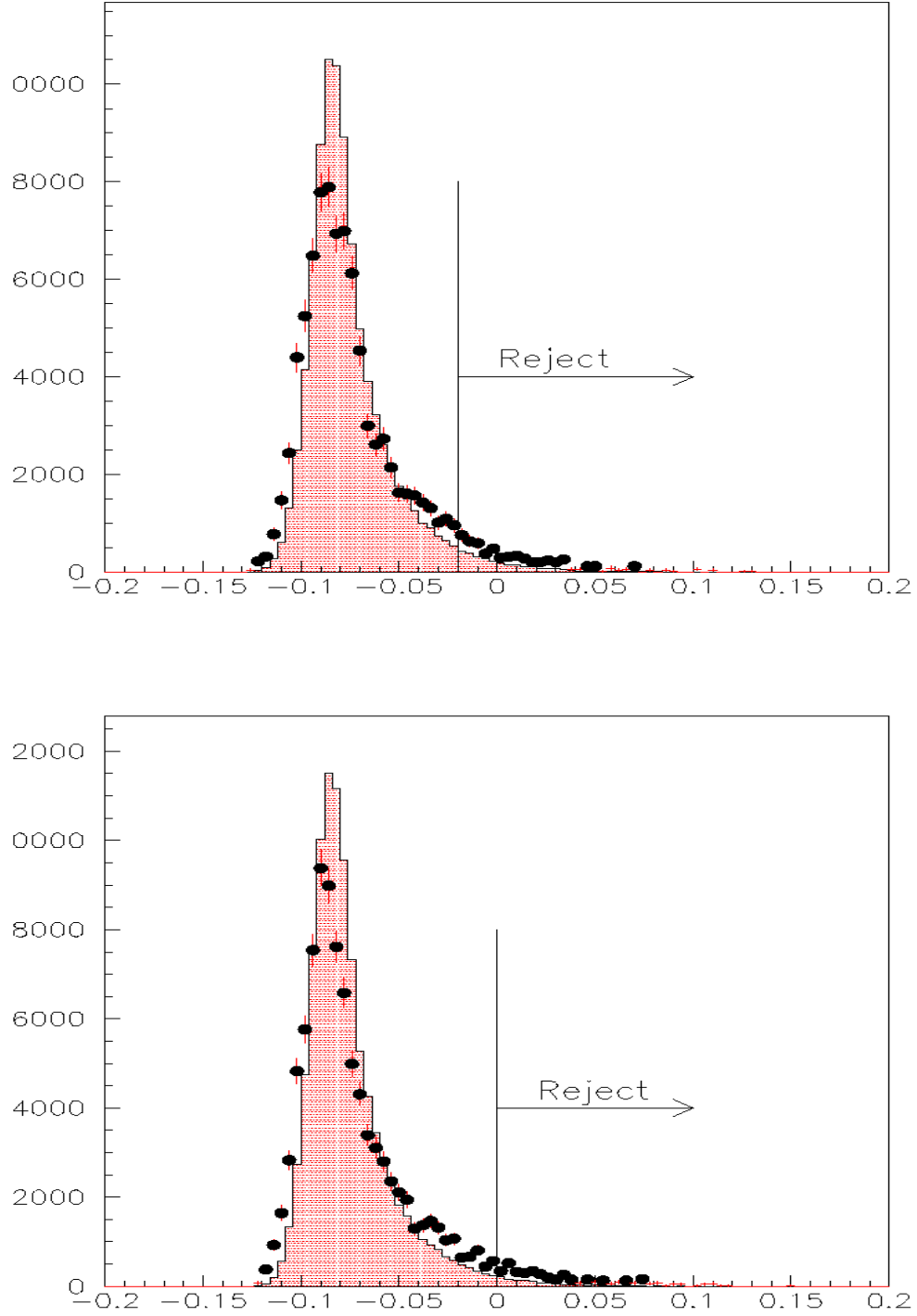


Figure 8.16: PP0KINE for events inside the signal region for 1997 (top) and 1999 (bottom) running, before the cut. Dots are background  $K_L \rightarrow \pi^0 \pi^0 \pi_D^0$  MC, colored histogram is  $K_L \rightarrow \pi^0 \pi_D^0 \gamma$  signal MC.



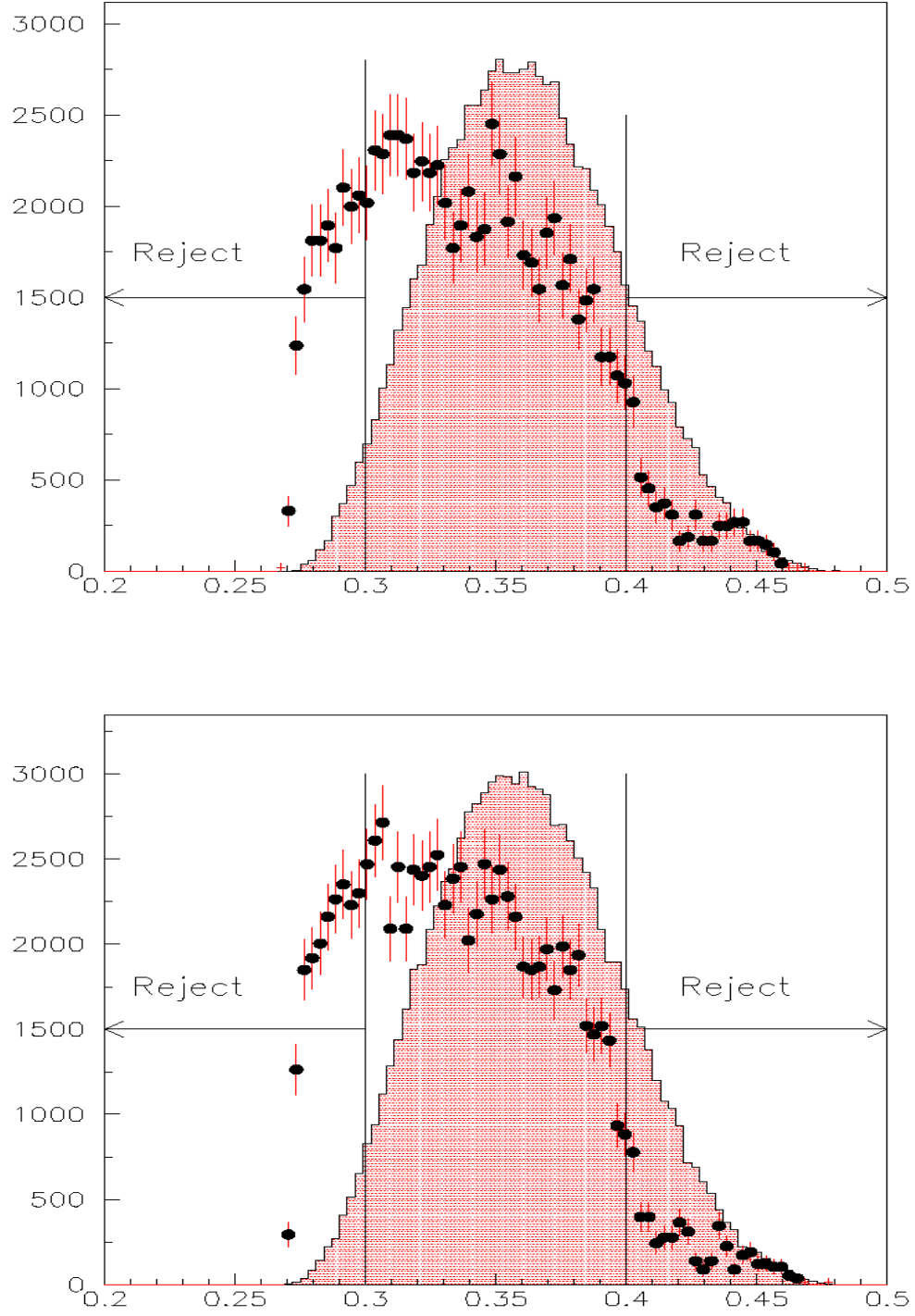


Figure 8.17:  $m_{\pi\pi}$  in  $\text{GeV}/c^2$  for events inside the signal region for 1997 (top) and 1999 (bottom) running, before the cut. Dots are background  $K_L \rightarrow \pi^0 \pi^0 \pi_D^0$  MC, colored histogram is  $K_L \rightarrow \pi^0 \pi_D^0 \gamma$  signal MC.

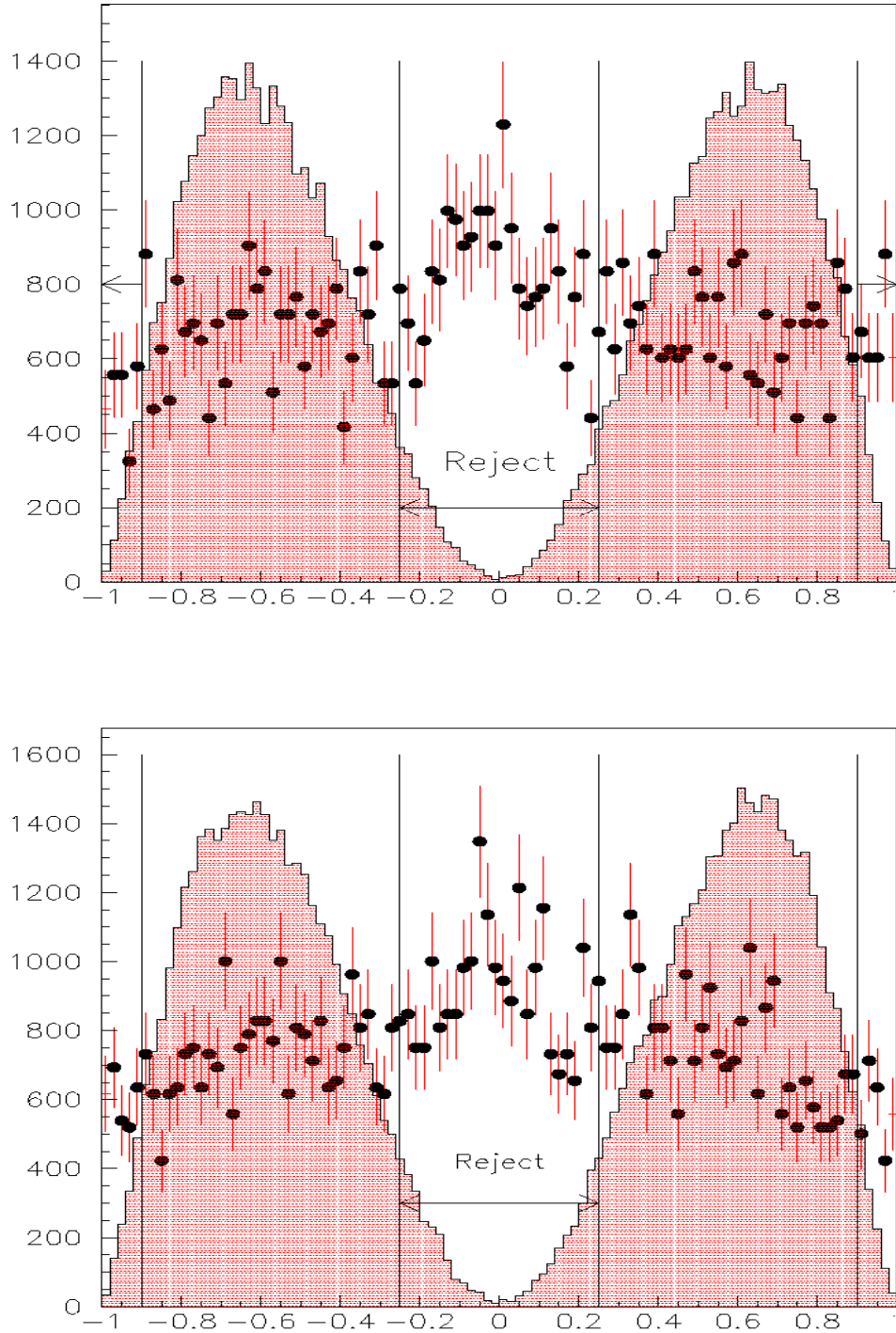


Figure 8.18: Cosine of the angle between a randomly chosen  $\pi^0$  and the direct emission photon, in the  $2\pi$  rest frame for events inside the signal region for 1997 (top) and 1999 (bottom) running, before the cut. Dots are background  $K_L \rightarrow \pi^0 \pi_D^0$  MC, colored histogram is  $K_L \rightarrow \pi^0 \pi_D^0 \gamma$  signal MC.

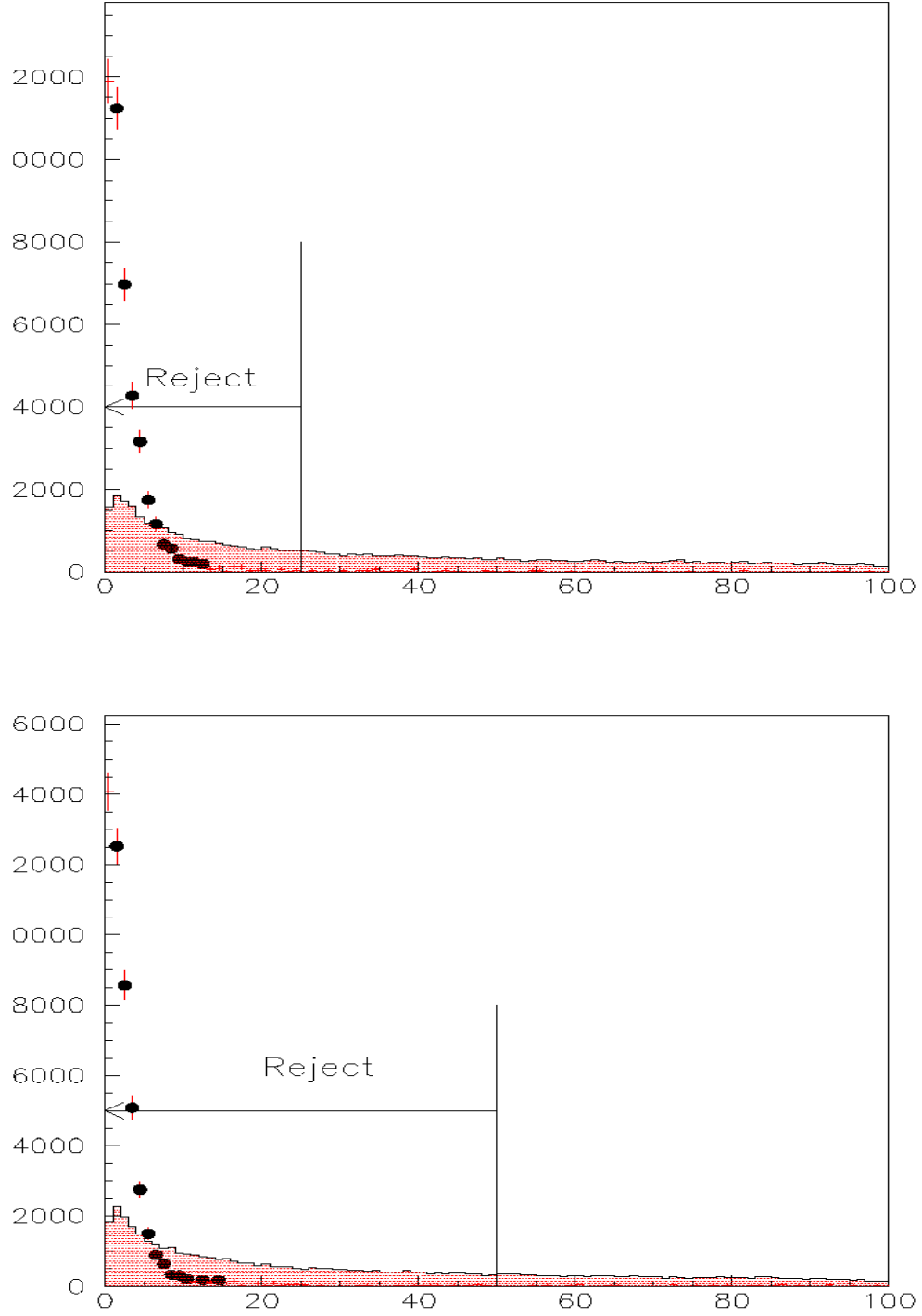


Figure 8.19: Overlapping cluster  $\chi^2$  for events inside the signal region for 1997 (top) and 1999 (bottom) running, before the cut. Dots are background  $K_L \rightarrow \pi^0 \pi^0 \pi_D^0$  MC, colored histogram is  $K_L \rightarrow \pi^0 \pi_D^0 \gamma$  signal MC.

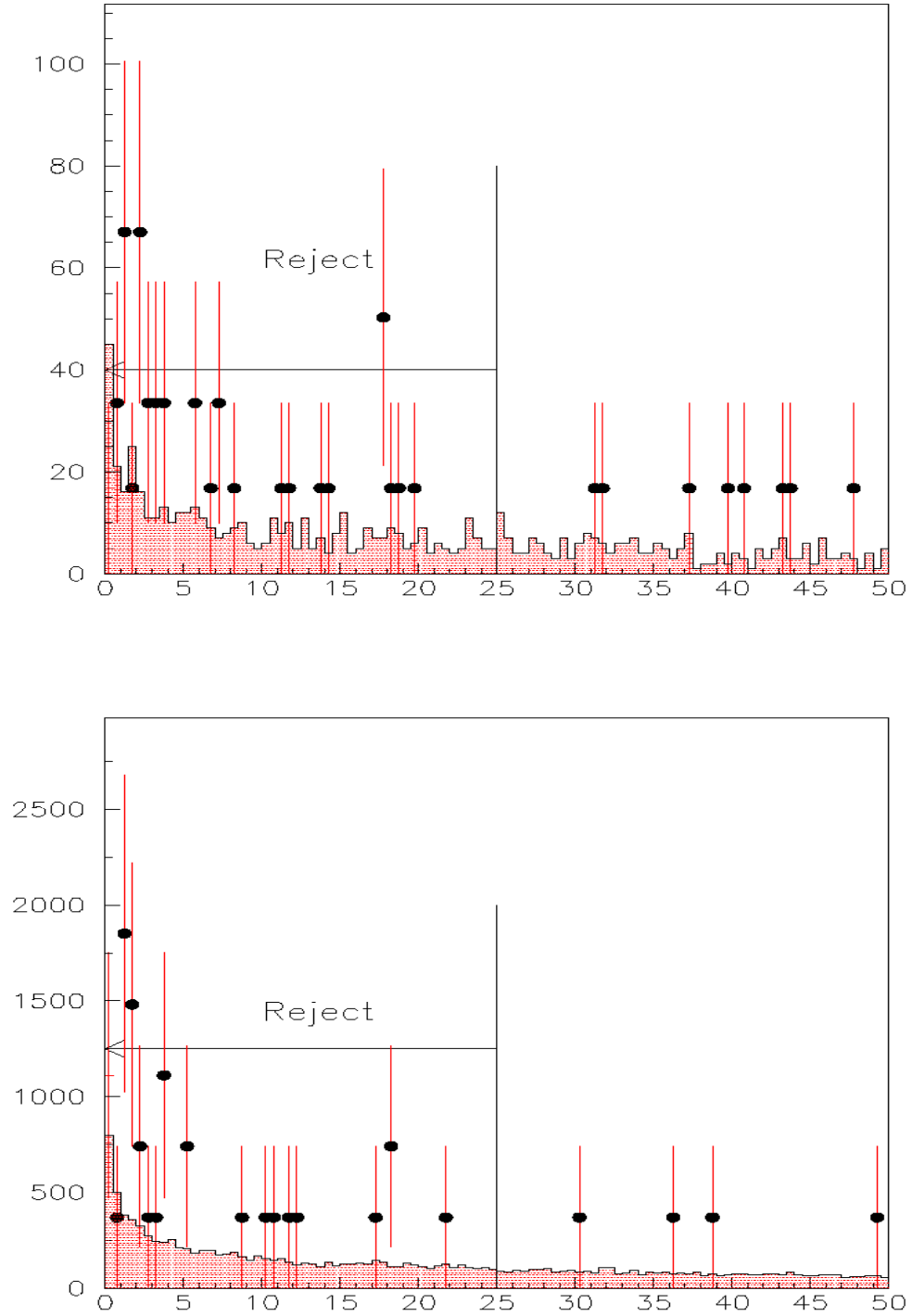


Figure 8.20: Next best minus best vertex  $\chi^2$  for events inside the signal region for 1997 (top) and 1999 (bottom) running, before the cut. Dots are background  $K_L \rightarrow \pi^0 \pi^0 \pi_D^0$  MC, colored histogram is  $K_L \rightarrow \pi^0 \pi_D^0 \gamma$  signal MC.

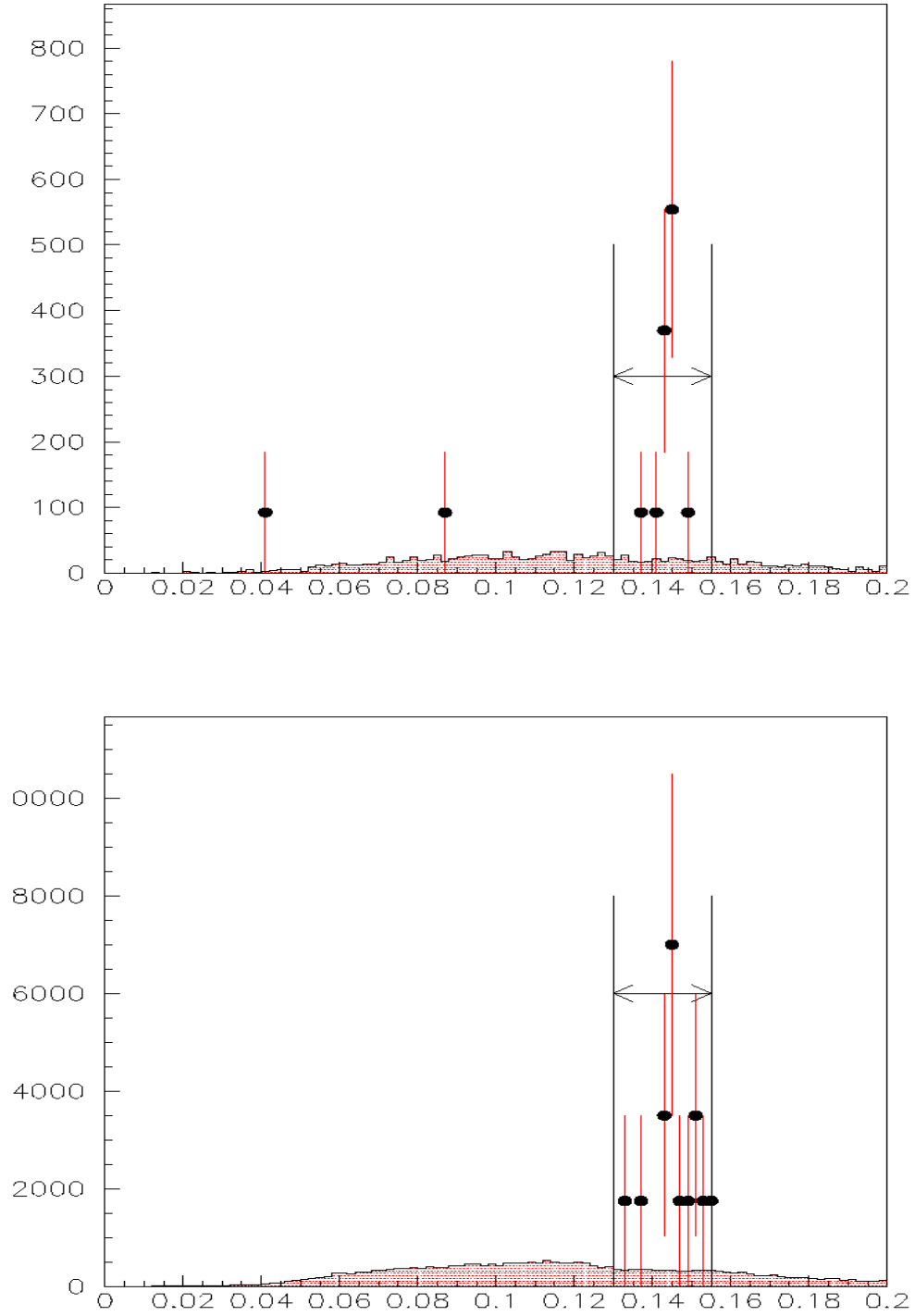


Figure 8.21: Best  $\pi^0$  mass (in  $\text{GeV}/c^2$ ) given by two random unpaired photons for events inside the signal region for 1997 (top) and 1999 (bottom) running, before the cut. Dots are background  $K_L \rightarrow \pi^0 \pi^0 \pi_D^0$  MC, colored histogram is  $K_L \rightarrow \pi^0 \pi_D^0 \gamma$  signal MC.

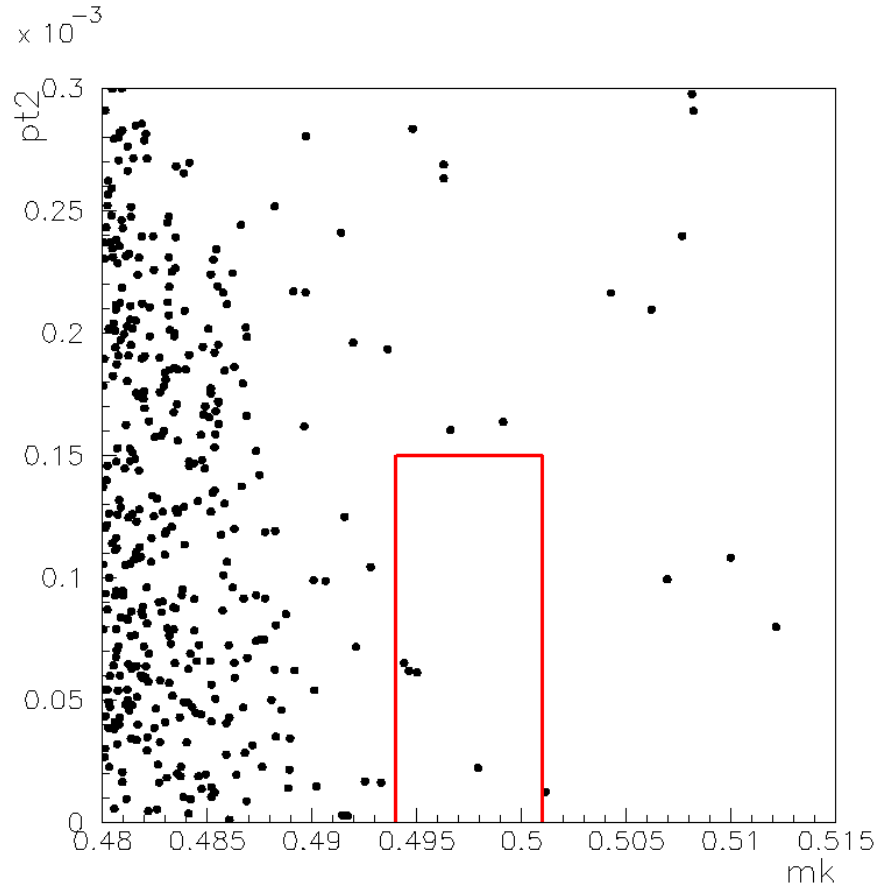


Figure 8.22:  $m_{ee\gamma\gamma\gamma}$  in  $\text{GeV}/c^2$  vs  $p_t^2$  in  $(\text{GeV}/c)^2$  for 1997  $K_L \rightarrow \pi^0 \pi^0 \pi_D^0$  MC after all cuts. The signal box is marked.

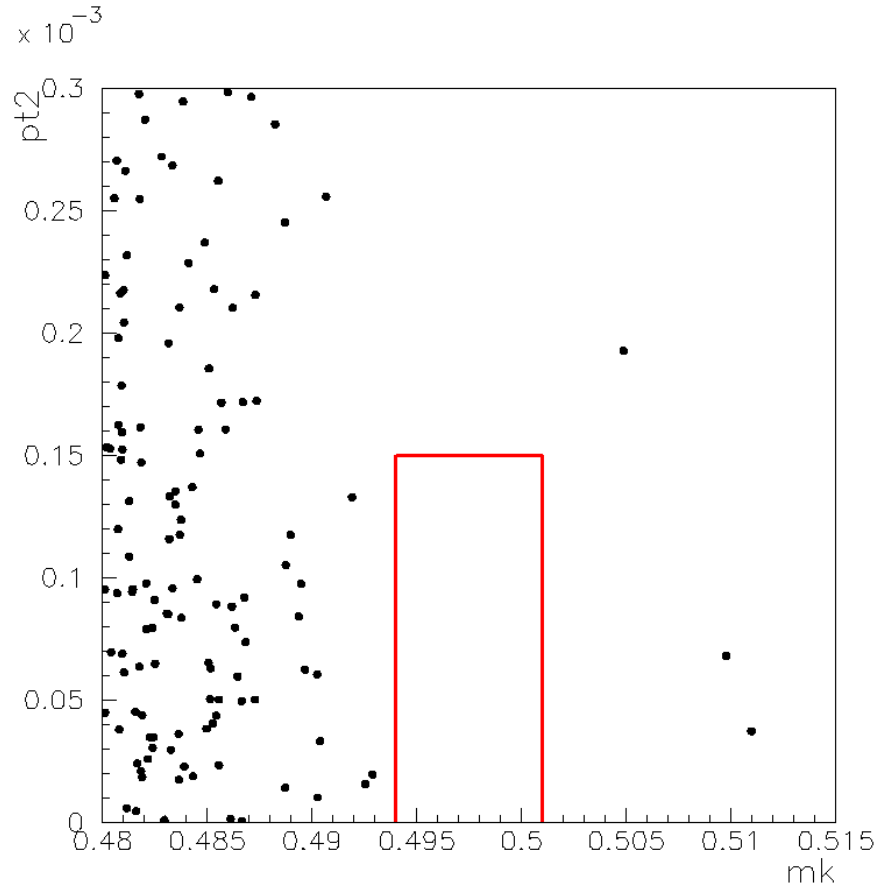


Figure 8.23:  $m_{ee\gamma\gamma\gamma}$  in  $\text{GeV}/c^2$  vs  $p_t^2$  in  $(\text{GeV}/c)^2$  for 1997 data after all cuts. The signal box is marked.

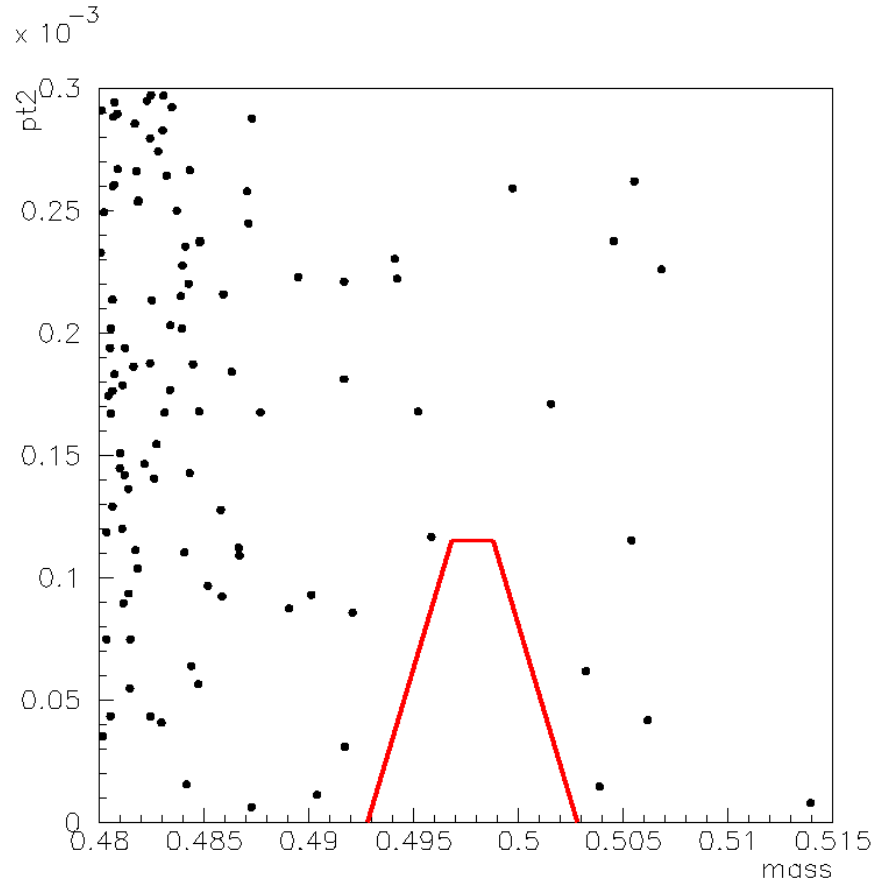


Figure 8.24:  $m_{ee\gamma\gamma\gamma}$  in  $\text{GeV}/c^2$  vs  $p_t^2$  in  $(\text{GeV}/c)^2$  for 1999  $K_L \rightarrow \pi^0 \pi^0 \pi_D^0$  MC after all cuts. The signal box is marked.



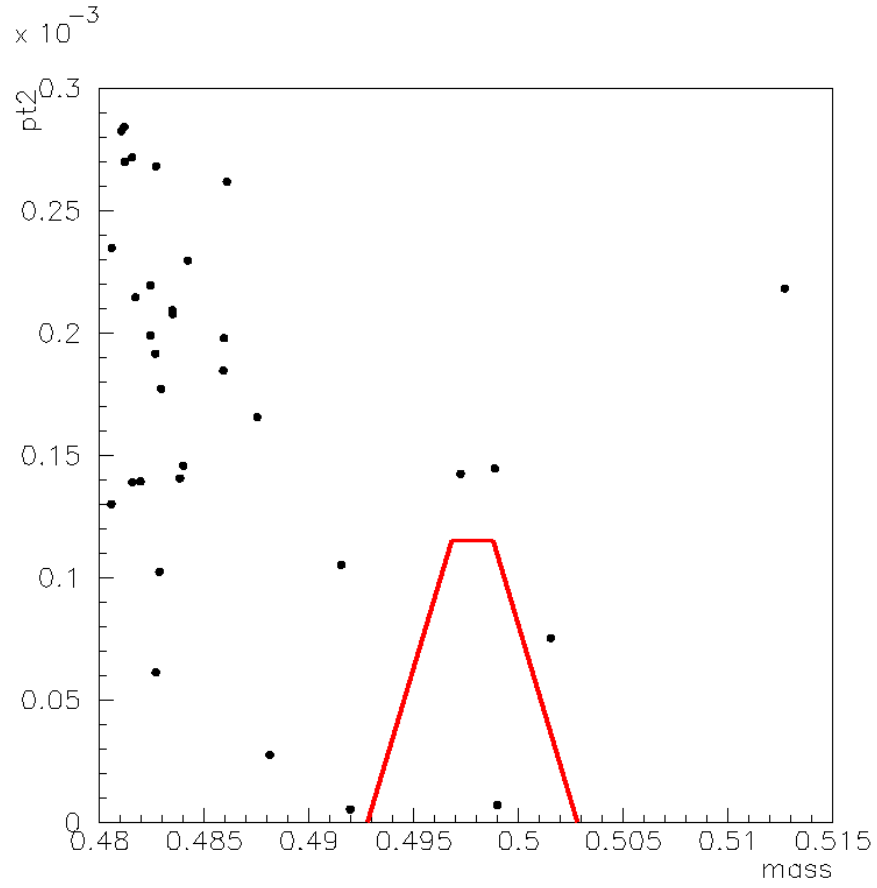


Figure 8.25:  $m_{ee\gamma\gamma\gamma}$  in  $\text{GeV}/c^2$  vs  $p_t^2$  in  $(\text{GeV}/c)^2$  for 1999 data after all cuts. The signal box is marked.

## Chapter 9

# Systematic Errors

### 9.1 The Single Event Sensitivity

The single event sensitivity is defined as the signal branching ratio that will result in exactly one signal event being discovered in the box. For the decay  $K_L \rightarrow \pi^0 \pi_D^0 \gamma$  it is given by:

$$SES(K_L \rightarrow \pi^0 \pi_D^0 \gamma) = \frac{1}{N_K \times A_{sig}} = \frac{BR(K_L \rightarrow \pi^0 \pi^0 \pi_D^0) \times A_{norm}}{N_{norm}^D \times A_{sig}}$$

where  $N_K$  is the total  $K_L$  flux,  $A_{sig}$  is the total signal mode acceptance after all cuts,  $A_{norm}$  is the total normalization mode acceptance after all cuts, and  $N_{norm}^D$  is the number of normalization mode events in data. To get an SES for  $K_L \rightarrow \pi^0 \pi^0 \gamma$  we simply divide by twice the Dalitz factor of 0.012 (since there are two pions that can undergo the Dalitz conversion in the final state). Since  $BR(K_L \rightarrow \pi^0 \pi^0 \pi_D^0) = 3 \times 0.012 \times BR(K_L \rightarrow \pi^0 \pi^0 \pi^0)$ , the Dalitz factor of 0.012 cancels in the SES, leaving a factor of 3/2:

$$SES(K_L \rightarrow \pi^0 \pi^0 \gamma) = \frac{3BR(K_L \rightarrow \pi^0 \pi^0 \pi^0) \times A_{norm}}{2N_{norm}^D \times A_{sig}}$$

The kaon flux for 1997, as calculated in chapter 7, was  $2.43 \times 10^{11}$ ; and the total signal acceptance was 0.101%, resulting in a 1997 single event sensitivity of  $4.07 \times 10^{-9}$  for  $K_L \rightarrow \pi^0 \pi_D^0 \gamma$ , or, dividing by 0.024 (twice the Dalitz factor),

$$SES_{97} = 1.70 \times 10^{-7} \text{ for } K_L \rightarrow \pi^0 \pi^0 \gamma$$

For 1999, the kaon flux was  $3.66 \times 10^{11}$  and the total signal acceptance was 0.085%, giving a 1999 single event sensitivity of  $3.21 \times 10^{-9}$  for  $K_L \rightarrow \pi^0 \pi_D^0 \gamma$  or, dividing by the Dalitz factor of 0.024,

$$SES_{99} = 1.34 \times 10^{-7} \text{ for } K_L \rightarrow \pi^0 \pi^0 \gamma$$

## 9.2 Calculating the Combined SES

The combined SES for the two years is defined by:

$$1 = SES_{total} \times A_{total} \times N_{total}$$

where  $N_{total}$  is the total  $K_L$  flux given by

$$N_{total} = N_{97} + N_{99}$$

and  $A_{average}$  is the average signal acceptance, given by

$$A_{average} = \frac{N_{97}A_{97} + N_{99}A_{99}}{N_{total}}$$

So that

$$1 = (N_{97}A_{97} + N_{99}A_{99}) \times SES_{total}$$

or, using the definition of the single event sensitivity,

$$\frac{1}{SES_{total}} = \frac{1}{SES_{97}} + \frac{1}{SES_{99}}$$

Using this formula, the combined 1997 and 1999 single event sensitivity for  $K_L \rightarrow \pi^0 \pi^0 \gamma$  is  $7.48 \times 10^{-8}$ .

### 9.3 Systematic Error on the SES

There were three possible sources of error on the total single event sensitivity. One was simply the known error on the branching ratio for  $K_L \rightarrow \pi^0 \pi^0 \pi^0$ , 1.2%.<sup>35</sup> Two other factors in the SES calculation, the normalization mode acceptance and the signal mode acceptance, also had associated errors. The errors in these variables were both statistical, due to the finite number of events in each mode, and systematic, reflecting any possible inaccuracies in the Monte Carlo reproduction of events.

The systematic error due to data/Monte Carlo disagreement could not be checked directly for the signal mode, as signal mode data does not exist. However, it was possible to check the disagreement directly for the normalization mode. This was done by removing each

normalization mode-only cut and looking at the resulting change in the total  $K_L$  flux. (The effect of removing cuts common to both the signal and normalization modes was not considered, since theoretically any data/MC disagreement should cancel between the two modes.) This was done separately for 1997 and 1999; the total error for each cut was taken as the weighted average of the 1997 and 1999 errors for that cut. The results of this conservative procedure are shown in table 1. (The cut on the position of the missing photon was not completely removed, since this would result in a large number of misreconstructed events leaking into the normalization mode. Instead, the range of accepted photon positions was increased to include all of the beamhole as well as the Collar Anti.)

### 9.3.1 Statistical Error on the Acceptances

A total of 46669 events were accepted out of fifty million generated  $K_L \rightarrow \pi^0 \pi_D^0 \gamma$  events for both years; this leads to a statistical error of 0.46%. For the normalization mode, 70448  $K_L \rightarrow \pi^0 \pi^0 \pi_D^0$  events were accepted out of 19.08 billion generated events; for a statistical error of 0.37%.

### 9.3.2 Total Error on the SES

Combining the total errors from the  $K_L \rightarrow \pi^0 \pi^0 \pi^0$  branching ratio, data/Monte Carlo disagreement as seen in the normalization-mode only cuts, and statistical errors on the acceptances gives a

total error of 6.69%, or  $5.00 \times 10^{-9}$ , on the combined SES.

## 9.4 Error on the Expected Background

For 1997, a total of 4  $K_L \rightarrow \pi^0 \pi^0 \pi_D^0$  MC events were found in the box for 4.72 generated flux units. For 1999, 0 events were found in the signal region for 3.77 generated flux units. This corresponds to 0.87 expected background events in the signal region for one total  $K_L$  flux. However, these events are weighted by their probability of being signal events (determined from  $p_t^2$  and mass resolutions) before being used in the upper limit calculation, and so the statistical error on the number of events must be weighted as well; this weighting will be described in the next chapter.

The only other source of error on this number comes from other possible backgrounds in the signal region. Several possible backgrounds were generated in Monte Carlo; the total number of events each contributed to the normalization mode, after all cuts, is shown in table 9.2. (None of these modes produced any events in the signal region after all cuts for either year). Since the largest contribution, due to  $K_L \rightarrow \pi^0 \pi_D^0 \pi_D^0$  events, is only 0.13% of the total number of normalization mode events after cuts from  $K_L \rightarrow \pi^0 \pi^0 \pi_D^0$ , these backgrounds were not considered to contribute a significant error.

Cut	Systematic Error %
$m_{\gamma\gamma}$	0.03
$E_\gamma$	0.01
Beamhole photon position	6.50
PP0KINE	0.90
Total	6.56

Table 9.1: Systematic errors due to cuts done only on the normalization mode.

Mode	Fluxes generated (97+99)	Total Events Past Cuts	(%) of Data
$K_L \rightarrow \pi^0 \pi_D^0 \pi_D^0$	1	22	0.13
$K_L \rightarrow \pi^0 \pi^0 \pi^0 \pi^0 \rightarrow e^+ e^-$	10	2	0.01
$K_L \rightarrow \pi^0 \pi^0 \pi^0 \pi^0 \rightarrow e^+ e^- e^+ e^-$	4	7	0.04
$K_L \rightarrow \pi^0 e^+ e^- \gamma$	10	0	0
$K_L \rightarrow \pi^0 \pi_D^0$	3	0	0

Table 9.2: Effect of various backgrounds on the normalization mode, after all normalization mode cuts. The numbers are combined for 1997 and 1999. The last column shows the percentage that each mode would represent of the total normalization mode data (16479 events) after all cuts.

## Chapter 10

# Final Result and Conclusion

In the previous two chapters a combined single event sensitivity for the 1997 and 1999 runs was found, as well as a number of expected background events in the signal region and actual data events in the signal region for each year. It was necessary to combine these results into an upper limit on the branching ratio of  $K_L \rightarrow \pi^0 \pi^0 \gamma$ . This was complicated by the need to incorporate statistical and systematic errors on the SES and background level into the final result, and to weight both data and background events according to their positions within the signal region. The following section describes the method to be used if these complications did not exist; the method used for incorporating errors and performing the weighting will be described subsequently.



## 10.1 The Basic Method

The primary result of the analysis consisted of three numbers—a single event sensitivity, an expected MC background level and a number of background data events. It was necessary to combine these numbers into a 90% confidence level upper limit on the signal branching ratio, which was done using a Feldman-Cousins confidence belt method.<sup>36</sup> The probability of observing a certain number of data events in the signal region,  $n$ , is given by a Poisson distribution:

$$P(n_{exp}, n) = \frac{e^{n_{exp}} n_{exp}^n}{n!}$$

where  $n_{exp}$  is the expected number of signal plus background events in the signal region, based on the Monte Carlo. This variable was a function of the unknown branching ratio for  $K_L \rightarrow \pi^0 \pi^0 \gamma$ :

$$n_{exp} = n_{exp}^b + n_{exp}^s$$

where

$$n_{exp}^s = BR(K_L \rightarrow \pi^0 \pi^0 \gamma) / SES(K_L \rightarrow \pi^0 \pi^0 \gamma)$$

since the SES is the expected branching ratio which will produce one event in the signal region.

To construct the confidence belt plot, the signal branching ratio was scanned over a range from 0 to  $5 \times 10^{-7}$ . For each value of the branching ratio,  $n_{exp}$  was calculated and the Poisson distribution  $P(n_{exp}, n)$  was plotted as a function of  $n$ . The Feldman-Cousins method was used to construct an interval in  $n$  which contained 90% of the Poisson distribution; this was the confidence belt interval for the corresponding value signal branching ratio. By this process, a confidence region was outlined on the two-dimensional plot of  $n$  vs  $BR(K_L \rightarrow \pi^0 \pi^0 \gamma)$ . The 90% upper limit was found as the value of  $BR(K_L \rightarrow \pi^0 \pi^0 \gamma)$  at the point where the horizontal line corre-

sponding to the actual data value of  $n$  intersected the lower edge of the confidence region.

## 10.2 Incorporating Errors

The effect of any error on the SES and/or the number of expected MC background events ( $n_{exp}^{bg}$ ) will be to change the value of the branching ratio that corresponds to a given  $n'$ . These errors can be taken into account by calculating the Poisson functions,  $P(n', n)$ , for a range of possible SES and  $n_{exp}^{bg}$  values, and finding the upper limit using the sum of all the PDFs. (This is equivalent to running the experiment multiple times, obtaining different values of the SES and the expected MC background, and combining the results.) For each calculation of the Poisson function, we choose the SES using Gaussian distributions with a mean equal to the nominal value and a width equal to the total combined error; the value of  $n_{exp}^{bg}$  is chosen similarly.

## 10.3 Weighting Events

Traditionally, upper limit searches have been done using a "cut and count" method, in which a signal region is defined and any data event in the region is assumed to be a potential signal event. In other words, all data events in the signal region are assigned the same weight regardless of their position within the region. This ne-

glects the fact that events on the fringes of the signal region are more likely to be background than events near the center. However, it is possible to use the distributions of signal mode MC and background mode MC events in the signal region to assign each event in the signal region a "signal weight"; and to use this number as the number of events in the region. For consistency, this weight must be applied both to data events in the signal region and to the background MC events in the region. The signal weight for an event is found as

$$P(s) = \frac{P(s)}{P(s) + P(b)}$$

where  $P(s)$  for a given event is the event's signal probability; it is the product of two normalized histograms,  $P(m_{ee\gamma\gamma\gamma\gamma})$  and  $P(p_t^2)$ , both for signal mode MC events in the signal region, for the appropriate year, after all cuts.  $P(b)$ , the background probability, is defined similarly, although since few background events in the signal region survive all cuts the distributions used to find  $P(b)$  are after all cuts except the overlapping clusters cut. The  $m_{ee\gamma\gamma\gamma\gamma}$  and  $p_t^2$  distributions used to calculate  $P(s)$  and  $P(b)$  for 1999 are shown in figure 10.1.

For the MC background, each of the four events in the 1997 signal region was individually weighted in this manner. The sum of the weights (1.69) was divided by the number of generated 1997  $K_L$  fluxes (4.72) to get the total number of expected MC background events for one flux, 0.36. The error on this number was taken to be

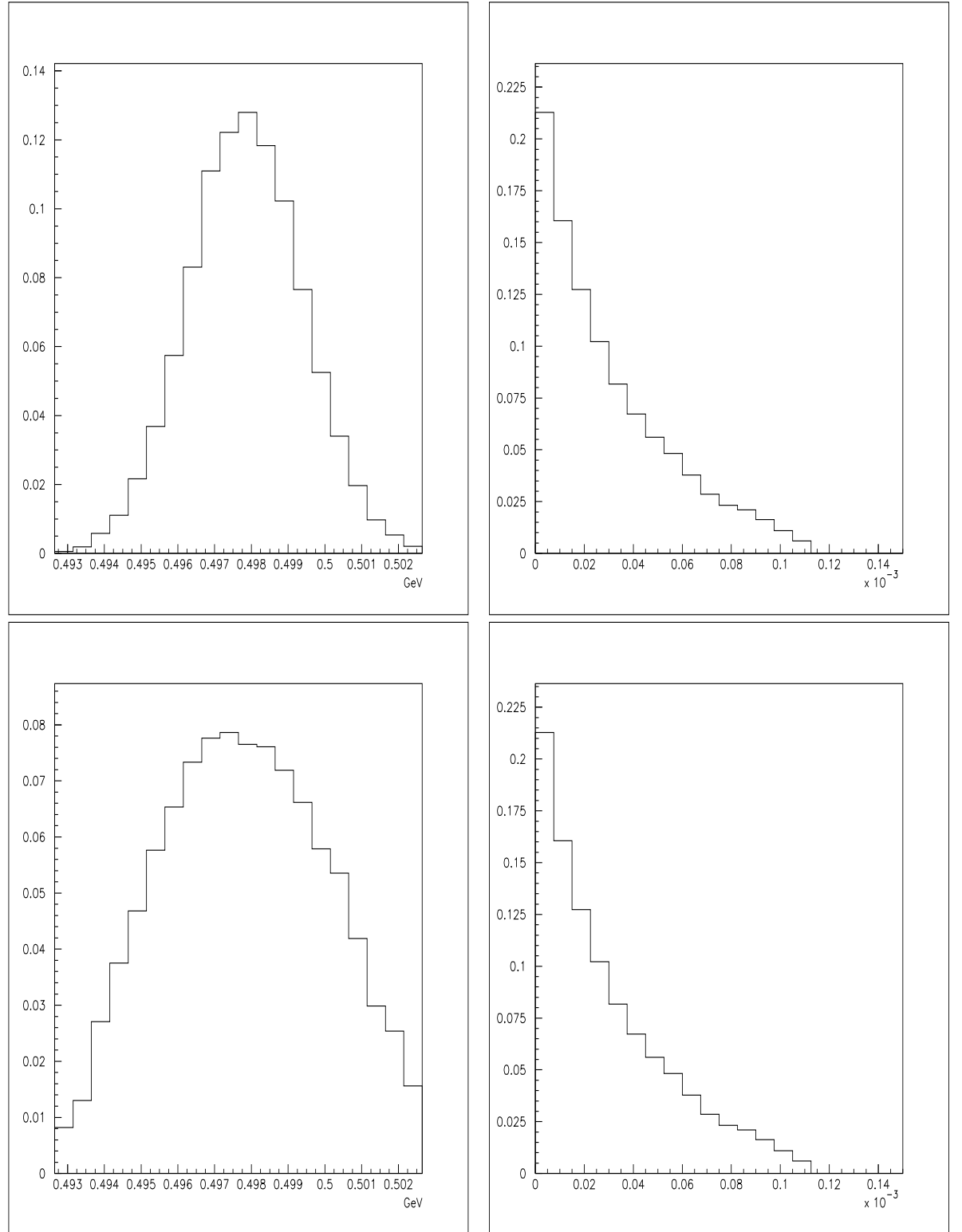


Figure 10.1:  $m_{ee\gamma\gamma\gamma}$  (left) and  $p_t^2$  (right) for 1999 MC events in the signal region after all cuts. The top plots are for signal  $K_L \rightarrow \pi^0 \pi_D^0 \gamma$  MC; the bottom plots are for background  $K_L \rightarrow \pi^0 \pi^0 \pi_D^0$  MC.

the square root of the sum of the weights, divided by the number of fluxes, or  $\sqrt{1.69}/4.72 = 0.28$ .

## 10.4 The Upper Limit

Using the weighting procedure defined above, there were  $0.36 \pm 0.28$   $K_L \rightarrow \pi^0 \pi^0 \pi_D^0$  events expected in the signal region, based on the Monte Carlo, for one total flux of KTeV data. The actual number of data events found in the signal region was zero for 1997 and one for 1999. This one data event had  $m_{ee\gamma\gamma\gamma} = 0.499$  GeV and  $p_t^2 = 8.44 \times 10^{-6} GeV^2$ , giving a signal weight  $P(s) = 0.122$  and a background weight  $P(b) = 0.108$ . This resulted in a total weight of  $0.122/(0.108+0.122) = 0.530$  for this event.

The combined single event sensitivity was  $(7.48 \pm 0.50) \times 10^{-8}$ . The SES and expected background level, with errors, were used to construct the confidence belt plot shown in figure 10.2. The observed data value of 0.53 events intersected the lower edge of the confidence belt at

$$BR(K_L \rightarrow \pi^0 \pi^0 \gamma) = 2.32 \times 10^{-7}$$

and so this is the value assigned as the final 90% upper limit.

## 10.5 Conclusion

The upper limit for  $K_L \rightarrow \pi^0 \pi^0 \gamma$  found in this analysis is a factor of 24 smaller than the previous experimental upper limit,  $5.6 \times 10^{-6}$ ,

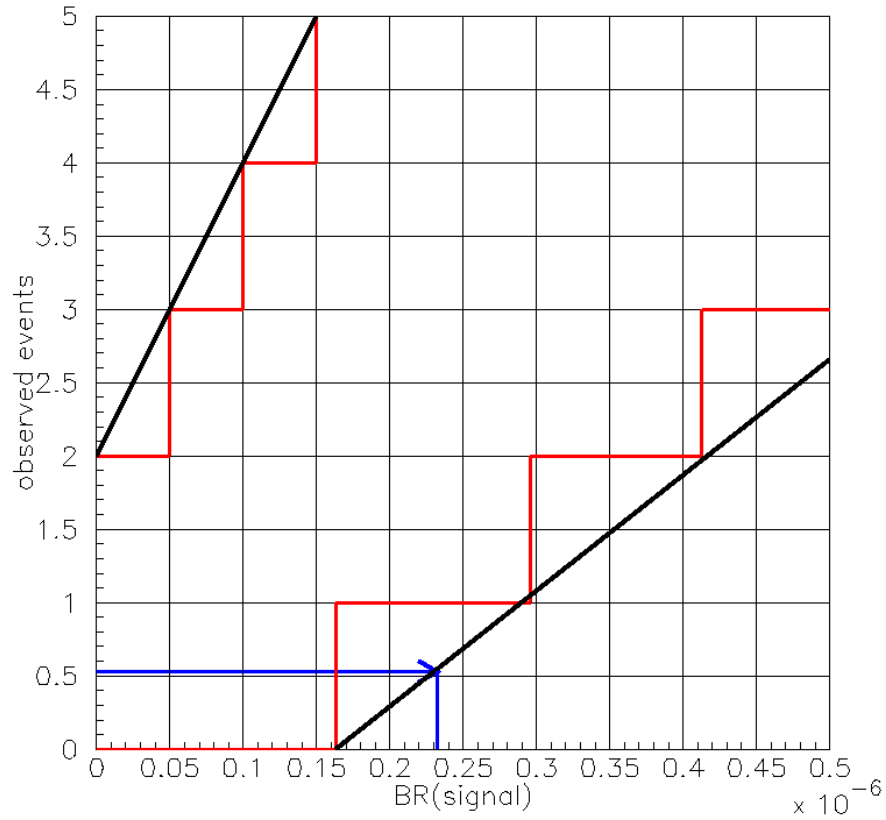


Figure 10.2: Confidence belt plot for the combined analysis. The x-axis shows the signal branching ratio, while the y-axis shows the number of observed events. The area enclosed by the slanted lines is the 90% confidence region. The arrow at  $y=0.53$  corresponds to the weight of the single data event; it crosses the lower edge of the confidence region at  $x = 2.32 \times 10^{-7}$ , giving that as a value for the 90% upper limit.

set by NA31. The upper limit is an order of magnitude larger than the largest theoretical prediction for the branching ratio  $1 \times 10^{-8}$ .



## Notes

- <sup>1</sup>TD Lee and CN Yang, Phys. Rev. 104, 254(1956)
- <sup>2</sup>J. Christenson et.al., Phys. Rev. Lett 13, 186, (1964)
- <sup>3</sup>Gell-Mann and Pais, Phys. Rev. 97, 1387 (1955).
- <sup>4</sup>Lande et. al. Phys. Rev. 103, 1901 (1956)
- <sup>5</sup>Christenson et. al. Phys Rev Lett 13, 138 (1964)
- <sup>6</sup>A.Alavi-Harati et.al. (KTeV collaboration), Phys. Rev. Lett 83, 917. (1999)
- <sup>7</sup>TD Lee and CS Wu, Annu. Rev. Nucl. Sci. 16 (1966)
- <sup>8</sup>Heilliger and Sehgal, Phys. Lett B307:182-186 (1993)
- <sup>9</sup>Heilliger and Sehgal, *ibid.*
- <sup>10</sup>Ecker, Progress in Particle and Nuclear Physics 35:1-80 (1993)
- <sup>11</sup>Barr et. al (NA31 Collaboration), Phys Lett B 351:579-584, (1995)
- <sup>12</sup>Funck and Kambor, Nucl Phys B396:53-80 (1996)
- <sup>13</sup>Barr et. al.(NA31 Collaboration), Phys Lett B.328 528-34 (1994)
- <sup>14</sup>A Alavi Harati et. al., Phys Rev Lett 89, 211810 (2002)
- <sup>15</sup>Coleman, *KTeV Internal Memo 141 (1994)*
- <sup>16</sup>K Hanagaki, PhD Thesis, Osaka University (1998)
- <sup>17</sup>Roodman, "The KTeV Pure CsI Calorimeter", Proceedings of the VII International Conference on Calorimetry, Tuscon AZ, World Scientific (1998)

- <sup>18</sup>Yarema, *KTeV Internal Memo 203, (1994)*
- <sup>19</sup>Roodman, *KTeV Internal Memo 403 (1997)*
- <sup>20</sup>Mikelson, *KTeV Internal Memo 347 (1995)*
- <sup>21</sup>Bown et. al. Nucl Inst Methods, B412,248 (1998)
- <sup>22</sup>Albuquerque et al. *KTeV Internal Memo 319 (1995)*
- <sup>23</sup>Mikelsons, *KTeV Internal Memo 500 (1998)*
- <sup>24</sup>Malensek, Fermilab Report FN-341, Fermilab, 1982
- <sup>25</sup>Heilliger and Sehgal, Phys. Lett B307:182-186 (1993)
- <sup>26</sup>Kroll and Wada, Physical Review 98:1355, 1955
- <sup>27</sup>Toale, Ph.D Thesis, University of Colorado, 2004
- <sup>28</sup>Hamm, Ph.D Thesis, University of Arizona, 2002
- <sup>29</sup>Mikelsons, Ph.D Thesis, University of Colorado, 1999.
- <sup>30</sup>Hamm, Ph.D Thesis, University of Arizona, 2002
- <sup>31</sup>Zimmerman, Ph.D Thesis, University of Chicago, 1999
- <sup>32</sup>Ledovskoy, "The Combined Vertexing Routine", 1999
- <sup>33</sup>Press, Teukolsky, Vetterling and Flannery, *Numerical Recipes in Fortran*, 2nd Edition, Cambridge University Press 1992
- <sup>34</sup>Particle Data Group, Review of Particle Physics, 2002, p.216
- <sup>35</sup>Review of Particle Physics, Particle Data Group, 2002, p.565
- <sup>36</sup>Feldman and Cousins, Phys Rev.D57, 3873 (1998)